Volume 1 Issue 2, June 2022
ISSN: 2810-9635 (Online)

Materials Science in Additive Manufacturing

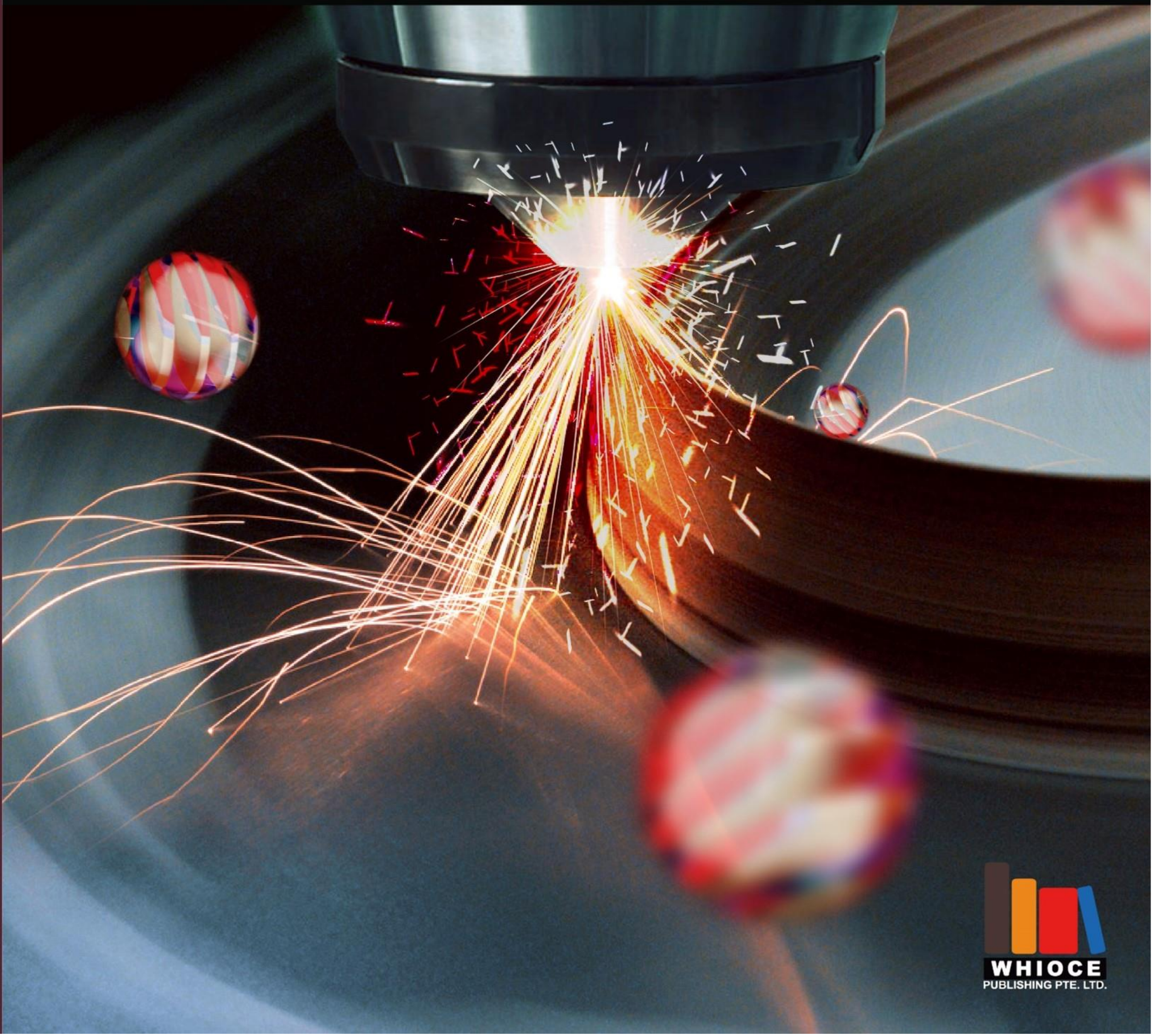

WHIOCE
PUBLISHING PTE. LTD.

Materials Science in Additive Manufacturing

Online ISSN: 2810-9635

Materials Science in Additive Manufacturing aims to bridge the cutting-edge research between additive manufacturing and the entire spectrum of materials science. The journal covers all applied and fundamentals of processing, synthesis, structure, composition, properties and performance of materials designed or manipulated for additive manufacturing. The journal covers a wide scope of innovative techniques, processes, methods, and applications.

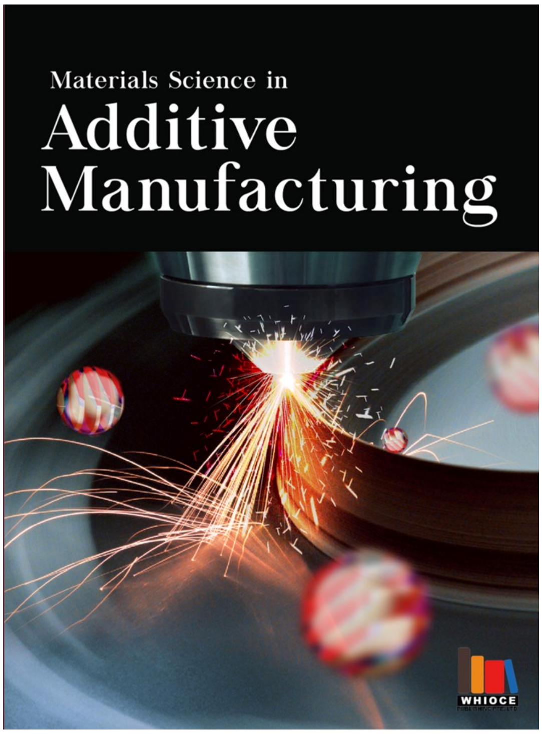

Scan to access website:

Scan to submit papers:

About Whioce Publishing

Whioce Publishing is a publishing company based in Singapore. We have in our portfolio a range of high-quality, open-access, peer-reviewed journals and books.

Contact Us

Managing Editor
Ian Wong
msam.editor@whioce.com

Whioce Publishing
73 Upper Paya Lebar Road # 07-02B-06 Centro Bianco Singapore 534818.

Editorial Office of *Materials Science in Additive Manufacturing*
34-2B, Jalan Puteri 1/2, Bandar Puteri, 47100 Puchong,
Selangor, Malaysia.

Volume 1 Issue 2• June 2022
ISSN 2810-9635 (online)

MATERIALS SCIENCE IN ADDITIVE MANUFACTURING

Editor-in-Chief

Chee Kai Chua

Singapore University of Technology and Design, Singapore

WHIOCE
PUBLISHING PTE. LTD.

Full issue copyright © 2022 Whioce Publishing
All rights reserved. Without permission in writing from the publisher, this full issue publication in its entirety may not be reproduced or transmitted for commercial purposes in any form or by any means, electronic or mechanical, including photocopying, recording, or any information storage and retrieval system. Permissions may be sought from info@whioce.com.

Article copyright © Respective Author(s)
See articles for copyright year. All articles in this full issue publication are open-access. There are no restrictions in the distribution and reproduction of individual articles, provided the original work is properly cited. However, permission to reuse copyrighted materials of an article for commercial purposes is applicable if the article is licensed under Creative Commons Attribution-NonCommercial License. Check the specific license before reusing.

MATERIALS SCIENCE IN ADDITIVE MANUFACTURING

ISSN: 2810-9635 (online)

Editorial and Production Credits

Publisher – Whioce Publishing
Managing Editor – Ian Wong
Production Editor – Ian Wong
Article Layout and Typeset: Sinjore Technologies (India)
Cover Design: BUTTON GRAPHIC DESIGN STUDIO (Malaysia)

For all advertising queries, contact info@whioce.com.

Supplementary file

Supplementary files of articles can be obtained at https://msam.whioce.com/index.php/MSAM/issue/view/7.

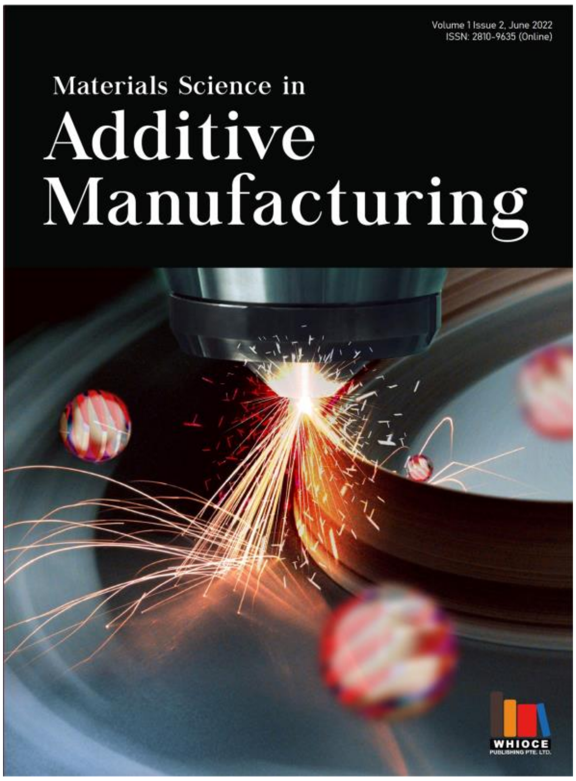

About the Cover

Directed energy deposition in progress

Disclaimer

Whioce Publishing is not liable to the statements, perspectives, and opinions contained in the publications. The appearance of advertisements in the journal shall not be construed as a warranty, endorsement, or approval of the products or services advertised and/or the safety thereof. Whioce Publishing disclaims responsibility for any injury to persons or property resulting from any ideas or products referred to in the publications or advertisements. Whioce Publishing remains neutral with regard to jurisdictional claims in published maps and institutional affiliations.

Materials Science in Additive Manufacturing

Editorial Board

Editor-in-Chief

Associate Editor

Editorial Board Members*

June 2022 | Volume 1 | Issue 2 |

Materials Science in Additive Manufacturing

https://msam.whioce.com/index.php/MSAM/index

CONTENTS

1 **Flexural behavior of 3D printed bio-inspired interlocking suture structures** *ORIGINAL RESEARCH ARTICLE*
Sachini Wickramasinghe, Truong Do, Phuong Tran
http://doi.org/10.18063/msam.v1i2.9

2 **Influence of powder morphology on laser absorption behavior and printability of nanoparticle-coated 90W-Ni-Fe powder during laser powder bed fusion** *ORIGINAL RESEARCH ARTICLE*
Jingjia Sun, Meng Guo, Keyu Shi, Dongdong Gu
https://doi.org/10.18063/msam.v1i2.11

3 **Multi-objective optimization of intense pulsed light sintering process for aerosol jet printed thin film** *ORIGINAL RESEARCH ARTICLE*
Guo Liang Goh, Haining Zhang, Guo Dong Goh, Wai Yee Yeong, Tzyy Haur Chong
https://doi.org/10.18063/msam.v1i2.10

4 **Process study for directed energy deposition of 316L stainless steel with TiB2 metal matrix composites** *ORIGINAL RESEARCH ARTICLE*
Yao Ting Ang, Swee Leong Sing, Joel Choon Wee Lim
https://doi.org/10.18063/msam.v1i2.13

5 **Cold spray additive manufacturing of copper-based materials: Review and future directions** *REVIEW ARTICLE*
Vineeth Menon, Clodualdo Aranas Jr., Gobinda Saha
https://doi.org/10.18063/msam.v1i2.12

WHIOCE PUBLISHING PTE. LTD. Materials Science in Additive Manufacturing

ORIGINAL RESEARCH ARTICLE

Flexural behavior of 3D printed bio-inspired interlocking suture structures

Sachini Wickramasinghe[1], **Truong Do**[2], **Phuong Tran**[1]*

[1]Department of Civil and Infrastructure Engineering, RMIT University, Melbourne, Australia

[2]College of Engineering and Computer Science, VinUniversity, Hanoi, Vietnam

Abstract

Additive manufacturing has allowed producing various complex structures inspired by natural materials. In this research, the bio-inspired suture structure was 3D printed using the fused deposition modeling printing technique to study its bending response behavior. Suture is one of the most commonly found structures in biological bodies. The primary purpose of this structure in nature is to improve flexibility by absorbing energy without causing permeant damage to the biological structure. An interesting discovery of the suture joint in diabolical ironclad beetle has given a great opportunity to further study the behavior of these natural suture designs. Inspired by the elliptical shape and the interlocking features of this suture, specimens were designed and 3D printed using polylactic acid thermoplastic polymer. A three-point bending test was then conducted to analyze the flexural behavior of each suture design, while digital image correlation and numerical simulation were performed to capture the insights of deformation process.

Keywords: Suture structure; Fused deposition modeling; Three-point bending; Digital image correlation; Numerical simulation

***Corresponding author:**
Phuong Tran
(jonathan.tran@rmit.edu.au)

Citation: Wickramasinghe S, Do T, Tran P, 2022, Flexural behavior of 3D printed bio-inspired interlocking suture structures. *Mater Sci Addi Manuf.* 1(2): 9.
https://doi.org/10.18063/msam.v1i2.9

Received: March 17, 2022

Accepted: April 12, 2022

Published Online: May 26, 2022

1. Introduction

Throughout the years of evolution, nature has developed and optimized complex structures to achieve specific functions in every biological body. These complex structures inspire the development of materials and structures with enhanced performances[1,2]. Three-dimensional (3D) printing or additive manufacturing (AM) has made it possible to recreate these complex natural structures and adapt them into engineering applications to improve their functionalities[3-7].

Among various natural structures, suture interfaces are visible in a wide range of species and have independently evolved to optimize the performance of diverse biological systems. Suture structures can be found in mammal crania, deer skull, turtle carapace, red-bellied woodpecker beak, boxfish armor, diatoms, and insect cuticles[8-14]. They provide flexibility to the structure to allow large deformations to absorb impact energy and damp shocks while maintaining structural integrity[15-17]. Depending on the species, the complexity, interlocking features, and sutures' geometry vary to achieve targeted properties[18,19]. For example, triangular sutures can be found in woodpecker beak and interlocking complex suture designs can be found in ammonite shells and diatoms, while elliptical shape interlocking sutures are visible in diabolical ironclad beetle[20]

The recent discovery of the suture structure in diabolical ironclad beetle (*Phloeodes diabolicus*) has attracted many researchers to study its behavior under different test conditions[24]. This beetle species acts dead to protect from predators since they are unable to fly. The flying beetles have hardened forewings, which act as a protection layer for underlying hindwings[25-28]. The elytra of the diabolical ironclad beetle perform remarkable crush resistance from predators in nature. The tough exoskeleton is a result of fusion of two elytra by a suture joint, which runs along the whole length of the abdomen. These interlocking sutures with ellipsoidal geometry, known as blades, are tougher than the triangular and hemispherical blades, which are commonly found in other terrestrial beetles. Figure 1D-F shows the diabolical ironclad beetle, a cross-section of the elytra and the suture connection between two elytra. The suture joints in diabolical ironclad beetle help to resist bending moments to protect vital internal organs. By incorporating interlocking suture interfaces into a biological system, the energy dissipation of the structure is regulated[24,29-31].

Most biological structures contain complex hierarchical arrangements that are difficult to fabricate through conventional manufacturing techniques[32,33]. Due to the design freedom, quality of the product and process control ability, 3D printing has the potential to develop lightweight complex structures[34-36]. Among various AM techniques, fused deposition modeling (FDM) – a trademark of Stratasys or fused filament fabrication – a commonly used term by open hardware community/RepRap is a convenient printing method for developing bio-inspired structures and understanding the mechanical responses and their governing mechanisms[37-39]. FDM printing is a material extrusion technique where thermoplastic material is melted and extruded through a hot end to create the printing layers[40]. Performing mechanical testing on 3D printed bio-inspired structures is beneficial in developing guidelines for future modifications and optimizations of the designs. While AM materials have different properties than natural materials, continuous structural design optimizations and mechanical testing would help to understand the failures, deformations, and damages in biological structures[41,42].

In this research work, diabolical ironclad beetle's suture-inspired designs were printed using polylactic acid (PLA), one of the most popular thermoplastic materials used in FDM printing due to their biodegradability and ease of printing, good strength, and stiffness[43-46]. The flexural behavior was then analyzed using a three-point bending test, followed by digital image correlation (DIC) and numerical simulation to provide more insight into the bending response of the suture structure. As mentioned before, since the suture joint helps resist bending moments in the beetle structure to protect internal organs, the research is focused on understanding the flexural properties of this bio-inspired suture structure. This suture interlocking mechanism would be greatly beneficial in connecting dissimilar materials without any external joining techniques and connecting small parts could develop large modular parts through interlocking without limiting to the small print volume in many 3D printers.

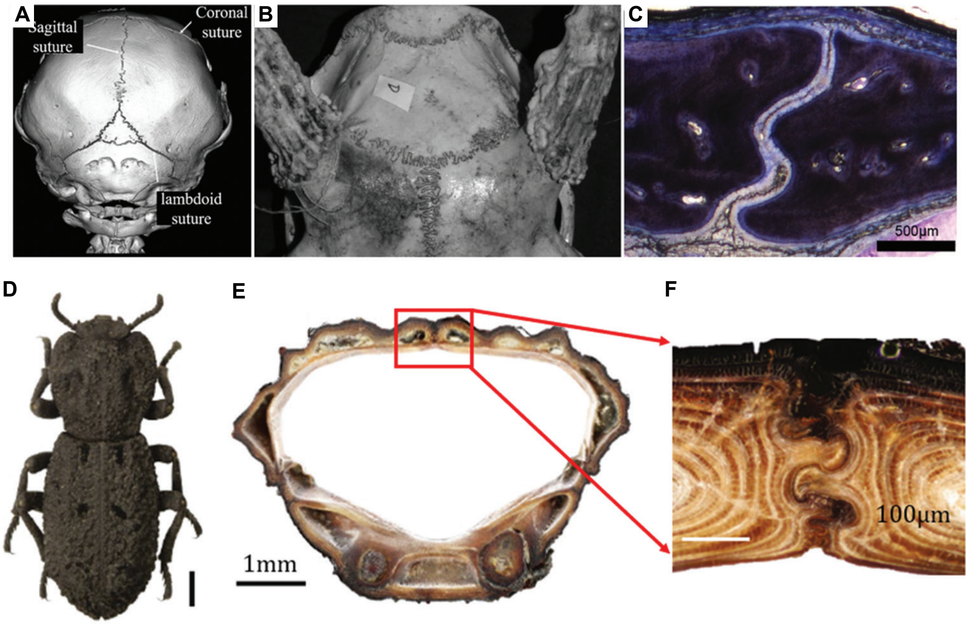

Figure 1. (A) Skull of a domestic shorthair cat[21], (B) cranial suture in white-tailed deer[22], (C) alligator internasal suture[23], (D) *Phloeodes diabolicus*, (E) cross-section of the elytra, (F) suture that connects two elytra (with copyright permission from the journal)[24]

2. Materials and methodology

2.1. Specimen fabrication

The shape of the suture is designed to be elliptical where the ratio between "a" (minor radius) and "b" (major radius) is 1:1.8, while the angle (Θ) between two ellipses is maintained to be 25° as shown in Figure 2A. Design parameters were selected from the literature, where researchers have analyzed the dimensions of the diabolical ironclad beetle's suture structure[24]. All the specimens were fabricated using a FDM technique with 45°/−45° print orientation. In comparison to 0°/90° print orientation, 45°/−45° print orientation contains less porous areas in the printed structure as per the X-ray micro-CT scan images in Figure 2B and D. The curved edges in the sutures are perfectly covered in each layer by 45°/−45° print orientation. Still, in 0°/90° print orientation, the 90° layers could not completely cover the curved edges of the printed structure as shown in microscopic images in Figure 2C and E. PLA specimens are printed using the Prusa Mk3i printer. The suture pattern is inspired by the interlocking connection between the two elytra in the diabolical ironclad beetle (*P. diabolicus*).

Three different sizes of sutures were printed using PLA as S1, S2, and S3; schematic diagrams are given in Figure 3A-C.

Specimens were configured by connecting the two separate parts, printed together without any additional force. Due to the high dimensional accuracy in the printer, two pieces were printed with the exact dimensions without including gap tolerance. Finally, the pieces were easily fitted together like a jigsaw puzzle without affecting the strength of the final part. The S3 design was further subjected to testing to analyze the effect of the positioning angle of the suture interface since, in nature, suture structure does not always follow a precise straight path, as shown in Figure 1A-D. Nearly straight suture lines are visible in infant skull, but in many cases, sutures create complex arrangement[47-49]. The schematic and PLA specimens with slanted suture interface by 2°, 5°, and 8° are given in Figure 3D-F, respectively. Dimensions of S1, S2, and S3 specimens are given in Table 1. Dimensions of S3-2°, S3-5°, and S3-8° are also similar to the dimensions of S3. The areas covered by the suture interfaces in all three sizes are maintained to be ~3.65 cm², which are calculated by the complete elliptic integral of the second kind, multiplied by the thickness of the specimen.

$$c = 4\int_{0}^{\frac{\pi}{2}} \sqrt{a^2 \cos^2 , + b^2 \sin^2 ,}\, d, \qquad \text{(Eq. 1)}$$

$$c' = \int_{0}^{t} \sqrt{a^2 \cos^2 , + b^2 \sin^2 ,}\, d, \qquad \text{(Eq. 2)}$$

$$a \tan\left(\frac{b}{a}\tan\varnothing\right) = t \qquad \text{(Eq. 3)}$$

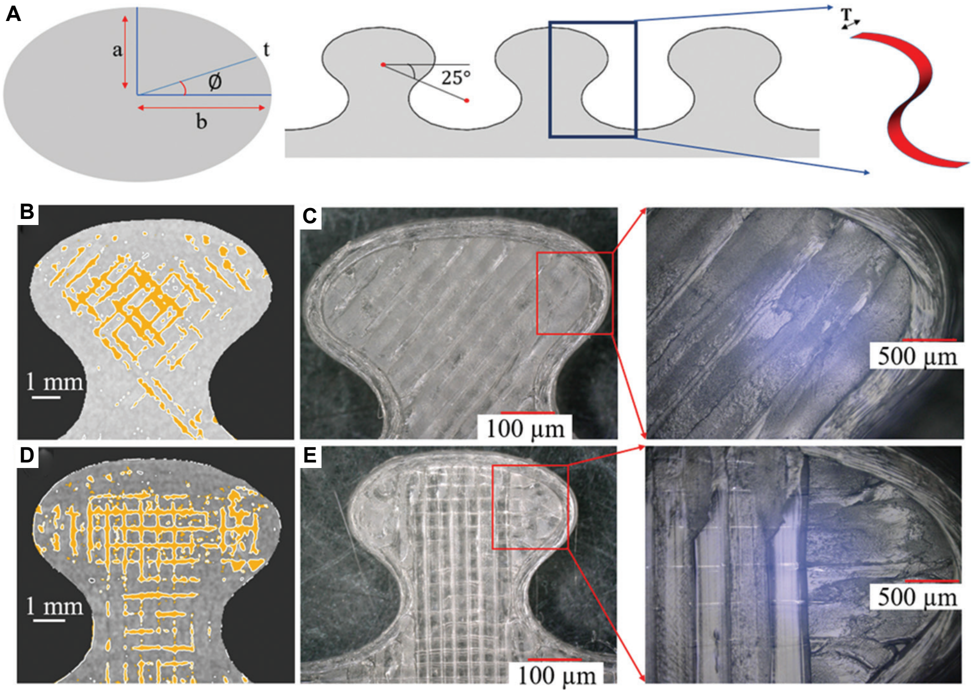

Figure 2. (A) Schematic of the suture design, (B) X-ray micro-CT scan of 45°/-45° print orientation, (C) microscopic images of 45°/-45° print orientation, (D) X-ray micro-CT scan of 0°/90° print orientation, (E microscopic images of 0°/90° print orientation.

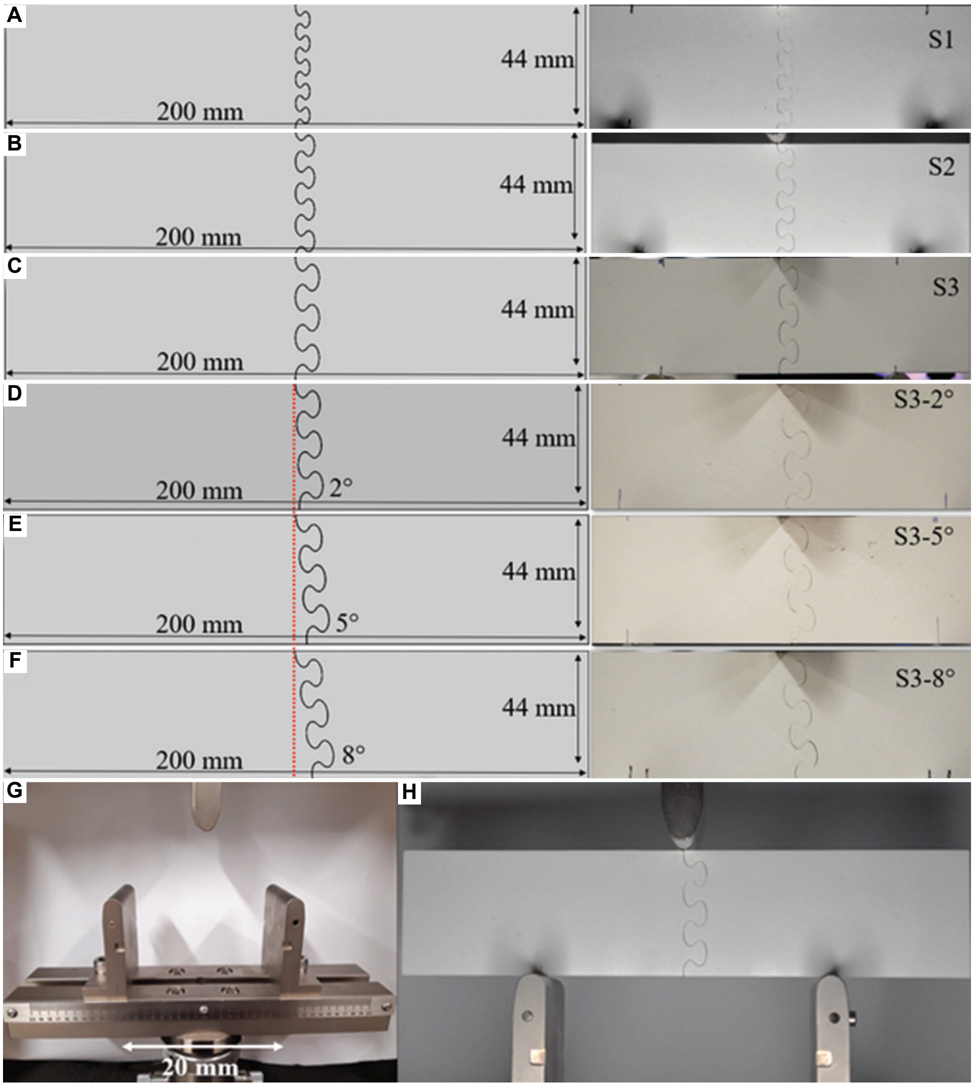

Figure 3. (A) S1 Schematic and PLA Specimen, (B) S2 Schematic and PLA Specimen, (C) S3 Schematic and PLA Specimen, (D) S3-2° Schematic and PLA Specimen, (E) S3-5° Schematic and PLA Specimen, (F) S3-8° Schematic and PLA Specimen, (G) three-point bending test setup, (H) three-point bending setup with specimen.

Table 1. Dimensions of the 3D printed PLA specimens

Specimen	Length (mm)	Width (mm)	Thickness (mm)	Minor radius, a (mm)	Major radius, b (mm)	Print layer height (mm)	Infill density	Number of print layers
S1	200	44	4	1.5	2.7	0.2	100%	20
S2	200	44	4	2	3.6	0.2	100%	20
S3	200	44	4	2.5	4.5	0.2	100%	20

Eq. 1 can be utilized to calculate the total circumference, C of the ellipse, while Eq. 2 and 3 can be utilized to calculate the arc length C′ of the ellipse at a given angle. Minor radius – a, major radius – b, and the angle are shown in Figure 2A. Once the repeat length, as given in Figure 2A, is calculated, the total area can be obtained by multiplying the whole length by the thickness (T), which is 4 mm in all the specimens.

2.2. Flexural test

A three-point bending test was conducted according to ASTM D790 to analyze the behavior of the suture structures under flexural loading[50]. A 5900R Instron universal testing machine with a 5 kN load cell and span length of 20 mm were utilized to perform the test. The length, height, and width of all the specimens were maintained to be 200 mm, 44 mm, and 4 mm, with a span length of 100 mm. The test setup without and with a PLA specimen is given in Figure 3G and H. The crosshead displacement rate was maintained to be 1 mm/min, and a 1 N preload was applied to ensure proper contact between the test specimen and the impactor. Five specimens were tested for each design. The centered cylindrical roller with 10 mm diameter and two supporting rollers at the bottom with 10 mm diameter were utilized to perform the three-point bending test.

2.3. DIC

DIC was conducted using Ncorr open source 2D Matlab software to analyze the strain field generation during the flexural test[51]. The region of interest (ROI) for the DIC was carefully selected to obtain the maximum results. As the specimen was built by connecting two parts, during three-point bending, the two parts started to separate, and creating a gap between the parts; hence, to eliminate the negative impact on the DIC results, selecting the ROI was done separately for the two parts.

2.4. Numerical simulation

A finite element model to simulate the suture inspired structure under a three-point bending test was developed using ABAQUS/Explicit 2020 (Dassault Systems Simulia Corp., Providence, RI). Three rollers having 10 mm diameter were modeled, and the test specimen was placed between the rollers according to the actual experimental setup. Metal rollers are treated as rigid bodies for the simplification of the simulation since they are significantly rigid compared to the PLA specimens. The constitutive behavior of the suture inspired test specimens is considered to be elastic-perfectly plastic based on the literature[52-55]. It is worth mentioning that the material anisotropy and localized defects that occur due to the 3D printing process are not considered in this analytical model. Through displacement boundary conditions, loading was applied to the top roller, while two bottom supporting rollers were encastered. Hard contact formulation was utilized to create normal contact behavior between the rollers and the test specimens, and tangential behavior was defined using penalty friction formulation with a friction coefficient of 0.3. A two-dimensional model was developed to save the cost and time of the simulation for S1, S2, S3, S3-2°, S3-5°, and S3-8° with 38029 linear quadrilateral elements of type CPS4R. The load of the top roller was further analyzed, and the bending stiffness of each specimen is calculated by the slope of the linear part of the force-displacement curve.

3. Results and discussion

3.1. Experimental results

The force-displacement curves of S1, S2, and S3 are given in Figure 4A. The number of suture ligaments in each design decreased with the increment of the size of the suture unit, thereby affecting the maximum load the structure can withstand before the failure. As per the force-displacement curves, it is evident that the S1 specimen withstand the highest load while the S2 specimen indicates the lowest maximum load. When it comes to the S3 specimen, the maximum load it can withstand had increased compared to S2 but was still lower than the S1. In all three cases, the force-displacement curves exhibit a similar pattern. Once the lowest suture ligament fails, the load suddenly drops, then starts to increase again and experiences another

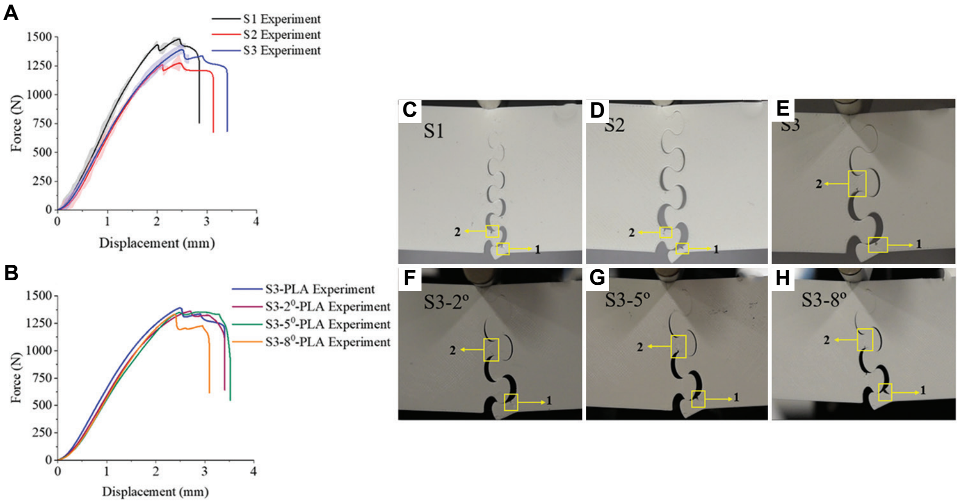

Figure 4. (A) Force-displacement curves of S1, S2, and S3. (B) Force- displacement curves of S3, S3-2°, S3-5°, and S3-8°; the failure points highlighted in yellow for (C) S1- first & second points, (D) S2 - first & second points, (E) S3 - first & second points (F) S3-2, (G) S3-5°, (H) S3-8°

sudden drop, it continues with a plateau until the failure of the whole structure.

As S3 exhibits the highest displacement, it implies that the S3 structure can absorb more energy by deforming than S1 and S2. Further studies on the effect of the positioning angle of the suture structure on flexural properties are conducted using the S3 specimen design. The positioning angles are varied by 2°, 5° and 8°. The positioning angles were varied by 2°, 5°, and 8° as given in Figure 3D-F. The maximum loads of S3-2°, S3-5°, and S3-8° designs were decreased, respectively, and all three maximum load values were lower than the maximum load of the S3 specimen. The total displacement of the S3-2° before the failure is almost similar to the S3, while S3-5° exhibits a larger displacement than S3. When it comes to S3-8°, the displacement significantly reduces compared to all the above-mentioned test specimens. The force-displacement curves are given in Figure 4B. These results indicate that the position of the suture components with respect to the applied load is a critical factor, and there is a possibility for further improvement of S3 by allocating the most suitable positioning angle.

In all the cases, failure first occurred at the semi suture module located at the bottom end of the suture component, indicated by first yellow square in Figure 4C-H. In all S3 samples, the second fracture point occurred in the middle of the suture module. In contrast, in S1 and S2, the second fracture point occurred closer to the first one, which implies in S3 specimens, stress is distributed evenly among all suture modules.

Flexural strength, bending stiffness, and energy absorbed by each design are given in Figure 5. As shown in Figure 5A, the flexural strength is significantly higher in the S1 sample than in S2 and S3. With the increment of the positioning angle, the flexural strength gradually decreases compared to the original S3 sample. The bending stiffness of each design is calculated using the force-displacement curve slope. Energy absorption is calculated using the area under the force-displacement curve. The bar charts indicate that bending stiffness decreases gradually with the increment of the positioning angle. Compared to S1, the absorbed energy of S2 and S3 is increased by 20% and 48%, respectively. Compared to S3, the energy absorption of S3-2°, S3-5°, and S3-8° is reduced by 4.2%, 1%, and 20%, respectively. Considering the flexural strength, bending stiffness, energy absorption, and failure pattern, different suture structures can be employed to achieve the desired performances. For example, the S1 design would perform better than S2 or S3, where higher flexural strength is required, and S3 would perform better than S1 or S2 in absorbing higher energy.

3.2. DIC results

DIC results of strain fields () for S3, S3-2°, S3-5°, and S3-8° when the fracture starts to propagate are given in Figure 6A-D, respectively. Strains fields generated in both parts of the specimens are given in the images. The ROI was selected separately for the interlocked parts in the same specimen to obtain clear strain filed contour plots. Higher strain along y-direction was visible in the weaker semi suture module at the bottom of the test specimen, which implies high-stress generation.

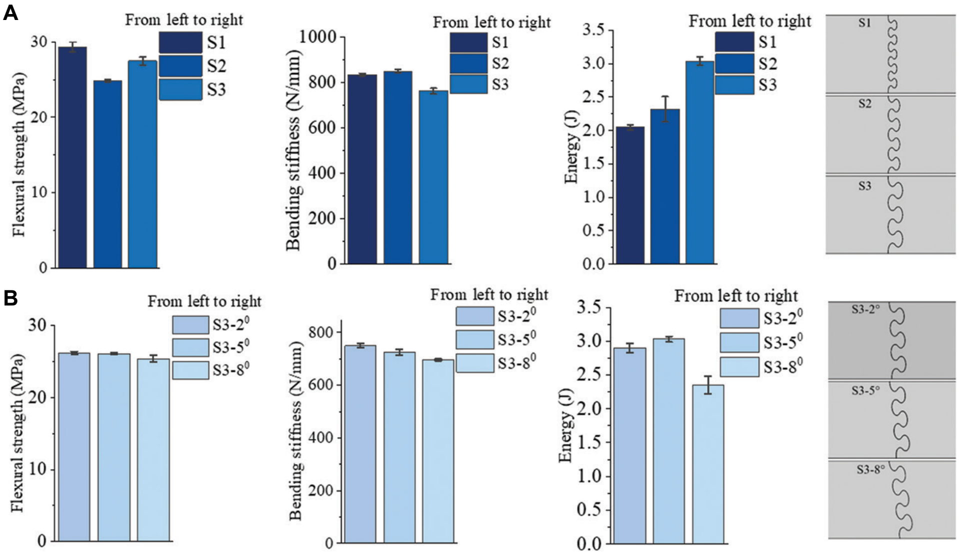

Figure 5. (A) Flexural strength, bending stiffness and energy absorption of S1, S2 and S3. (B) Flexural strength, bending stiffness and energy absorption of S3-2°, S3-5° and S3-8°.

From all DIC results, it is visible that one side of the necking area is under compression in every suture module while the other side of the necking area experiences tension. The force exerted by the top suture module causes tension on the necking area of the bottom suture module. Meanwhile, the top suture module gets compressed by the bottom suture module in return due to the interlocking feature. DIC contour plots of the S3 specimen show high-stress concentration in the suture modules, while with the increment of the inclined angle, stress is distributed more uniformly across all suture modules. This could be the reason for S3-2° and S3-5° specimens to have a slight increment in the displacement before the failure compared to the S3 one, as given in Figure 4B. In S3-2° and S3-5° specimens, stress is uniformly distributed among all the suture modules. Still, in the S3-8° specimen, stress is mainly concentrated at the weaker semi suture module at the bottom, causing failure at a lower displacement.

3.3. Comparison between experimental and numerical simulation results

The comparison between force-displacement curves obtained from numerical simulation and the experimental results for S1, S2, and S3 are shown in Figure 7A. The numerical simulation results show a good agreement with the experimental results with slight discrepancy due to the assumption of elastic-perfectly plastic material constitutive model. Figure 7B-D exhibits the deformation comparison of simulation and experimental results of S1, S2, and S3. Simulation results have captured the deformation of each suture design till the specimens reach their maximum loading conditions.

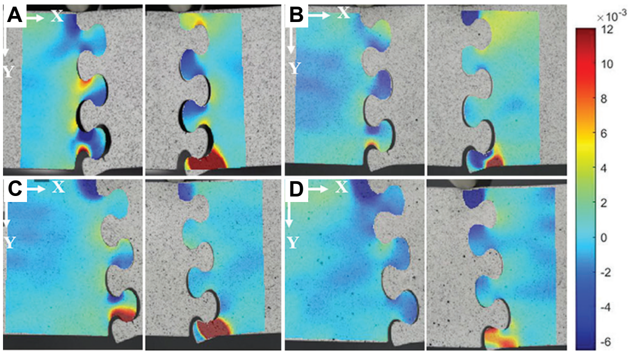

Figure 6. DIC contour plots of ϵ_{yy} strain fields for the two interlocked parts just before the fracture. (A) S3, (B) S3-2°, (C) S3-5°, and (D) S3-8. Region of interest (ROI) is selected separately for the two parts of the same interlocked specimen.

Compared to S1 and S2, sample S3 shows higher deformation, implying that the structure is more flexible. The number of interlocking points directly affects the structure's flexibility and strength. Fewer interlocking points allow the structure to deform in a larger displacement, while many interlocking points make the structure stiffer. Force-displacement graphs from the experiment and simulation model for S3-2°, S3-5°, and S3-8° are given in Figure 8A. Numerical simulation results show good agreement with the experimental results up to the point of maximum load. Similar to the previous section, the slight difference between the experimental and simulation results is caused due to not considering the porosity effect of 3D printed structures and assuming the model behavior to be elastic perfectly plastic.

The deformation captured by the simulation and the experimental deformation for S3-2°, S3-5°, and S3-8° are shown in Figure 8B-D.

3.4. Parametric study

Many biological structures with sutures do not contain a single suture line throughout the whole structure, but rather a network of suture lines to create complex arrangements[9,49,56]. Here, a simple parametric study was conducted to investigate the influence of two suture lines in the structure. For all three sizes, S1, S2, and S3 symmetrical suture lines with inclined angles of 0, 2, 5, and 8 degrees were incorporated in two different configurations as shown in Figure 9A and B. Specimens are created by connecting three separate parts to include two suture lines. The two

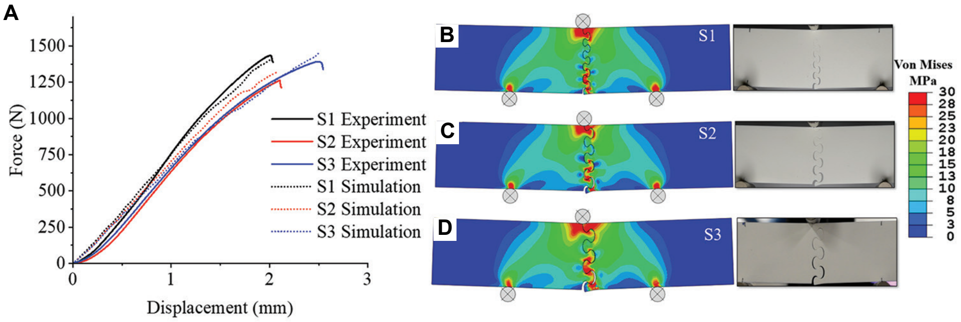

Figure 7. (A) Numerical simulation and experimental force-displacement results comparison of S1, S2 and S3. Von Mises stress distribution comparison at the maximum load of each design: (B) S1 simulation and experiment, (C) S2 simulation and experiment, and (D) S3 simulation and experiment.

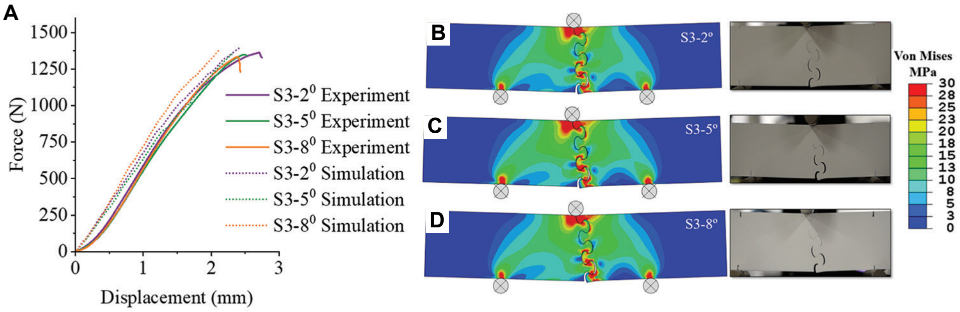

Figure 8. (A) Numerical simulation and experimental force-displacement results comparison of S3-2°, S3-5° and S3-8°. Von Mises stress distribution comparison at the maximum load of each design: (B) S3-2° simulation and experiment, (C) S3-5° simulation and experiment, and (D) S3-8° simulation and experiment.

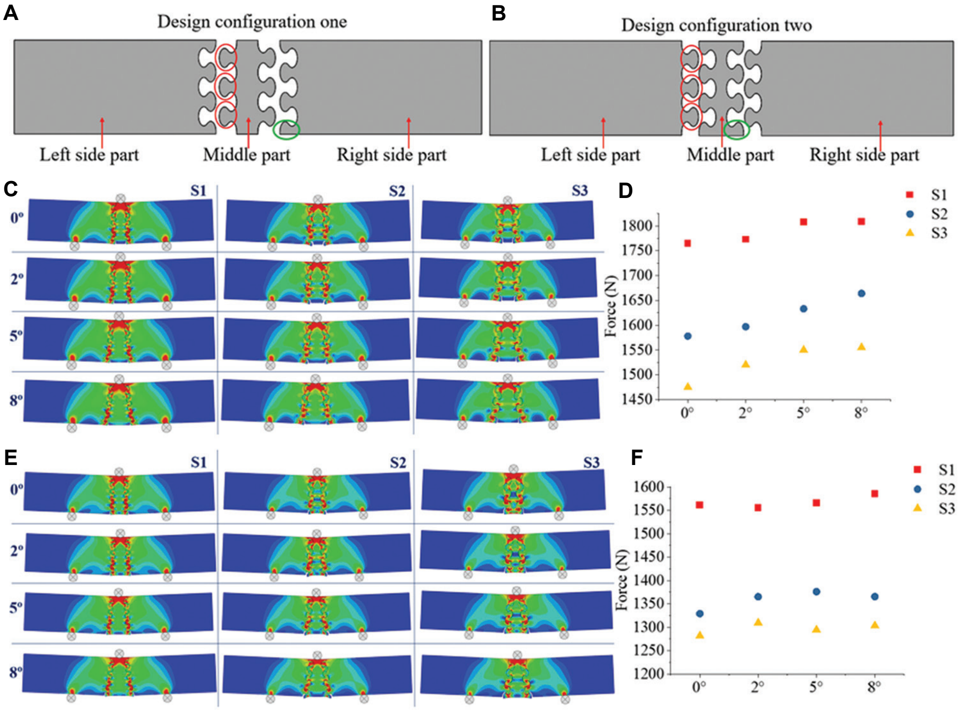

Figure 9. (A) Design configuration one, and (B) design configuration two; red circles indicate the placement of the interlocking suture modules on the side part and the middle part of the specimen, and green circle shows the weaker semi suture module. (C) Von Mises stress comparison of 0°, 2°, 5° and 8° inclined angle designs in configuration one. (D) Scatter plot of peak forces in each design. (E) Von Mises stress comparison of 0°, 2°, 5° and 8° inclined angle designs in configuration two. (F) Scatter plot of peak forces in each design.

design configurations are shown in Figure 9A and B. In configuration one, many numbers of interlocking suture modules were printed in the middle part of the specimen, and in configuration two, many interlocking suture modules were printed in the side parts of the specimen as highlighted in red circles. Figure 9C and E show the completed specimens of the two design configurations at their maximum load. Figure 9D and F show the scatter plots of the maximum force encountered by each design.

In all the cases, S1 yields the highest maximum force due to its many interlocking points compared to S2 and S3, even though in all three cases, the areas covered by sutures are equal. Parametric results from design configuration one show that the maximum force gradually increases with the increment of the inclined angle. Despite small fluctuations in the maximum loads in design configuration two, the overall results present similar behavior to design configuration one. This implies that design configuration one could provide a more stable and predictable structure, as the force gradually increases with the increment of the angle without any fluctuations in the results, compared to configuration two.

Table 2 . The percentage increments of the maximum loads in design configuration one compared to the design configuration two

	S1	S2	S3
0°	13 %	18 %	15 %
2°	14 %	16 %	16 %
5°	15 %	18 %	19 %
8°	14 %	21 %	19 %

Comparing the results of design configurations one and two, as given in Figure 9A and B, the maximum load obtained by samples S1, S2, and S3 in configuration one is higher than in configuration two. The percentage increment of the maximum loads in design configuration one compared to the design configuration two is given in Table 2.

Similar to the experimental results, higher stress occurs in the bottom semi suture module in every design where the first failure occurs. In design configuration one, weaker bottom semi suture modules (highlighted in green circle in Figure 9A) are attached to the bigger side parts, where they gain support for the stress distribution; hence, this design configuration can withstand a higher load. In configuration two, weaker bottom semi suture modules (highlighted in green circle in Figure 9B) are connected to the middle part of the specimen, where it gains support only from the middle part for the stress distribution, as shown in Figure 9B. This leads the design configuration two to withstand a lower maximum load compared to the configuration one.

This parametric study showed that the maximum load the structure can withstand could be improved by combining symmetrical suture lines, correlating with the inclined angle increment. The placement of the weaker link within the suture structure also significantly impacts the highest load the structure can withstand.

4. Conclusion

The research was conducted to investigate the flexural behavior of bio-inspired suture structures. The specimens were developed with three different sizes as S1, S2, and S3 using 3D printing of PLA thermoplastic while maintaining the ratio between the minor and major radii of the elliptical suture shape to 1:1.8. S3 design was used to develop S3-2°, S3-5°, and S3-8°, varying the positioning angles by 2°, 5°, and 8° to analyze the effect of the positioning angle. The S1 specimen withstood maximum load during the three-point bending test but failed within short displacement, whereas S3 showed higher displacement before the failure but with a lower maximum load. The flexural strengths of S1, S2, and S3 were noted to be 28 MPa, 24 MPa, and 26 MPa, while the energy absorption of each design was calculated as 2 J, 2.5 J, and 3 J. Bending stiffness values indicate that compared to S1, both S2 and S3 designs are harder to bend.

(i) When changing the positioning angle of the suture component, the total displacement before the failure was slightly increased compared to the S3, in both S3-2° and S3-5°. Further increment in the angle up to 8° has noticeably reduced the total displacement at failure compared to S3 specimen as the stress is concentrated mainly in the weaker semi suture module at the bottom rather than uniformly distributing through the whole suture structure. In all three cases, flexural strengths and energy absorptions were slightly reduced compared to S3. The variation in bending stiffness values suggests that by changing the positioning angle of the sutures, the stiffness of the whole structure could be improved.

(ii) DIC results indicate that adjacent interlocking suture modules exert tension and compression on each other due to their interlocking feature. When the top suture modules exert tension on the necking area of the bottom suture module, the head of the bottom suture module curls up and compresses the top suture module, and instead of moving down before fracture occurs in its necking area.

(iii) Numerical simulation showed good agreement with the experimental results. The model was assumed to be elastic-perfectly plastic, even though FDM prints contain defects due to the printing process. The model reveals that introducing larger suture modules with less interlocking points allows more uniform stress distribution along the suture structure compared to S1 and S2, where the stress was mainly concentrated to the suture modules at the bottom of the specimen.

(iv) The parametric study was performed on beam samples with two symmetrical suture lines, which considerably enhanced the ability to withstand a higher load. The load-bearing ability of the structure was further improved with the increment of the inclined angle. The simulation results also confirm that positioning of the interlocking suture modules plays an important role in enhancing the load-bearing properties of the structure. The parametric study concluded that the position of the suture components has a significant impact on the mechanical performance of the whole structure.

(v) These sutures could be beneficial in many ways when developing a structural design. Incorporating a suture joint creates a pre-established crack path which would help to predict the fracture behavior by analyzing the suture pattern while maintaining flexibility. As the suture joint is developed without any adhesive materials, this interlocking mechanism could be utilized to join dissimilar materials without any external joining treatments. Finally, large modular parts could be manufactured by connecting small pieces through the interlocking technique without limiting to the small part volume in many 3D printers.

Based on our results, we conclude that depending on the desired mechanical performance, different suture designs can be utilized to achieve a decent outcome. For example, when high energy absorption is required, S3 design could be benefited, and when a higher load-bearing action is required, S1 design could be highly effective. From the results of this research, it is evident that bio-inspired suture structures can be further optimized to enhance their performances, providing countless advantages for many engineering applications.

Acknowledgments

The authors acknowledge the facilities and the scientific and technical assistance of the Advanced Manufacturing Precinct, the Rheology and Materials Characterization Laboratory at RMIT University.

Funding

This research received no external funding.

Conflict of interest

The authors declare no conflict of interest.

Author contributions

Conceptualization: Phuong Tran

Data curation: Sachini Wickramasinghe

Funding acquisition: Truong Do

Methodology: Phuong Tran

Supervision: Phuong Tran

Writing—original draft: Sachini Wickramasinghe

Writing—review and editing: Truong Do, Phuong Tran

All authors have read and agreed to the published version of the manuscript.

References

1. Ghazlan A, Ngo T, Tan P, *et al.*, 2021, Inspiration from nature's body armours-a review of biological and bioinspired composites. *Compos B Eng*, 205: 108513.

   https://doi.org/10.1016/j.compositesb.2020.108513

2. Ahamed MK, Wang H, Hazell PJ, 2022, From biology to biomimicry: Using nature to build better structures a review. *Constr Build Mater*, 320: 126195.

   https://doi.org/10.1016/j.conbuildmat.2021.126195

3. Du Plessis A, Broeckhoven C, Yadroitsava I, *et al.*, 2019, Beautiful and functional: A review of biomimetic design in additive manufacturing. *Addit Manuf*, 27: 408–427.

   https://doi.org/10.1016/j.addma.2019.03.033

4. Plocher J, Mencattelli L, Narducci F, *et al.*, 2021, Learning from nature: Bio-inspiration for damage-tolerant high-performance fibre-reinforced composites. *Compos Sci Technol*, 208: 108669.

   https://doi.org/10.1016/j.compscitech.2021.108669

5. Liu J, Li S, Fox K, *et al.*, 2022, 3D concrete printing of bioinspired bouligand structure: A study on impact resistance. *Addit Manuf*, 50: 102544.

   https://doi.org/10.1016/j.addma.2021.102544

6. Tee YL, Maconachie T, Pille P, *et al.*, 2021, From nature to additive manufacturing: Biomimicry of porcupine quill. *Mater Des*, 210: 110041.

   https://doi.org/10.1016/j.matdes.2021.110041

7. Peng C, Tran P, 2020, Bioinspired functionally graded gyroid sandwich panel subjected to impulsive loadings. *Compos B Eng*, 188: 107773.

   https://doi.org/10.1016/j.compositesb.2020.107773

8. Achrai B, Wagner HD, 2013, Micro-structure and mechanical properties of the turtle carapace as a biological composite shield. *Acta Biomater*, 9: 5890–5902.

   https://doi.org/10.1016/j.actbio.2012.12.023

9. Krauss S, Monsonego-Ornan E, Zelzer E, *et al.*, 2009, Mechanical function of a complex three-dimensional suture joining the bony elements in the shell of the red-eared slider turtle. *Adv Mater*, 21: 407–412.

   https://doi.org/10.1002/adma.200801256

10. Lee N, Horstemeyer M, Rhee H, *et al.*, 2014, Hierarchical multiscale structure-property relationships of the red-bellied woodpecker (*Melanerpes carolinus*) beak. *J R Soc Interf*, 11: 20140274.

    https://doi.org/10.1098/rsif.2014.0274

11. Liu Z, Zhang Z, Ritchie RO, 2020, Interfacial toughening effect of suture structures. *Acta Biomater*, 102: 75–82.

    https://doi.org/10.1016/j.actbio.2019.11.034

12. Vincent JF, Wegst UG, 2004, Design and mechanical properties of insect cuticle. *Arthrop Struct Dev*, 33: 187–99.

    https://doi.org/10.1016/j.asd.2004.05.006

13. Yang W, Naleway SE, Porter MM, *et al.*, 2015, The armored carapace of the boxfish. *Acta Biomater*, 23: 1–10.

    https://doi.org/10.1016/j.actbio.2015.05.024

14. Magwene PM, Socha JJ, 2013, Biomechanics of turtle shells: How whole shells fail in compression. *J Exp Zool A Ecol*

Genet, 319: 86–98.

https://doi.org/10.1002/jez.1773

15. Jia Z, Yu Y, Wang L, 2019, Learning from nature: Use material architecture to break the performance tradeoffs. *Mater Des*, 168: 107650.

    https://doi.org/10.1016/j.matdes.2019.107650

16. Chen IH, Yang W, Meyers MA, 2015, Leatherback sea turtle shell: A tough and flexible biological design. *Acta Biomater*, 28: 2–12.

    https://doi.org/10.1016/j.actbio.2015.09.023

17. Alheit B, Bargmann S, Reddy B, 2020, Computationally modelling the mechanical behaviour of turtle shell sutures a natural interlocking structure. *J Mech Behav Biomed Mater*, 110: 103973.

    https://doi.org/10.1016/j.jmbbm.2020.103973

18. Gao C, Li Y, 2019, Mechanical model of bio-inspired composites with sutural tessellation. *J Mech Phys Solids*, 122: 190–204.

    https://doi.org/10.1016/j.jmps.2018.09.015

19. Lin E, Li Y, Ortiz C, *et al.*, 2014, 3D printed, bio-inspired prototypes and analytical models for structured suture interfaces with geometrically-tuned deformation and failure behavior. *J Mech Phys Solids*, 73: 166–182.

    https://doi.org/10.1016/j.jmps.2014.08.011

20. Malik IA, Mirkhalaf M, Barthelat F, 2017, Bio-inspired “jigsaw”-like interlocking sutures: Modeling, optimization, 3D printing and testing. *J Mech Phys Solids*, 102: 224–238.

    https://doi.org/10.1016/j.jmps.2017.03.003

21. Schmidt MJ, Farke D, Staszyk C, *et al.*, 2022, Closure times of neurocranial sutures and synchondroses in Persian compared to Domestic Shorthair cats. *Sci Rep*, 12: 1–13.

    https://doi.org/10.1038/s41598-022-04783-1

22. Nicolay CW, Vaders MJ, 2006, Cranial suture complexity in white-tailed deer (*Odocoileus virginianus*). *J Morphol*, 267: 841–849.

    https://doi.org/10.1002/jmor.10445

23. Bailleul AM, Scannella JB, Horner JR, *et al.*, 2016, Fusion patterns in the skulls of modern archosaurs reveal that sutures are ambiguous maturity indicators for the Dinosauria. *PLoS One*, 11: e0147687.

    https://doi.org/10.1371/journal.pone.0147687

24. Rivera J, Hosseini MS, Restrepo D, *et al.*, 2020, Toughening mechanisms of the elytra of the diabolical ironclad beetle. *Nature*, 586: 543–548.

25. Arakane Y, Lomakin J, Gehrke SH, *et al.*, 2012, Formation of rigid, non-flight forewings (elytra) of a beetle requires two major cuticular proteins. *PLoS Genet*, 8: e1002682.

    https://doi.org/10.1371/journal.pgen.1002682

26. Fédrigo O, Wray GA, 2010, Developmental evolution: How beetles evolved their shields. *Curr Biol*, 20: R64–R66.

    https://doi.org/10.1016/j.cub.2009.12.012

27. Linz DM, Hu AW, Sitvarin MI, *et al.*, 2016, Functional value of elytra under various stresses in the red flour beetle, *Tribolium castaneum*. *Sci Rep*, 6: 1–10.

    https://doi.org/10.1038/srep34813

28. Tomoyasu Y, Arakane Y, Kramer KJ, *et al.*, 2009, Repeated co-options of exoskeleton formation during wing-to-elytron evolution in beetles. *Curr Biol*, 19: 2057–2065.

    https://doi.org/10.1016/j.cub.2009.11.014

29. Chen PY, 2020, Diabolical ironclad beetles inspire tougher joints for engineering applications. *Nature*, 586: 502–504.

    https://doi.org/10.1038/d41586-020-02840-1

30. Lazarus BS, Velasco-Hogan A, Gómez-del Río T, *et al.*, 2020, A review of impact resistant biological and bioinspired materials and structures. *J Mater Res Technol*, 9: 15705–15738.

    https://doi.org/10.1016/j.jmrt.2020.10.062

31. Huang W, Restrepo D, Jung JY, *et al.*, 2019, Multiscale toughening mechanisms in biological materials and bioinspired designs. *Adv Mater*, 31: 1901561.

    https://doi.org/10.1002/adma.201901561

32. Studart AR, 2016, Additive manufacturing of biologically-inspired materials. *Chem Soc Rev*, 45: 359–376.

    https://doi.org/10.1039/C5CS00836K

33. Gharde S, Surendren A, Korde JM, *et al.*, 2019, Recent advances in additive manufacturing of bio-inspired materials. In: Biomanufacturing, Springer, Berlin, p35–68.

    https://doi.org/10.1007/978-3-030-13951-3_2

34. Dev S, Srivastava R, 2021, Effect of infill parameters on material sustainability and mechanical properties in fused deposition modelling process: A case study. *Prog Addit Manuf*, 6: 631–642.

35. Gu GX, Chen CT, Richmond DJ, *et al.*, 2018, Bioinspired hierarchical composite design using machine learning: simulation, additive manufacturing, and experiment. *Mater Horiz*, 5: 939–945.

    https://doi.org/10.1039/C8MH00653A

36. Dimas LS, Buehler M, 2014, Modeling and additive manufacturing of bio-inspired composites with tunable fracture mechanical properties. *Soft Matter*, 10: 4436–4442.

    https://doi.org/10.1039/C3SM52890A

37. Samykano M, Selvamani S, Kadirgama K, *et al.*, 2019, Mechanical property of FDM printed ABS: Influence of printing parameters. *Int J Adv Manuf Technol*, 102: 2779–

2796.

https://doi.org/10.1007/s00170-019-03313-0

38. Mazzanti V, Malagutti L, Mollica F, 2019, FDM 3D printing of polymers containing natural fillers: A review of their mechanical properties. *Polymers*, 11: 1094.

    https://doi.org/10.3390/polym11071094

39. Cuiffo MA, Snyder J, Elliott AM, *et al.*, 2017, Impact of the fused deposition (FDM) printing process on polylactic acid (PLA) chemistry and structure. *Appl Sci*, 7: 579.

    https://doi.org/10.3390/app7060579

40. Luis E, Pan HM, Sing SL, *et al.*, 2020, 3D direct printing of silicone meniscus implant using a novel heat-cured extrusion-based printer. *Polymers*, 12: 1031.

    https://doi.org/10.3390/polym12051031

41. Velasco-Hogan A, Xu J, Meyers MA, 2018, Additive manufacturing as a method to design and optimize bioinspired structures. *Adv Mater*, 30: 1800940.

    https://doi.org/10.1002/adma.201800940

42. Wang D, Chen D, Chen Z, 2020, Recent progress in 3D printing of bioinspired structures. *Front Mater*, 7: 286.

    https://doi.org/10.3389/fmats.2020.00286

43. Ehrmann G, Ehrmann A, 2021, Investigation of the shape-memory properties of 3D printed PLA structures with different infills. *Polymers*, 13: 164.

    https://doi.org/10.3390/polym13010164

44. Raj SA, Muthukumaran E, Jayakrishna K, 2018, A case study of 3D printed PLA and its mechanical properties. *Mater Today Proc*, 5: 11219–26.

    https://doi.org/10.1016/j.matpr.2018.01.146

45. Kiendl J, Gao C, 2020, Controlling toughness and strength of FDM 3D-printed PLA components through the raster layup. *Compos B Eng*, 180: 107562.

    https://doi.org/10.1016/j.compositesb.2019.107562

46. Rajpurohit SR, Dave HK, 2018, Effect of process parameters on tensile strength of FDM printed PLA part. *Rapid Prototyp J*, 24: 1317–1324.

    https://doi.org/10.1108/RPJ-06-2017-0134

47. Cao Y, Wang W, Wang J, *et al.*, 2019, Experimental and numerical study on tensile failure behavior of bionic suture joints. *J Mech Behav Biomed Mater*, 92: 40–49.

    https://doi.org/10.1016/j.jmbbm.2019.01.001

48. Malik IA, Barthelat F, 2018, Bioinspired sutured materials for strength and toughness: Pullout mechanisms and geometric enrichments. *Int J Solids Struct*, 138: 118–133.

    https://doi.org/10.1016/j.ijsolstr.2018.01.004

49. Miura T, Perlyn CA, Kinboshi M, *et al.*, 2009, Mechanism of skull suture maintenance and interdigitation. *J Anat*, 215: 642–655.

    https://doi.org/10.1111/j.1469-7580.2009.01148.x

50. Standard A, 2014, ASTM D638-14 Standard Test Method for Tensile Properties of Plastics. ASTM International, West Conshohocken, PA.

51. Blaber BA, Antoniou A, 2015, Ncorr: Open-source 2D digital image correlation matlab software. *Exp Mech*, 55: 1105–1122.

52. Peng C, Fox K, Qian M, *et al.*, 2021, 3D printed sandwich beams with bioinspired cores: Mechanical performance and modelling. *Thin Walled Struct*, 161: 107471.

    https://doi.org/10.1016/j.tws.2021.107471

53. Habib F, Iovenitti P, Masood S, *et al.*, 2017, In-plane energy absorption evaluation of 3D printed polymeric honeycombs. *Virtual Phys Prototyp*, 12: 117–131.

    https://doi.org/10.1080/17452759.2017.1291354

54. Kardel K, Ghaednia H, Carrano AL, *et al.*, Experimental and theoretical modeling of behavior of 3D-printed polymers under collision with a rigid rod. *Addit Manuf*, 14: 87–94.

    https://doi.org/10.1016/j.addma.2017.01.004

55. Lee SH, Lee KG, Hwang JH, *et al.*, 2019, Evaluation of mechanical strength and bone regeneration ability of 3D printed kagome-structure scaffold using rabbit calvarial defect model. *Mater Sci Eng C*, 98: 949–959.

    https://doi.org/10.1016/j.msec.2019.01.050

56. Liu L, Jiang Y, Boyce M, *et al.*, 2017, The effects of morphological irregularity on the mechanical behavior of interdigitated biological sutures under tension. *J Biomech*, 58: 71–78.

    https://doi.org/10.1016/j.jbiomech.2017.04.017

Materials Science in Additive Manufacturing

ORIGINAL RESEARCH ARTICLE

Influence of powder morphology on laser absorption behavior and printability of nanoparticle-coated 90W-Ni-Fe powder during laser powder bed fusion

Jingjia Sun, Meng Guo, Keyu Shi, Dongdong Gu*

Jiangsu Provincial Engineering Laboratory for Laser Additive Manufacturing of High-Performance Metallic Components, College of Materials Science and Technology, Nanjing University of Aeronautics and Astronautics, Nanjing, China

Abstract

In this work, mesoscopic simulation and experimental studies were applied to investigate the influence of powder morphology and characteristics on laser absorption behavior and printability of nanoparticle-coated 90W-Ni-Fe powder during laser powder bed fusion (LPBF). The mechanism of laser-material interaction and the thermal behavior of molten fluid during LPBF were revealed, thereby optimizing the powder preparation parameters. It showed that when the powder preparation parameters were optimized (i.e., ball-to-powder weight ratio of 1:2, milling speed of 250 rpm, and milling time of 6 h), the Ni and Fe nanoparticles were uniformly dispersed on W particles and, meanwhile, the sufficiently high sphericity of the W matrix particles was maintained. The nanoparticle-coated 90W-Ni-Fe powder had a sound laser absorption behavior with laser absorptivity of 93.51%, leading to the high LPBF printing quality with a smooth surface free of balling phenomenon and microcracks. Specimen fabricated using optimally prepared powder has a high density of 98% and a low surface roughness of 7.91 μm. The LPBF-processed 90W-Ni-Fe alloys had a uniform hardness distribution with an average value of 439.47 HV_1 and significantly enhanced compression properties with compressive strength of 1255.35 MPa and an elongation of 24.74%. The results in this work provided a physical understanding of complex and interdependent laser-powder interaction and melt pool formation mechanisms during LPBF of W-based alloys that are governed by powder characteristics.

Keywords: Laser powder bed fusion; Powder morphology; Laser absorption behavior; Mechanical properties

1. Introduction

W-Ni-Fe has attracted a great deal of attention in the fields of national defense, industry, and military due to its high density, high melting point, and extremely low thermal expansion coefficient[1,2]. However, at present, they are usually fabricated by conventional powder metallurgy technique based on liquid phase sintering, which is characterized by costly mold cycles and difficulty in completely melting W particles, limiting the application of

***Corresponding author:**
Dongdong Gu
(dongdonggu@nuaa.edu.cn)

Citation: Sun J, Guo M, Shi K, *et al*., 2022, Influence of powder morphology on laser absorption behavior and printability of nanoparticle-coated 90W-Ni-Fe powder during laser powder bed fusion. *Mater Sci Add Manuf.* 1(2): 11. http://doi.org/10.18063/msam.v1i2.11

Received: April 11, 2022

Accepted: May 30, 2022

W-Ni-Fe as a structural material. The rapid development of additive manufacturing (AM) provides a new method for W-Ni-Fe fabrication. AM is defined as a method of printing components from three-dimensional (3D) model data using a layer-wise manufacturing philosophy and can be divided into seven divisions according to printing mechanism and raw material[3]. Laser powder bed fusion (LPBF) is one of the most promising AM technologies due to its laser-induced complete melting mechanism[4,5]. As an efficient, digital, and highly flexible advanced technology, LPBF has been applied in many fields such as military, aerospace, and biomedical, and has a laser beam with high energy to completely melt W particles, making it one of the effective methods to prepare high-performance W-Ni-Fe components[3,6]. Nevertheless, the design of raw materials has become a constraint to the development of LPBF-fabricated W-Ni-Fe parts[3,5,6].

The previous studies indicate that powder properties have an important influence on LPBF-processed W parts. Field *et al.*[7] produced W specimens with two kinds of high-purity W powders: the first powder was a chemically reduced powder with an irregular morphology, and the second powder was a plasma-spheroidized powder with highly spherical morphology. They found that W powders with high sphericity had higher apparent power densities and enhanced the density of LPBF-fabricated W components. A 3D laser absorption model based on ray tracing was established by Zhang *et al.*[8] to investigate the influence of W particle size and its distribution on the powder-to-laser absorptivity and underlying behavior. The simulation and experimental results indicated that the absorptivity of the powder layers considerably exceeded the single powder particle value or the dense solid material value, and smaller particle size improved the laser absorptivity during LPBF-processed W parts. Braun *et al.*[9] analyzed the processing of Mo and W by LPBF, and they identified the oxygen in the powder as a cause for cracks and residual porosity. Nevertheless, these studies mainly focused on pure W, and the effect of feedstock powder characteristics on laser absorption behavior and printing quality of LPBF-processed W-based alloys was rarely studied. It has been reported that nano-reinforcing particles can effectively improve the printing quality of LPBF-fabricated W-based alloys[7,10-12].

Several studies have been carried out on laser absorption and melting behavior during LPBF. Khairallah *et al.*[13] used high-fidelity simulations, coupled with synchrotron experiments, to capture fast multitransient dynamics at the meso-nanosecond scale. They discovered new spatter-induced defect formation mechanisms, which depend on the scan strategy and competition between laser shadowing and expulsion. A recent study by Ge *et al.*[14] proposed mesoscopic simulation to investigate the influence of ceramic addition on the laser energy absorption and powder melting behaviors during LPBF of TiC/Ti6Al4V composites, and they found that the addition of 1 wt.% or 3 wt.% ceramic was beneficial to improving the laser absorptivity and the surface morphology of melted track. A high-fidelity model coupled with a ray-tracing method was constructed by Ren *et al.*[15] to visualize the flow kinetics and reflection behavior during LPBF of Cu-Cr-Zr alloy, which showed good agreement with experiments in terms of track width and depth. The above-mentioned and related studies have reported that laser absorptivity is vital for the subsequent metallurgical behavior and printing quality, and the absorption behavior and liquid-solid interface dynamics during LPBF are affected by the morphology and characteristics of feedstock powder. Understanding the complex and interdependent laser-powder-melt pool interaction during LPBF is of great importance, which matters for the control of metallurgical defects and mechanical properties of LPBF-fabricated W-based parts[8,13,14,16]. However, few studies on laser absorption and melting behavior of W-based powders during LPBF have been reported, and the mechanisms of the influence of powder morphology and characteristics on laser absorption behavior and printability of 90W-Ni-Fe powder during LPBF remain unknown.

The *in situ* alloying of AM, as opposed to pre-alloyed powder used for printing, provides a feasible way for AM with multiple materials. The LPBF, due to its concentrated laser energy input with sufficiently high thermal behavior, is expected to become one of the *in situ* alloying processes in the coming years[17-20]. In this work, the geometrical optical ray-tracing (GO-RT) models and computational fluid dynamics-based powder melting (CFD-PM) models were established to obtain an in-depth understanding of mechanisms during LPBF fabrication of W-based alloys. The nanoparticle-coated 90W-Ni-Fe powders for LPBF were fabricated by mechanical mixing with ball milling, and the corresponding LPBF experiments were carried out. The influence of the powder morphology and characteristics on laser absorption behavior and printability of LPBF 90W-Ni-Fe was investigated by numerical and experimental methods, and the laser-powder interaction mechanism and thermal behavior of molten fluid were revealed. A good agreement was obtained between the simulated and experimental results, and this work provided a physical understanding of complex and interdependent laser-powder-melt pool interaction during LPBF of 90W-Ni-Fe, aiming to form scientific guidance for LPBF fabricating high-quality W-based alloys.

2. Materials and methods

2.1. Powder preparation and LPBF printing

This work utilized the commercial spherical W powder and nano-scale Ni and Fe powder as starting materials (Figure 1), and an E2000 vertical inverter ball mill was used to prepare nanoparticle-coated 90W-Ni-Fe powders with different morphologies. The W powder had a size distribution of D_{10} = 8.25 µm, D_{50} = 14.41 µm, and D_{90} = 24.25 µm, respectively. The laser absorptivity/reflection of different powders was tested using a Shimadzu UV3600 UV-Vis NIR spectrophotometer, and the morphology of different powders was observed using a Hitachi S-4800 field emission scanning electron microscope (SEM).

The LPBF printing device was developed by the Nanjing University of Aeronautics and Astronautics, and the process details were described in our previous work[21]. High-purity argon (99.9%) was used as the protective gas to prevent the formation of oxides, and a chessboard scanning strategy was employed to reduce heat accumulation during LPBF printing[9]. The LPBF processing parameters of 90W-Ni-Fe alloys were laser power of 200 W, scanning speed of 250 mm/s, hatch spacing of 50 µm, and layer thickness of 30 µm. The length of the LPBF-fabricated single tracks was 50 mm, the size of block specimens was 6 mm × 8 mm × 8 mm, and the length to diameter (L/D) of the compression parts was 1.25 (GB/T 7314-2017).

2.2. Microstructure and mechanical properties

The top surface morphologies of 90W-Ni-Fe scanning tracks and block specimens were observed using SEM, and the block specimens were ground and polished according to the standard metallographic procedures and were observed using an XJP-300 optical microscope (OM). The 3D morphology and the surface roughness of 90W-Ni-Fe alloys were obtained using a VK-150K 3D laser microscope imaging system. The microhardness of the optimal 90W-Ni-Fe sample was tested using an HXS-1000 AY microhardness tester with a load setting of 1000 g, and the stress distribution was obtained by a Proto LXRD high-speed X-ray residual stress analyzer. The compression experiment was carried out using a CMT5205 testing machine with a loading rate of 1 mm/min.

2.3. Establishment of GO-RT models

Numerical simulations in this work were based on the mechanism of LPBF (Figure 2A), and a random function was used to generate powder beds in MATLAB (Figure 2B). The geometric information was imported into the optical design and analysis software FRED to form geometric models. After establishing the geometric models, according to Fresnel formulae, the laser reflection behavior was described as[16,22]:

$$\alpha_{p} = 1 - \frac{(n_{c} - 1/\cos\theta) + m_{c}^{2}}{(n_{c} + 1/\cos\theta) + m_{c}^{2}} \quad (1)$$

$$\alpha_{s} = 1 - \frac{(n_{c} - \cos\theta) + m_{c}^{2}}{(n_{c} + \cos\theta) + m_{c}^{2}} \quad (2)$$

where α denotes the absorptivity, θ is the angle of incidence, n_c represents the real part of the complex index of refraction, and m_c represents the imaginary part of the complex index of refraction[14,22]. In this study, the laser refractive behavior of different materials was described by defining the complex index of refraction (Figure 3). Integrating sphere is one of the laser absorption/reflectivity measurement methods (Figure 4A). By the laser absorbance formula:

$$A = 1 - T - R \quad (3)$$

where A denotes the absorption, T is the transmission, and R represents the radiation reflection. The transmitted radiation of metal can be generally regarded as zero[8]. Therefore, the above equation can be simplified as:

$$A = 1 - R \quad (4)$$

this means the absorption of the laser energy can be calculated using the measured reflectivity[14,22]. After obtaining a powder bed with indices defined, a spherical analytical surface was established according to the principle of integrating sphere. At the same time, a Gaussian distributed optical source similar to the LPBF equipment was loaded above the powder bed (Figure 4B). Subsequently, ray tracing was performed in FRED to investigate the laser absorption behavior (Figure 4C and D).

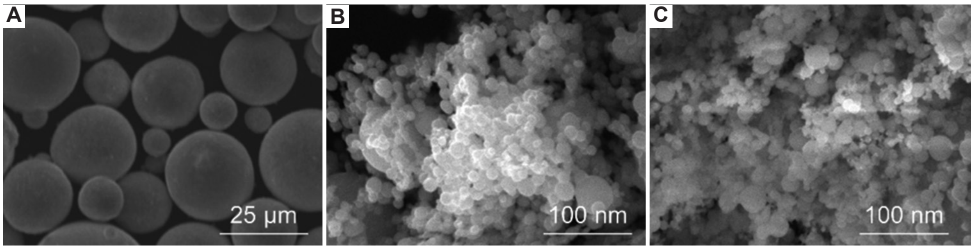

Figure 1. SEM images showing the starting powders: W (A), Ni (B), and Fe (C).

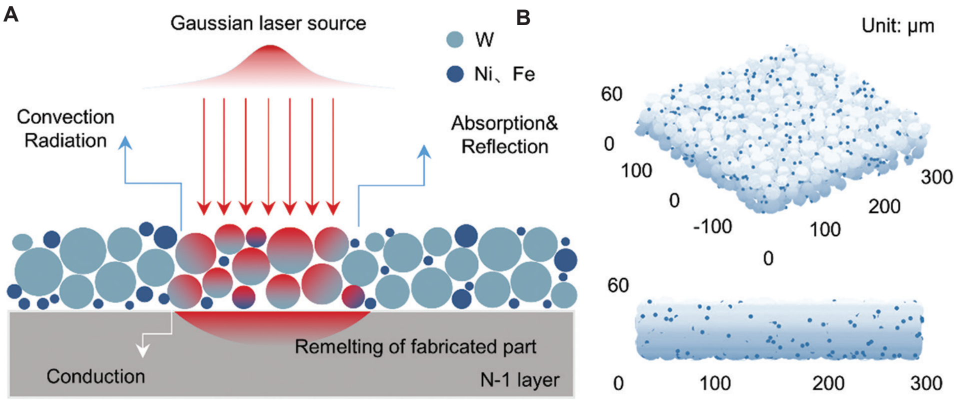

Figure 2. Mechanism of LPBF processing (A) and the algorithmically generated powder bed (B).

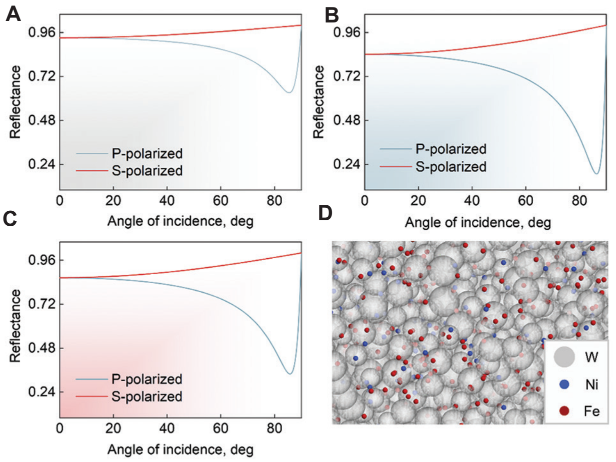

Figure 3. Fresnel formulae for calculating absorptivity for S and P polarization of W (A), Ni (B), and Fe (C), and the powder bed with indices defined (D).

2.4. Establishment of CFD-PM models

Geometric information was also imported into the computational fluid dynamics simulation software FLUENT. During the construction of the CFD-PM model, the laser energy conversion factor of the volumetric Gaussian heat source was set concerning simulation and experimental results. The modified heat flow distribution of the moving Gaussian heat source can be described as[14,23,24]:

$$q=\frac{6PA}{R^2\pi H(1-1/e^3)}\exp\left(\frac{-9(x^2+y^2)}{R^2\log(H/z)}\right) \tag{5}$$

where P is the laser power, R is the spot radius, and is the laser heat source depth. Considering that most of the heat was conducted by the powder bed and solidification layer, the boundary conditions were described as[24]:

$$K\frac{\partial T}{\partial n}+h_c(T\text{-}T_0)+\sigma\varepsilon(T^4-T_0^4)=q \tag{6}$$

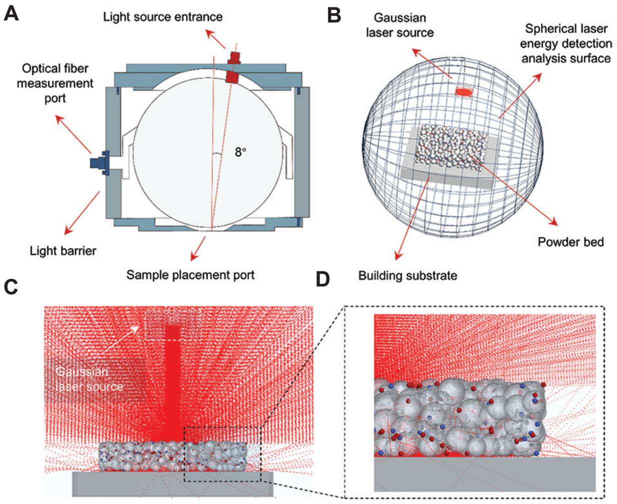

Figure 4. Schematic diagram of integrating sphere (A), GO-RT model with Gaussian laser source and spherical analytical surface (B), and complicated interaction between the powder bed and laser beam (C and D).

where T_0 is the surrounding temperature, h_c is the heat conduction coefficient, σ is the Stefan-Boltzmann constant, and ε is the emissivity. The side and bottom boundaries were settled as insulation boundaries[14]. More modeling details were set concerning existing reports to illustrate the effect of nanoparticle-coated 90W-Ni-Fe powder morphology on the non-uniform melting behavior during LPBF[8,13,14,22-25].

3. Results and discussion

3.1. Effects of nanoparticle-coated 90W-Ni-Fe powder morphologies on the laser absorption behavior

Before establishing models, the morphologies of nanoparticle-coated 90W-Ni-Fe powder were observed. Energy input during the milling process was different under different milling conditions, thus producing nanoparticle-coated 90W-Ni-Fe powder with different morphologies[10,11,25-27]. According to the specific impact energy equation[28]:

$$E_{\mathrm{i}}=\sum_{\mathrm{j}=1}^{n}\frac{1}{2M_{\mathrm{s}}}M_{\mathrm{b}}v_{\mathrm{j}}^{2} \quad (7)$$

where, E_i is the specific impact energy in ball milling, Ms is the mass of powder, M_b is the total mass of grinding balls, v_j is the relative impact velocity between two grinding balls and/or a ball grinding against the grinding bowel wall, and n is the number of collision of a ball against other balls and/or the grinding bowl wall within a second. As can be seen from the above equation, the higher the milling speed or ball-to-powder weight ratio is applied, the higher the impact energy is obtained. The nanoparticle-coated 90W-Ni-Fe powder morphology evolved with the change of milling energy (Figure 5A). Reinforced particles were gradually dispersed uniformly with increased specific impact energy in ball milling, but particle deformation and breakage were more likely to occur (Figure 5B). When the ball-to-powder weight ratio was 1:2, the milling speed was 250 rpm with a milling time of 6 h, the Ni and Fe nanoparticles were uniformly dispersed around W particles, and the sufficiently high sphericity of the W matrix particles was maintained. Combining the above, 3D microscopic GO-RT models with different powder morphologies were established (Figure 6).

The calculated laser absorptivity and their standard deviations are presented in Figure 7. As shown from Figure 7A, the laser absorptivity of the 90W-Ni-Fe powder bed model tended to decrease with the increase of milling energy. The laser absorptivity decreased significantly when the matrix particles were broken or deformed. The standard deviation of calculated laser absorptivity tended to decrease and then increased with the milling energy increasing (Figure 7B). The standard deviation was lowest when the reinforced particles were uniformly distributed and the matrix particles were unbroken or undeformed, indicating that the laser energy conversion factor was high and stable. This was attributed to the improved homogeneity of the powder bed[25,26,29]. When the nanoparticles were agglomerated, the decreased ratio of spot size to irradiated particles promoted the multiple reflections of the laser, improving the laser absorptivity[8]. However, the powder bed was uneven in this case, so the laser energy conversion was instability, which tended to produce highly unstable molten pools, affecting the printing quality of LPBF[8,14,22]. When the matrix particles were broken or deformed, the powder bed had low packing density and high porosity, which weakened the multiple reflections and reduced the laser energy conversion factor, affecting the wetting and spreading of melt during LPBF[8,30,31]. These may cause balling effects and reduce the printing quality of fabricated specimens[8,24,31].

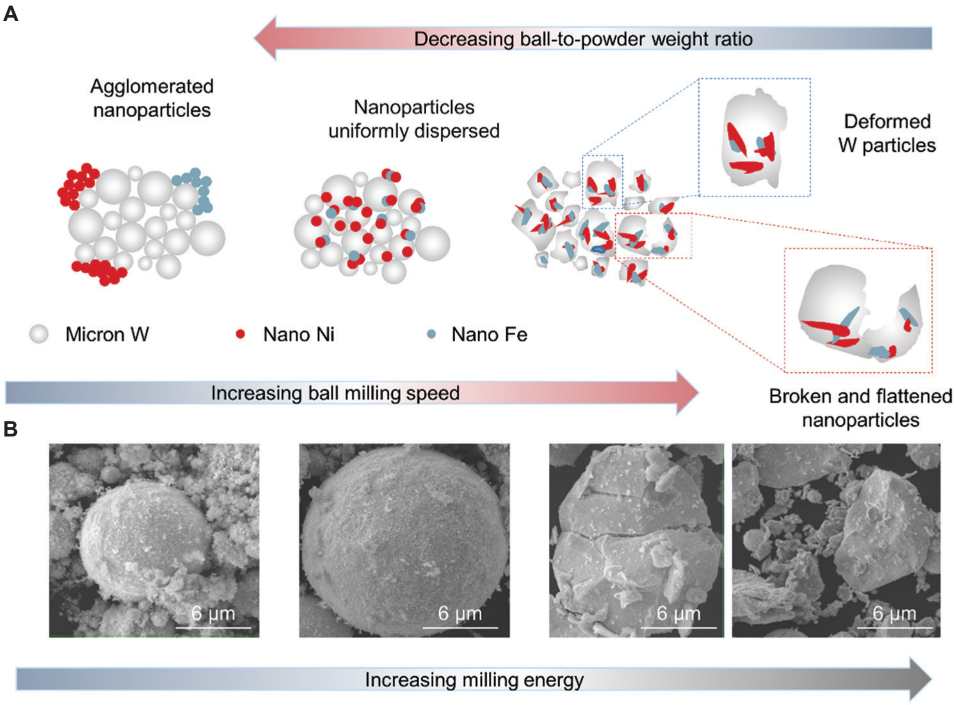

Figure 5. Schematic of the evolution mechanism of nanoparticle-coated powder during ball milling (A) and SEM images showing the different nanoparticle-coated 90W-Ni-Fe powder (B).

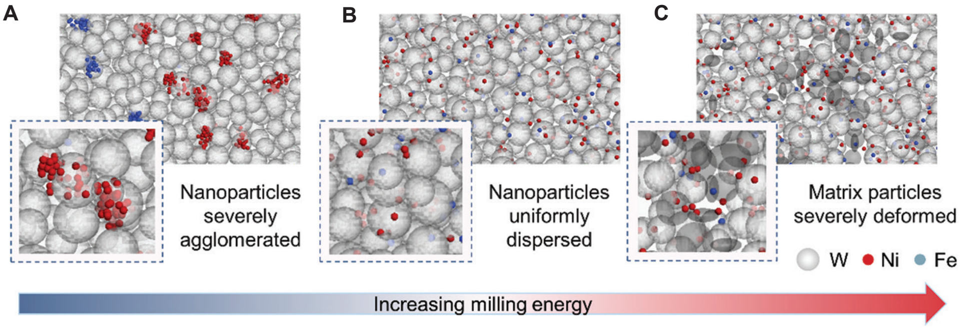

Figure 6. GO-RT models displaying different powder morphologies: severely agglomeration (A), uniformly dispersion (B), and deformation (C).

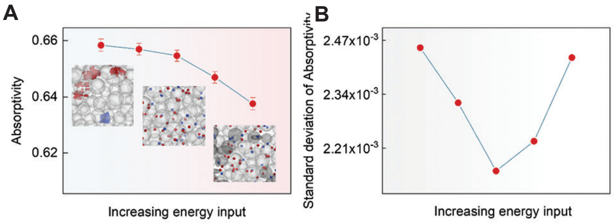

Figure 7. Calculated laser absorptivity of different models (A) and standard deviation of the absorptivity (B).

Moreover, the interaction and penetration of laser beams also have an important influence on the quality of LPBF printing[13,22,25]. To further investigate the effect of powder morphologies on the laser absorption behavior of LPBF, analysis surfaces were established in both horizontal and vertical directions (Figure 8A), which were used to compare spot tracking results and irradiance distribution of different powder bed models. The track spot diagram on the upper surface and the irradiance in the depth direction of the powder bed were shown in Figure 8B, and it can be seen that tracking spots appeared outside the laser spot range due to the optical effect of external diffusion, which promoted heat conduction and thermal radiation[14]. When the nanoparticles were uniformly dispersed and the sphericity of matrix particles was good, the irradiance in the depth direction was the highest and the laser interaction on the upper surface was the strongest. However, when the nanoparticles were agglomerated or the matrix particles were broken or deformed, the laser penetration was lower, and the laser interaction on the surface of the powder bed was weaker. Moreover, the laser beam tracking spot was significantly reduced when agglomerated nanoparticles adhered to matrix particles, which can be regarded as a certain masking effect[14]. When the nanoparticles were agglomerated, the laser absorptivity of the powder bed was the highest, but most of the energy acted on nanoparticles, which weakened the interaction between matrix particles and laser, reducing the laser energy acting on matrix particles[25,26].

The above shows that homogeneous nanoparticle-coated 90W-Ni-Fe powder with high sphericity has the best laser absorption behavior. Agglomerated nanoparticles make beams reflecting between nanoparticles and reduce the stability of absorption, and deformed particles weaken the multiple reflections and reduce the laser absorptivity and penetration.

To verify the above simulation results, the laser absorptivity/reflection of nanoparticle-coated powders with different morphologies were tested (Figure 9). Two sets of nanoparticle-coated 90W-Ni-Fe powders with different morphologies were prepared at different milling speeds or ball-to-powder weight ratios. The energy in ball milling increased with the increase of ball-to-powder weight ratio or milling speed as shown in equation VII[28]. As seen in Figure 9, the laser absorptivity of different nanoparticle-coated 90W-Ni-Fe powders decreased with the increase of milling energy. Moreover, it decreased significantly when the milling energy was too high (matrix particle deformed). The trend of experimental results was consistent with simulation, indicating that the homogeneous nanoparticle-coated powder with high sphericity has sound laser absorption behavior with laser absorptivity of 93.51%. Similar to what has been reported, the values of measured laser absorptivity have a certain increment compared with simulation[16]. This can be attributed to the balance between complexity and reality when constructing the model, the nanoparticles in the model are less than the actual, so the ratio of spot size to the number of irradiated particles is increased, reducing the laser absorptivity[8,22]. At the same time, the actual W powder has a higher surface roughness than particles in the model, which also increases the measured laser absorptivity[8,14,16,22]. Although the calculated laser absorptivity of models is lower, the models still reflect the laser absorption behavior during LPBF. Moreover, these models can visualize some phenomena which are often challenging to observe in real-time in a mesoscopic view, providing a relatively in-depth physical analysis of laser

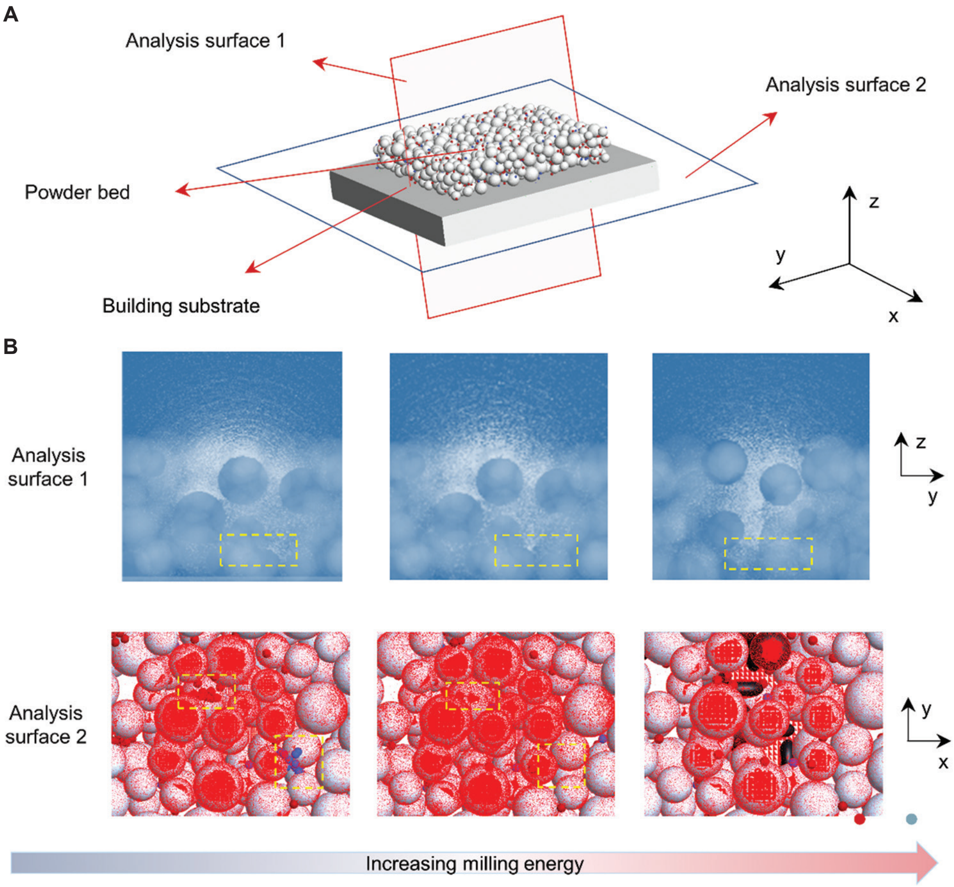

Figure 8. The analysis surfaces creating the energy irradiance in powder beds (A), and the track spot diagram of each laser ray on the surface of powder beds (B).

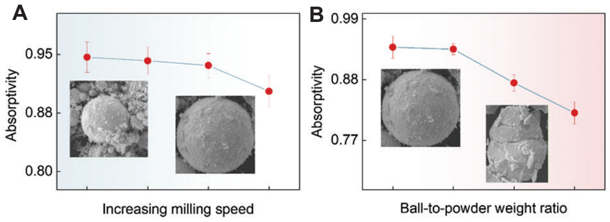

Figure 9. Absorptivity of milled nanoparticle-coated 90W-Ni-Fe powder at different milling speeds (A) and ball-to-powder weight ratios (B).

absorption behavior during LPBF fabricating W-based alloys.

3.2. Effects of nanoparticle-coated 90W-Ni-Fe powder morphologies on printability

During LPBF fabricating, the powder particles undergo complex laser-material interactions[13]. The laser absorptivity/reflection, the number of laser interactions, and the irradiation depth predict the efficiency of the laser energy utilization of the powder bed[14,22]. The laser utilization efficiency influences the molten pool formation, evaporation, Marangoni effect, and recoil pressure, which determine the printing quality of LPBF-processed components[8,14,22,24,25]. Hence, the change in laser absorption behavior due to the nanoparticle-coated 90W-Ni-Fe powder morphology is of great importance. To further reveal the influence of nanoparticle-coated 90W-Ni-Fe powder morphology on the printability, the CFD-PM single track simulation clouds (Figure 10A-C) and SEM images of LPBF-fabricated 90W-Ni-Fe scanning tracks (Figure 10D-F) were obtained. The W particles reached their melting point when the Ni and Fe particles had already reached their boiling points. Due to such a huge difference between W and Ni-Fe phases, only the W matrix particles were shown in the CFD-PM simulation clouds, the effect of enhanced particles was reflected by changing laser energy conversion factors. The melting behavior and surface quality of LPBF-fabricated single track of 90W-Ni-Fe were sensitive to the morphology of powder feed as presented in Figure 10. The LPBF scanning track was relatively straight when the reinforcing particles were uniformly distributed and the matrix particles maintained good sphericity (Figure 10B and E), which can be attributed to the high and relatively stable laser absorption of the powder layer[24-26]. The fully melted particles and stable molten pool improved the wetting and spreading of liquid metal, enhancing the surface quality of the LPBF-processed parts[14,25]. Comparatively, with enhanced particles agglomerated (Figure 10A and D), the LPBF 90W-Ni-Fe single track had a fluctuated boundary. This can be attributed to the high and uneven laser absorption behavior which caused the nonuniform spreading[11,24,26]. When the matrix particles were broken or deformed, the LPBF scanning track morphology changed to irregular shapes (Figure 10F), and the balling effects were observed (Figure 10C), which can be attributed to the increase in viscosity. When the temperature of the laser-irradiated zone is higher than the melting point of W, the viscosity of the W droplet can be defined as[30]:

$$\eta_{\mathrm{d}}(T)=0.108\exp\left(\frac{1.28\times10^{5}}{RT}\right) \tag{8}$$

where n_d is the viscosity of the W droplet, R is the gas constant (equal to 8.31 J·mol^{-1}·K^{-1}), and the temperature T ranges of 3350–3700 K. From the above equation, the higher the molten pool temperature, the lower the W droplet viscosity. The previous studies indicated that there is a competing mechanism for the wetting, spreading, and solidification of W droplets during LPBF[31]. Due to the low laser absorptivity of the powder layer with deformed matrix particles, the molten pool cannot absorb enough laser energy, reducing the temperature of the droplet. This increased the viscosity of the droplet and they solidified before spreading sufficiently, resulting in the balling effects. This phenomenon is detrimental to interlayer bonding and tends to affect the densification behavior during LPBF[31,32].

Before LPBF fabrication, a computer-aided design model of the part is processed by software to plan the laser path line-by-line[4,33]. Therefore, the quality of the scanning track is of great importance to metallurgical bonding and the surface quality of fabricated components[6,14,24]. To further investigate the effect of nanoparticle-coated 90W-Ni-Fe powder morphology on LPBF printing quality, SEM images of the upper surfaces, and morphology of the side surfaces of different fabricated 90W-Ni-Fe alloys are presented in Figure 11. It can be seen that the evolution of the powder morphology does affect the surface quality of LPBF-processed specimens due to the changes in dynamic viscosity. LPBF processing involves the flow and solidification of liquid metal in the molten pool; the dynamic viscosity n_f of the molten pool is defined as[29]:

$$\eta_{\mathrm{f}}=\frac{16}{15}\sqrt{\frac{m}{kT}}\sigma \tag{9}$$

where m is the atomic mass, k is the Boltzmann constant, T is the temperature of the molten pool, and σ is the surface tension. The previous studies indicated that the surface tension is higher when the molten pool temperature is lower[21]. Therefore, the higher the molten pool temperature, the lower the dynamic viscosity. The laser

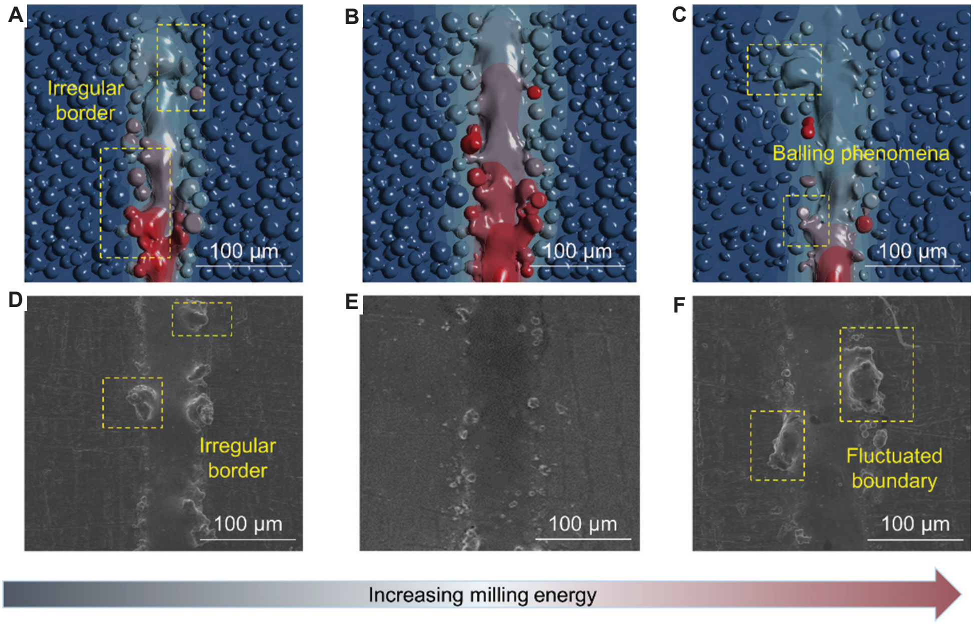

Figure 10. Simulated single-track morphologies (A-C) and SEM images showing as-fabricated 90W-Ni-Fe scanning tracks (D-F) with powders of different morphologies: severely agglomeration (A and D), uniformly dispersion (B and E), and deformation (C and F).

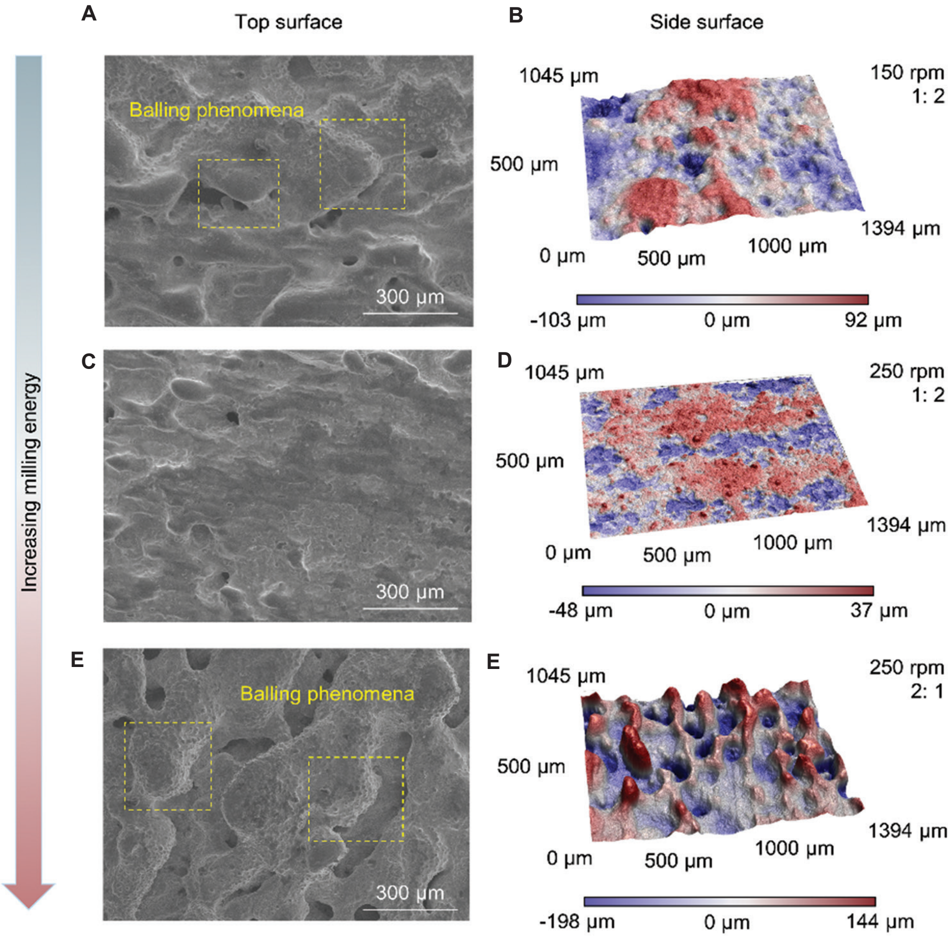

Figure 11. SEM images showing top surface morphologies (A, C, and E) and 3D morphologies describing the side surface (B, D, and F) of LPBF-processed 90W-Ni-Fe alloys fabricated by different powder: severely agglomeration (A and B), uniformly dispersion (C and D), and deformation (E and F).

energy conversion factor of the homogeneous powder with good sphericity was high and stable, lowering the dynamic viscosity of the molten pool, and yielding a sufficient liquid lifetime for wetting and spreading behavior[14,24]. Hence, the spattering and balling effects were reduced, improving the surface quality of LPBF-fabricated 90W-Ni-Fe parts. In this instance, the surface roughness (S_a) of the fabricated specimen was 7.91 μm. When the enhanced particles were agglomerated or the matrix particles were deformed, the surface roughness (S_a) of the fabricated specimen was 20.05 μm and 29.41 μm, respectively. This can be attributed to the unstable laser absorption behavior which reduced the stability of the molten pool, leading to the splashing and balling effects, reducing the surface quality of the LPBF-processed specimens[14,24-26].

The stability of the molten pool also tends to affect the densification behavior of LPBF-fabricated 90W-Ni-Fe alloys, which has an important influence on its mechanical properties[4,13,34]. To investigate the effects of powder morphologies on the densification level of LPBF-processed 90W-Ni-Fe parts, OM images of specimens fabricated by different powders were observed (Figure 12). The densification level of the specimens increased and then decreased as the milling energy increased. Homogeneous powder with high sphericity had the highest densification level (density of 98%). This was attributed to the fact that homogeneous nanoparticle-coated 90W-Ni-Fe powder with high sphericity had the best laser absorption behavior, thus improving the wetting and spreading behavior of LPBF[29,30]. The trends of results obtained from the single tracks and bulk fabrications were correlated. With the high quality of the scanning track, the metallurgical bonding of processed specimens improved, thereby increasing the density of the fabricated W-Ni-Fe specimen.

The above results show that the powder morphology does influence the LPBF printing quality of 90W-Ni-Fe alloys and homogeneous powder with high sphericity has the sound laser absorption behavior; these help with obtaining the best LPBF printability. Meanwhile, a good agreement is obtained between the simulated and experimental results.

3.3. Mechanical properties of the optimal 90W-Ni-Fe alloys

The above analysis shows that optimal specimens can be obtained by homogeneous nanoparticle-coated 90W-Ni-Fe powder with high sphericity. The density of LPBF-fabricated specimens has an important influence on their microhardness and residual stress distribution[25,35]. Figure 13 presented the microhardness and residual stress distribution of the optimal specimen. The average Vickers hardness and residual stress of the 90W-Ni-Fe specimen were 439.47 HV_1 and 501.85 MPa, respectively. The dispersion of hardness values was smaller than reported, which was attributed to the high densification level of the specimen[2]. When the load was applied to the surface of the specimen, there was no obvious collapse due to its high densification level[36]. It is shown from Figure 13B that compressive stress was uniformly distributed inside the specimen. This can be attributed to the rapid melting-solidification process during LPBF, which produced solidification shrinkage, and the shrinkage can be expressed as[37]:

$$\frac{d(\Delta L/L_0)}{d_t} = \frac{\Delta P_f \varepsilon_d}{D_G \eta} \tag{10}$$

where ΔP is the capillary pressure, D_G is the grain radius, ε_d is the liquid thickness, and n is the viscosity of the liquid. The optimized 90W-Ni-Fe powder formed a homogeneous powder bed, making the solidification shrinkage rate at different positions similar. Hence, the residual stress was uniformly distributed in the specimen and the gradient of residual stress was small.

The residual stress generated by the heating-cooling thermal cycle of the LPBF processing is one of the key factors affecting the properties of fabricated parts. It has been reported that LPBF-processed specimens with smaller residual stress gradients are less prone to deformation, so they have better mechanical properties[35,37]. The compressive stress-strain curve of the testing part fabricated by optimized powder was presented in Figure 14. The compressive strength of the 90W-Ni-Fe part was 1255.35 MPa with an elongation of 24.74%, which was higher than the reported LPBF-fabricated W specimen (compressive strength of 902 MPa with an elongation of 6.4%)[38]. To reveal the strengthening mechanisms, the microstructures of LPBF-processed W and W-Ni-Fe along the building direction were shown in Figure 15. The microstructures of LPBF-processed W consisted of large columnar grains. With the addition of nano Ni and Fe, the microstructures of the fabricated specimen presented the equiaxial columnar grains, and the cracks were significantly reduced. The

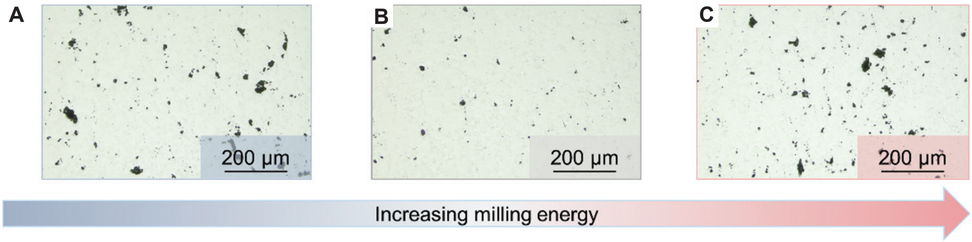

Figure 12. OM images showing LPBF-processed alloys fabricated by different nanoparticle-coated 90W-Ni-Fe powder: severely agglomeration (A), uniformly dispersion (B), and deformation (C).

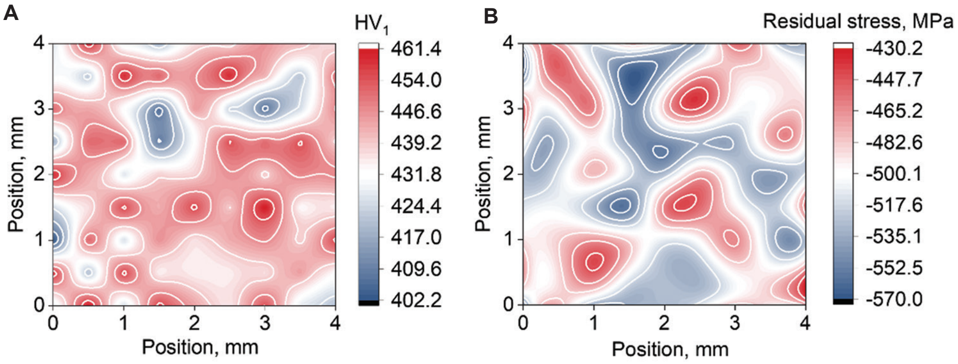

Figure 13. Hardness (A) and residual stress (B) distribution of LPBF-processed sample fabricated by optimized nanoparticle-coated 90W-Ni-Fe powder.

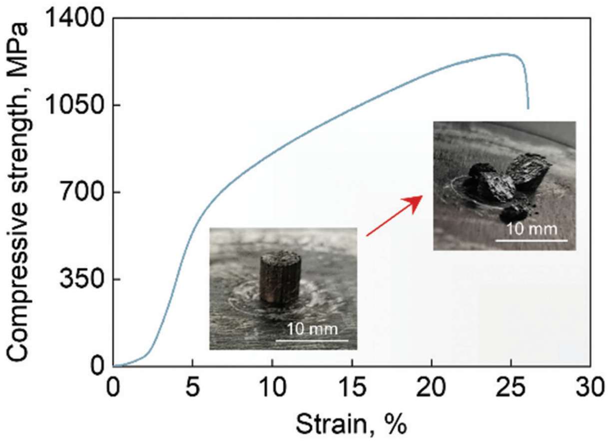

Figure 14. Compressive stress-strain curve of LPBF-processed part fabricated by optimized nanoparticle-coated 90W-Ni-Fe powder.

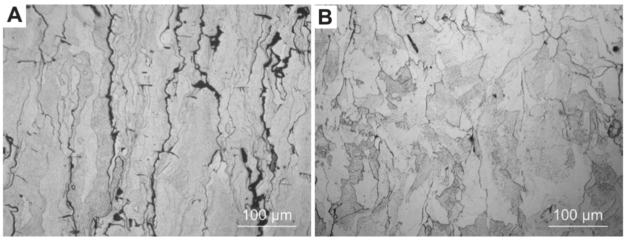

Figure 15. Microstructures of LPBF-processed W (A) and W-Ni-Fe (B) specimens.

improvement of compressive strength was attributed to the transformation of the microstructure from columnar to equiaxial grains when the Ni and Fe nanoparticles were added to the W matrix. As the surfaces of W particles were coated with Ni and Fe, the continuous growth of W grains was prevented and the growth of the equiaxial grains was promoted instead. Meanwhile, the nanoparticles were diffused to the grain boundaries due to their strong activity, reducing the microcracks and resultant grain boundary strengthening. The microstructures directly determined the mechanical properties of the final parts, thereby improving the mechanical properties of LPBF-fabricated W-Ni-Fe alloys.

4. Conclusion

Through numerical and experimental investigations, this study examined the effects of nanoparticle-coated 90W-Ni-Fe powder morphology on the laser absorption behavior and the printing quality of LPBF. GO-RT models and CFD-PM models were first established to obtain an in-depth understanding of mechanisms during LPBF fabrication of W-based alloys. Nanoparticle-coated 90W-Ni-Fe powders were prepared and corresponding alloys were fabricated by a self-developed device. Based on the above discussion and results, several conclusions can be drawn:

(i) It was discovered that the morphology of nanoparticle-coated 90W-Ni-Fe powder prepared by different milling conditions was different; this was attributed to the difference in milling energy caused by different milling parameters. Reinforced particles were gradually dispersed uniformly with increased specific impact energy in ball milling, but particle deformation and breakage were more likely to occur.

(ii) Powder morphology was optimized to obtain stable laser absorption behavior with high absorptivity in both horizontal and vertical directions of the powder bed. Homogeneous nanoparticle-coated 90W-Ni-Fe powder with good sphericity had the best laser absorption behavior. Agglomerated nanoparticles made laser beams reflect between nanoparticles and reduced the stability of laser absorption behavior. Deformed matrix particles weakened the multiple reflections and lowered laser absorptivity and penetration.

(iii) Laser absorption of nanoparticle-coated 90W-Ni-Fe powder with different morphologies was different, thus making their LPBF printability different. Homogeneous nanoparticle-coated 90W-Ni-Fe powder with good sphericity had the best LPBF printability with a straight scanning track free of balling effects, which had a good agreement with modeling results.

(iv) The 90W-Ni-Fe alloys fabricated by optimized powder had the best surface quality (surface roughness of 7.91 μm), the highest densification level (density of 98%), and uniform residual stress distribution. Moreover, the 90W-Ni-Fe alloys had a uniform hardness distribution with an average value of 439.47 HV_1, and they had better compression properties (compressive strength of 1255.35 MPa with an elongation of 24.74%) compared with LPBF-processed pure W parts.

Acknowledgments

None.

Funding

This work was supported by the Science Challenge Project (No. TZ2018006-0301-02 and No. TZ2018006-0303-03), National Natural Science Foundation of China for Creative Research Groups (Grant No. 51921003), The 15th Batch of "Six Talents Peaks" Innovative Talents Team Program (No. TD-GDZB-001), The Fundamental Research Funds for the Central Universities (NO. NC2020004), and Basic Strengthening Program (No. 2019-JCJQ-JJ-331).

Conflict of interest

Jingjia Sun, Meng Guo, Keyu Shi, and Dongdong Gu declare that they have no (potential) conflicts or competing interests with any institutes, organizations, or agencies that might influence the integrity of results or objective interpretation of their submitted works.

Author contributions

Conceptualization: Dongdong Gu
Data curation: Jingjia Sun, Meng Guo
Formal analysis: Dongdong Gu, Jingjia Sun, Meng Guo
Funding acquisition: Dongdong Gu
Investigation: Dongdong Gu, Jingjia Sun, Meng Guo
Methodology: Jingjia Sun, Meng Guo, Keyu Shi
Project administration: Dongdong Gu, Meng Guo
Resources: Dongdong Gu
Software: Jingjia Sun, Keyu Shi, Meng Guo
Supervision: Dongdong Gu, Meng Guo
Validation: Dongdong Gu, Jingjia Sun, Meng Guo
Visualization: Dongdong Gu, Jingjia Sun, Meng Guo, Keyu Shi
Writing – original draft: Jingjia Sun
Writing – review and editing: Dongdong Gu, Meng Guo.

References

1. Ivekovic A, Montero-Sistiaga ML, Vanmeensel K, *et al.*, 2019, Effect of processing parameters on microstructure and properties of tungsten heavy alloys fabricated by SLM. *Int J Refract Met Hard Mater*, 82: 23–30.

   http://doi.org/10.1016/j.ijrmhm.2019.03.020

2. Li JF, Wei ZY, Zhou BK, *et al.*, 2019, Densification, microstructure and properties of 90W-7Ni-3Fe fabricated by selective laser melting. *Metals Basel*, 9: 884.

   http://doi.org/10.3390/met9080884

3. Thompson MK, Moroni G, Vaneker T, *et al.*, 2016, Design for additive manufacturing: Trends, opportunities, considerations, and constraints. *Cirp Ann-Manuf Techn*, 65: 737–760.

   http://doi.org/10.1016/j.cirp.2016.05.004

4. Gu DD, Shi XY, Poprawe R, *et al.*, 2021, Material-structure-performance integrated laser-metal additive manufacturing. *Science*, 372: eabg1487.

   http://doi.org/10.1126/science.abg1487

5. Bourell DL, Rosen DW, Leu MC, 2014, The roadmap for additive manufacturing and its impact. *3D Print Addit Manuf*, 1: 6–9.

   http://doi.org/10.1089/3dp.2013.0002

6. Schmidt M, Merklein M, Bourell D, *et al.*, 2017, Laser based additive manufacturing in industry and academia. *Cirp Ann-Manuf Techn*, 66: 561–583.

   http://doi.org/10.1016/j.cirp.2017.05.011

7. Field AC, Carter LN, Adkins NJ, *et al.*, 2020, The effect of powder characteristics on build quality of high-purity tungsten produced via laser powder bed fusion (LPBF). *Metall Mater Trans A*, 51: 1367–1378.

   http://doi.org/10.1007/s11661-019-05601-6

8. Zhang JY, Gu DD, Yang Y, *et al.*, 2019, Influence of particle size on laser absorption and scanning track formation mechanisms of pure tungsten powder during selective laser melting. *Engineering*, 5: 736–745.

   http://doi.org/10.1016/j.eng.2019.07.003

9. Braun J, Kaserer L, Stajkovic J, *et al.*, 2019, Molybdenum and tungsten manufactured by selective laser melting: Analysis of defect structure and solidification mechanisms. *Int. J Refract Met Hard Mater*, 84: 104999.

   http://doi.org/10.1016/j.ijrmhm.2019.104999

10. AlMangour B, Grzesiak D, Yang JM, 2017, Selective laser melting of TiB2/316L stainless steel composites: The roles of powder preparation and hot isostatic pressing post-treatment. *Powder Technol*, 309: 37–48.

    http://doi.org/10.1016/j.powtec.2016.12.073

11. AlMangour B, Grzesiak D, Yang JM, 2018, *In situ* formation of TiC-particle-reinforced stainless steel matrix nanocomposites during ball milling: Feedstock powder preparation for selective laser melting at various energy densities. *Powder Technol*, 326: 467–478.

    http://doi.org/10.1016/j.powtec.2017.11.064

12. Hu ZP, Zhao YN, Guan K, *et al.*, 2020, Pure tungsten and oxide dispersion strengthened tungsten manufactured by selective laser melting: Microstructure and cracking mechanism. *Addit Manuf*, 36: 101579.

    http://doi.org/10.1016/j.addma.2020.101579

13. Khairallah SA, Martin AA, Lee JR, *et al.*, 2020, Controlling interdependent meso-nanosecond dynamics and defect generation inmetal 3D printing. *Science*, 368: 660–665.

    http://doi.org/10.1126/science.aay7830

14. Ge Q, Gu DD, Dai DH, *et al.*, 2021, Mechanisms of laser energy absorption and melting behavior during selective laser melting of titanium-matrix composite: role of ceramic addition. *J Phys D Appl Phys*, 54: 115103.

    http://doi.org/10.1088/1361-6463/abcdce

15. Ren ZH, Zhang DZ, Fu G, *et al.*, 2021, High-fidelity modelling of selective laser melting copper alloy: Laser reflection behavior and thermal-fluid dynamics. *Mater Design*, 207: 109857.

    http://doi.org/10.1016/j.matdes.2021.109857

16. Boley CD, Mitchell SC, Rubenchik AM, *et al.*, 2016, Metal powder absorptivity: Modeling and experiment. *Appl Opt*, 55: 6496–6500.

http://doi.org/10.1364/ao.55.006496

17. Mosallanejad MH, Niroumand B, Aversa A, *et al.*, 2021, *In-situ* alloying in laser-based additive manufacturing processes: A critical review. *J Alloys Compd*, 872: 159567.

    http://doi.org/10.1016/j.jallcom.2021.159567

18. Huang S, Narayan RL, Tan JH, *et al.*, 2021, Resolving the porosity-unmelted inclusion dilemma during *in-situ* alloying of Ti34Nb via laser powder bed fusion. *Acta Mater*, 204: 116522.

    http://doi.org/10.1016/j.actamat.2020.116522

19. Zhang XH, Xiao Z, Yu WH, *et al.*, 2022, Influence of erbium addition on the defects of selective laser-melted 7075 aluminium alloy. *Virtual Phys Prototyping*, 17: 406–418.

    http://doi.org/10.1080/17452759.2021.1990358

20. Sing SL, Huang S, Goh GD, *et al.*, 2021, Emerging metallic systems for additive manufacturing: *In-situ* alloying and multi-metal processing in laser powder bed fusion. *Prog Mater Sci*, 119: 100795.

    http://doi.org/10.1016/j.pmatsci.2021.100795

21. Guo M, Gu DD, Xi LX, *et al.*, 2019, Selective laser melting additive manufacturing of pure tungsten: Role of volumetric energy density on densification, microstructure and mechanical properties. *Int J Refract Met Hard Mater*, 84: 105025.

    http://doi.org/10.1016/j.ijrmhm.2019.105025

22. Yang Y, Gu DD, Dai DH, *et al.*, 2018, Laser energy absorption behavior of powder particles using ray tracing method during selective laser melting additive manufacturing of aluminum alloy. *Mater Design*, 143: 12–19.

    http://doi.org/10.1016/j.matdes.2018.01.043

23. Xia MJ, Gu DD, Yu GQ, *et al.*, 2016, Selective laser melting 3D printing of Ni-based superalloy: Understanding thermodynamic mechanisms. *Sci Bull*, 61: 1013–1022.

    http://doi.org/10.1007/s11434-016-1098-7

24. Dai DH, Gu DD, Ge Q, *et al.*, 2020, Mesoscopic study of thermal behavior, fluid dynamics and surface morphology during selective laser melting of Ti-based composites. *Comput Mater Sci*, 177: 109598.

    http://doi.org/10.1016/j.commatsci.2020.109598

25. Lin KJ, Fang YM, Gu DD, *et al.*, 2021, Selective laser melting of graphene reinforced titanium matrix composites: Powder preparation and its formability. *Adv Powder Technol*, 32: 1426–1437.

    http://doi.org/10.1016/j.apt.2021.03.003

26. Zhuang J, Gu DD, Xi LX, *et al.*, 2020, Preparation method and underlying mechanism of MWCNTs/Ti6Al4V nanocomposite powder for selective laser melting additive manufacturing. *Powder Technol*, 368: 59–69.

    http://doi.org/10.1016/j.powtec.2020.04.041

27. Attar H, Prashanth KG, Zhang LC, *et al.*, 2015, Effect of powder particle shape on the properties of In Situ Ti-TiB composite materials produced by selective laser melting. *J Mater Sci Technol*, 31: 1001–1005.

    http://doi.org/10.1016/j.jmst.2015.08.007

28. Mio H, Kano J, Saito F, *et al.*, 2004, Optimum revolution and rotational directions and their speeds in planetary ball milling. *Int J Miner Process*, 74: S85–S92.

    http://doi.org/10.1016/j.minpro.2004.07.002

29. Gu DD, Shen YF, 2009, Effects of processing parameters on consolidation and microstructure of W-Cu components by DMLS. *J Alloys Compd*, 473: 107–115.

    http://doi.org/10.1016/j.jallcom.2008.05.065

30. Paradis PF, Ishikawa T, Yoda S, 2005, Viscosity of liquid undercooled tungsten. *J Appl Phys*, 97: 106101.

    http://doi.org/10.1063/1.1896432

31. Zhou X, Liu XH, Zhang DD, *et al.*, 2015, Balling phenomena in selective laser melted tungsten. *J Mater Process Technol*, 222: 33–42.

    http://doi.org/10.1016/j.jmatprotec.2015.02.032

32. Zhang DQ, Cai QZ, Liu JH, *et al.*, 2011, Research on process and microstructure formation of W-Ni-Fe alloy fabricated by selective laser melting. *J Mater Eng Perform*, 20: 1049–1054.

    http://doi.org/10.1007/s11665-010-9720-3

33. DebRoy T, Wei HL, Zuback JS, *et al.*, 2018, Additive manufacturing of metallic components process, structure and properties. *Prog Mater Sci*, 92: 112–224.

    http://doi.org/10.1016/j.pmatsci.2017.10.001

34. Martin JH, Yahata BD, Hundley JM, *et al.*, 2017, 3D printing of high-strength aluminium alloys. *Nature*, 549: 365–369.

    http://doi.org/10.1038/nature23894

35. Li C, Liu ZY, Fang XY, *et al.*, 2018, Residual stress in metal additive manufacturing. *Procedia CIRP*, 71: 348–353.

    http://doi.org/10.1016/j.procir.2018.05.039

36. Abbas MA, Yan AR, Wang ZY, 2021, On the use of EBSD and microhardness to study the microstructure properties of tungsten samples prepared by selective laser melting. *Materials*, 14: 1215.

    http://doi.org/10.3390/ma14051215

37. Zhu HH, Lu L, Fuh JY, 2004, Influence of binder's liquid volume fraction on direct laser sintering of metallic powder. *Mat Sci Eng A-Struct*, 371: 170–177.

    http://doi.org/10.1016/j.msea.2003.11.048

38. Gu DD, Guo M, Zhang HM, *et al.*, 2020, Effects of laser scanning strategies on selective laser melting of pure tungsten. *Int J Extrem Manuf*, 2: 025001.

    http://doi.org/10.1088/2631-7990/ab7b00

WHIOCE PUBLISHING PTE. LTD.
Materials Science in Additive Manufacturing

ORIGINAL RESEARCH ARTICLE

Multi-objective optimization of intense pulsed light sintering process for aerosol jet printed thin film

Guo Liang Goh[1†], Haining Zhang[2†], Guo Dong Goh[1], Wai Yee Yeong[1*], Tzyy Haur Chong[3,4]

[1]Singapore Centre for 3D Printing, School of Mechanical and Aerospace Engineering, Nanyang Technological University, Singapore

[2]Department of Intelligent Manufacturing, School of Information Engineering, Suzhou University, Suzhou, China

[3]Singapore Membrane Technology Centre, Nanyang Environment & Water Research Institute, Nanyang Technological University, Singapore

[4]School of Civil and Environmental Engineering, Nanyang Technological University, Singapore

Abstract

The sintering of printed nanoparticle films is a necessary processing step for most nanoparticle inks to make the printed film functional. The sintering of nanoparticle is usually performed through thermal sintering, photonic sintering, induction sintering, etc. Intense pulsed light (IPL) sintering method is one of the most popular sintering methods for nanoparticle inks due to the fast and effective process, but it may yield mediocre performance if improper sintering parameters are used. In this work, we investigate the correlation between the two factors which are the print passes of aerosol jet printing and the sintering distance of the samples on the effect of the surface morphology and sheet resistance. A contradictory correlation between the two factors was observed and a multi-objective optimization was carried out using machine learning method to identify the most optimum conditions for both factors. We found that multi-objective optimization approach is effective in reducing the conflicting responses, thus the sintered thin film can have low sheet resistance and low surface roughness. This work provides an essential guide for achieving conductive films with electrical conductivity and low surface roughness using IPL sintering process for fast fabrication of multi-layered electronics such as electrochemical electrodes.

Keywords: Additive manufacturing; 3D printing; Printed electronics; Multi-objective optimization; Photonic sintering; Process optimization

1. Introduction

In the past decade, printed electronics technology has received great attention because of the increasing needs for alternative electronics fabrication technology to produce unconventional electronics, especially in the field of flexible and stretchable electronics[1,2]. Conventionally, electronics are manufactured using silicon wafer

---

[†]These authors contributed equally to this work

***Corresponding author:**
Wai Yee Yeong
(wyyeong@ntu.edu.sg)

Citation: Goh GL, Zhang H, Goh GD, *et al*., 2022, Multi-objective optimization of intense pulsed light sintering process for aerosol jet printed thin film. *Mater Sci Add Manuf*. 1(2): 10.

http://doi.org/10.18063/msam.v1i2.10

Received: March 31, 2022

Accepted: May 10, 2022

technology that requires high processing temperature which poses restrictions on the material options[3]. In contrast, printed electronics technology uses functional inks to create circuits and electronic components, thereby lowering the process temperature and creating more opportunities for new electronic architectures with various substrates, particularly for low thermal stability substrates[4-7]. It has allowed for new opportunities for the creation of flexible electronic components that can be used in applications such as water technology for system health monitoring purpose[8].

In the early years, printed electronics is normally done using traditional additive-based printing techniques that require tool, mask, or stencil for the patterning of inks[9]. These traditional printing techniques include screen printing, gravure printing, flexographic printing, and offset printing. These techniques are compatible with the roll-to-roll manufacturing process and allow the use of flexible substrates, which makes them highly suitable for mass production of flexible electronics. However, the recent shift in the industry's needs for custom-made electronics has spurred the search for cheaper alternatives for electronic fabrication because of the high initial cost for the tools and stencils renders the traditional printing techniques uneconomic for such purpose. In contrast, three-dimensional (3D) printing, also known as additive manufacturing, is found to be a better option for the fabrication of highly customizable advanced electronics[10]. At present, 3D printing techniques such as inkjet printing[11], aerosol jet printing[12-15], and direct ink writing[16] have been increasingly used by the industry to manufacture advanced electronics that require fine resolution and sophisticated geometry. Among which, aerosol jet printing technique has gained much attraction over the years due to its capability to process a wide range of materials and the high printing resolution[17]. Besides, it can also be used to integrate electronics on 3D structures, making it suitable for realizing novel electronic designs[18].

Regardless of the printing techniques, the functional inks remain the key ingredient to achieving the low processing temperature for printed electronics[19,20]. To date, various types of functional inks such as silver nanoparticle inks, gold nanoparticles inks, and silver nanowire inks have been developed to cater for different applications[4,21,22]. Functional inks generally contain several components, namely, the active material, the solvent, the binder, the surfactant, and other additives[20]. The active materials and binder made up the main materials of the printed layers that determine the type and property of the layers, whereas the other materials such as the solvent, surfactant, and other additives will be removed in the sintering process.

In general, a sintering treatment is required to process the printed ink layers in order to make the active materials functional[23]. This is because the active materials are normally covered with a layer of organic stabilizer, which impedes their functionality. Sintering treatment removes the organic stabilizer layer and binds the active materials together. For the case of metal nanoparticle, the nanoparticles receive energy during the sintering process and fuse together and grow larger to form a conductive network of nanoparticles. Besides, sintering treatment also enhances the adhesion of the printed materials to the substrates. Till now, there are many different sintering techniques that have been developed such as thermal sintering[24], electrical sintering[25], induction sintering[26], and photonic sintering[27]. Each sintering technique offers its unique advantages and possesses certain limitations. For examples, thermal sintering treatment can achieve homogeneous sintering but may not be suitable for all substrates as the substrate will be exposed to the same sintering condition. In contrast, induction sintering and electrical sintering offer selective sintering of nanoparticle layers, but only work with metallic inks and require pre-thermal treatment to make them conductive.

Intense pulsed light (IPL) sintering is a type of photonic sintering method that uses pulses of high intensity light to sinter the nanoparticle inks[28]. The process uses a xenon lamp that emits a broad spectrum of light with wavelength ranges from visible light to UV light as the energy source[29-31]. Unlike other sintering techniques, IPL sintering can be done in a very short time and does not induce significant damage to the substrates. The performance of the IPL sintering technique depends on various factors such as the light intensity, the type of substrates, the ink composition, the light absorption of the nanoparticle, and the thickness of the printed film. Despite the advantages of IPL technique, it is widely known that the process can cause defects such as cracks and delamination of the printed film due to the rapid vaporization of the gases originating from the organic compounds[32]. These defects can cause undesirable and inconsistent performance of the electrical circuit or electronics components. Severe delamination can also restrict the use of the IPL-sintered conductive film for multilayer electronic designs which requires additional insulating or functional layers atop of the printed conductive film such as the case of electrochemical sensing electrodes. Although this issue can be solved by using back irradiation rather than top irradiation, it is only limited to transparent substrate[31] and does not address the issue for some samples that requires top irradiation. Although preheating the samples is found to be helpful in reducing delamination in certain cases, it may not solve the issue entirely for thicker samples[33].

In this work, we explore the use of IPL sintering technique for sintering aerosol jet printed silver nanoparticle film for printed electronics applications. Although there have been many works that investigate the effect of various process parameters on the performance silver nanoparticle film[34-39], no study has investigated the interplay between the sintering parameters and film thickness on the quality and the performance of the sintered film. The objective of this work is to find out the process window of the IPL sintering process to achieve crack-free films with low sheet resistance for aerosol jet printed film with different thicknesses. To better analyze the correlation between different factors such as sintering distance and print passes on the surface morphology and electrical property of the printed film, a multi-objective optimization method was adopted. Here, a modified central composite design (CCD) was used to study the relationships between the quality of the sintered films and the main printing and sintering parameters. Analysis of variance (ANOVA) was conducted to examine individual effects and the interactions of the main variables on the sheet resistance and surface roughness of the sintered thin films. The results of analysis suggest that the CCD-derived models are statistically meaningful. The modified CCD-derived models were then optimized by a desirability function method, and a 2-dimensional (2D) optimal printing and sintering window were determined to yield thin film with low sheet resistance and low surface roughness. Following that, the derived statistical models were jointly driven with a non-dominated sorting genetic algorithm (GA) to systematically optimize the conflicting responses in a more robust manner. The findings demonstrate the effectiveness of the suggested multi-objective optimization approach in reducing the conflicting responses. This work presents useful guide for future attempts to optimize the IPL sintering parameters for various nanoparticle-based film such as gold for good electrical conductivity and low surface roughness for fast fabrication of multi-layered electronics such as electrochemical electrodes.

2. Materials and methods

2.1. Materials

The silver nanoparticle ink that was used in this work is UT Dots Ag40TE purchased from UT Dots®. The silver nanoparticle is reported to have an average particle diameter of 10 nm and it is dispersed in proprietary solvents. The optimum sintering temperature of the ink using conventional thermal sintering method is claimed to range from 150°C to 200°C for at least 30 min. For the substrate, Kapton® polyimide films with a thickness of 75 µm were used for the fabrication of test coupons. Polyimide substrate was used in this work because it is widely used in the field of printed electronics for the fabrication of flexible electronics and wearables due to the good material property and thermal compatibility. The polyimide substrate was first cleaned with soap water and ethanol to remove the inorganic and organic contaminants on its surface. This was done to ensure that the surface wettability of the surface was uniform to ensure consistent print quality and film adhesion. No surface modification was done on the polyimide substrate.

2.2. Fabrication of test coupons

Each test coupon is made up of four conductive thin film printed on polyimide films which can ensure at least a sample size of $n = 3$ for each test condition for statistically meaningful analysis. The diameter of the coupon is 1 cm. The tool path for the print head is designed to have a line pitch of 120 µm to ensure sufficient overlapping between the adjacent lines for formation of homogeneous film. A spiral tool path design was used for the 1 cm diameter circles. The printing of ink was done using an Optomec™ Aerosol jet® 5X system (Figure 1A). Ultrasonic atomizer was used for the printing of silver ink. For good printability, the process parameters for printing the silver ink onto the polyimide film were optimized to be as follows: sheath flow = 20 standard cubic centimeters per minute (sccm), atomizer flow = 50 sccm, ultrasonic atomizer current = 0.6 A, print speed = 10 mm/s, and the substrate temperature = 80°C.

2.3. Intense pulse light sintering of printed silver film

The sintering of the printed silver nanoparticle film was carried out using a Xenon™ S-1000 pulsed light system. The IPL sintering system consists of a tabletop controller, a sintering chamber, and an air-cooled lamp housing (Figure 1B). The lamp operating voltage ranges from 2.25 to 3.80 kV. The generated pulsed light has a pulse duration of 520 µs and a pulse energy ranging from 290 to 830 Joules/pulse depending on the lamp operating voltage. The in-house-made sintering chamber consists of a chamber that houses the sintering lamp and a height-adjustable stage. The chamber serves to prevent stray light from entering the lab and the height-adjustable stage allows for the adjustment of pulse light intensity by controlling the distance of the sample from the light source. As the light intensity varies spatially, all the test coupons are placed at the center of the stage and sintered with five light pulses to ensure consistency.

2.4. Characterization methodology

Characterization of the printed film was performed to generate information that can be used for the optimization

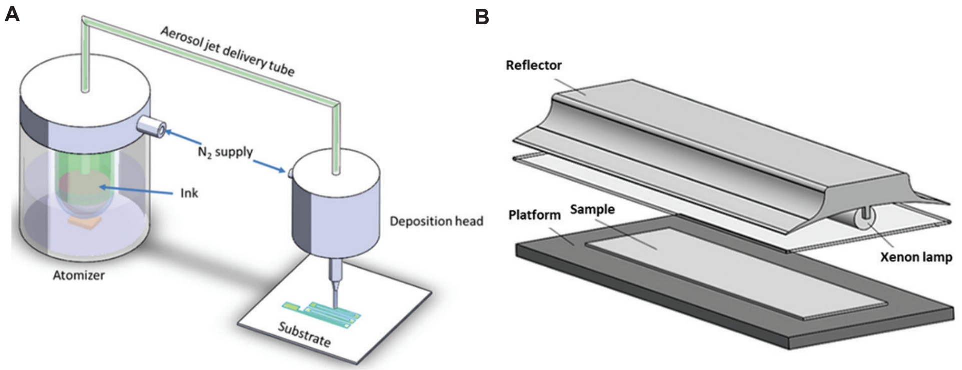

Figure 1. (A) Aerosol jet printing system (Reprinted with permission from[40]. Copyright (2019) American Chemical Society. (B) Intense pulsed light system.

process. In this work, electrical property and the degree of delamination are the two main optimization objectives. As such, electrical property characterization and surface roughness characterization were conducted to provide information about the sheet resistance and the degree of delamination of the sintered film, respectively.

The electrical property was measured using a Lucas Labs Pro 4 collinear probe station with a Keithley 2400 source meter unit. The measurements were done with the collinear probes placed at the center of each printed circular film. In this work, sheet resistance was used to characterize the electrical property of the sintered film for a few reasons. First, it is almost impossible to calculate the resistivity of the sintered film with swelling and delamination morphology as the cross section of the film cannot be determined accurately using the equation $\rho = RA/L$ (R: resistance, A: cross-sectional area, and L: length) due to the non-uniform cross-sectional area[32]. Second, as IPL sintering usually results in non-uniform sintering across the depth, sheet resistance was used in this study instead of electrical resistivity because sheet resistance is more meaningful in terms of reflecting the actual electrical property of the IPL-sintered films with different thicknesses. Furthermore, this allows electrical circuit designers and engineers to easily determine the number of print passes without the need for quantifying the film thickness.

The surface roughness characterization was performed using a Keyence VK-X200 confocal microscope coupled with a ×10 magnification lens. The region of interest was selected to be at the center of the circular film. As the dimensions of a single scan region is approximately 1500 µm × 1000 µm, this can result in biased and selective sampling. To avoid this, a large scanning region was created by stitching nine different scan regions. This resulted in a scanned region with a dimension of 4500 µm × 3000 µm, which can better reflect the overall surface condition over the sintered film. The severity of the delamination can be described by the surface roughness parameters. It should be noted that different surface roughness parameters are often used to describe different types of defects or surface anomaly. For instance, R_a measures the average deviation of the surface over a sampling area (Figure 2A), R_z measures the maximum deviation of the surface over a sampling area (Figure 2B), and R_{ku} measures the fourth power of the root mean square deviation to display the dimensionless fourth power of the sampling area (Figure 2C).

Each of these roughness parameters has its pros and cons in terms of describing the severity of the delamination. For example, R_a is useful for describing the overall severity of the delamination but difficult to pick up small or localized delamination, whereas R_z is useful for describing localized out-of-plane delamination but tend to overestimate the delamination severity of localized defects in relation to the overall surface condition. R_{ku}, on the other hand, is useful for differentiating different defect morphologies. As the delamination of the sintered film can happen in various ways, it is vital to use different surface roughness parameters such as R_a, R_z, and R_{ku} to account for the different modes of delamination. However, for the ease of the optimization process and analysis, a single surface roughness indicator is preferred over many different surface roughness parameters. As such, we have adopted a surface roughness indicator, S, as a linear sum of the normalized surface roughness parameters multiplied by their assigned weights. In this case, we defined the surface roughness indicator, $S = w_1\tilde{R}_a + w_2\tilde{R}_z + w_3\tilde{R}_{ku}$ with $0 < S < 1, w_1 + w_2 + w_3 = 1$. Each surface roughness parameter was normalized with the highest values of respective surface roughness parameters ($R_{a,max}$ = 25.6 µm, $R_{x,max}$ = 370.1 µm, $R_{ku,max}$ = 172.0 µm) within the sample populations, and the weights for each surface parameter are the same ($w_1 = w_2 = w_3 = 1/3$) to ensure equal contributions to the surface roughness indicator, S. To illustrate the correlation between the adopted surface roughness indicator and the actual sintered film condition, six different sintered films obtained using different process parameters were used and their corresponding surface roughness was analyzed as shown in Figure 3. A qualitative comparison using reconstructed confocal scans of the sintered films can be found on Figure S1 of the supplementary document. The *S* value was calculated based on the equation as described earlier. The surface roughness parameter for each coupon was obtained based on the average surface roughness parameters (R_a, R_z, and R_{ku}) of 3 regions of approximately equal size, as shown in Figure 3.

These six sintered films are randomly selected (from 105 samples) simply to illustrate the different types of delamination mode and severity. In general, the surface

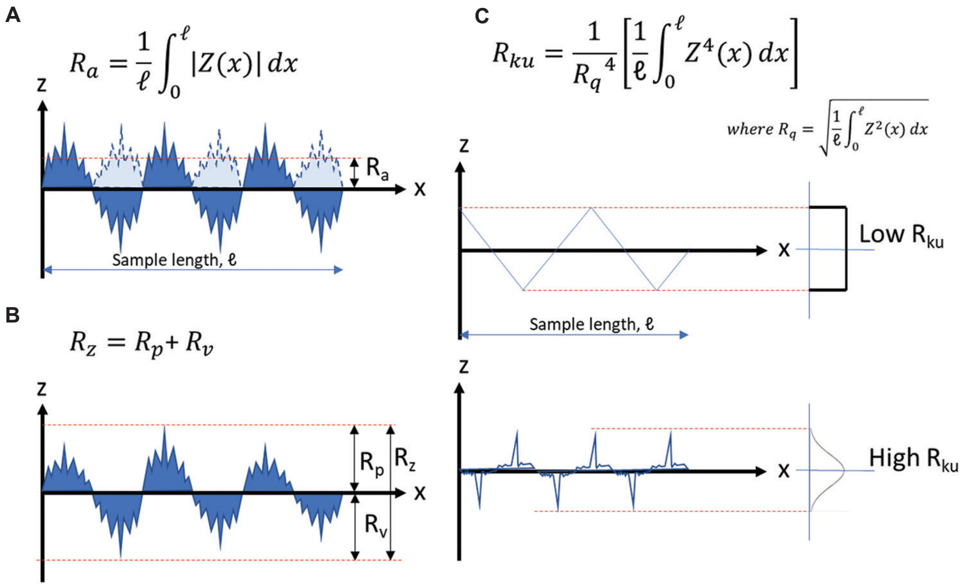

Figure 2. Definition of different surface roughness parameters. (A) R_a, (B) R_z, and (C) R_{ku}[41].

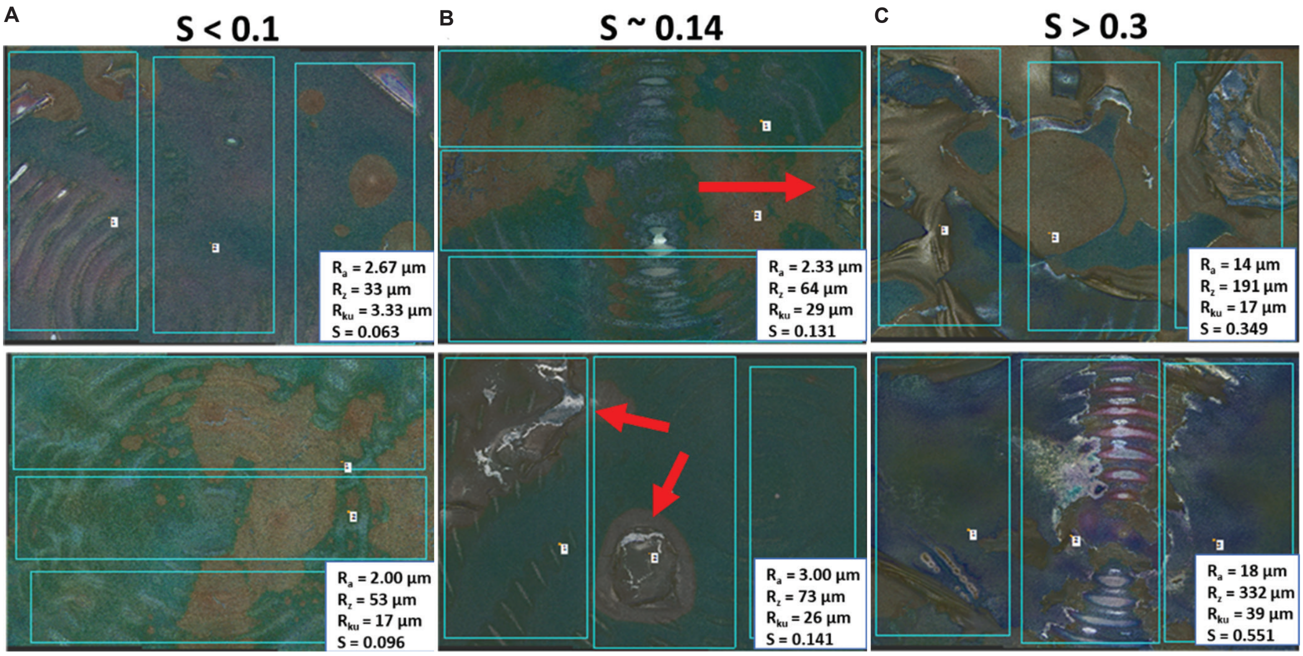

Figure 3. Correlation between surface roughness indicator and the severity of delamination of the sintered film. (A) Coupons with *S* <0.1 contains no delamination, (B) coupons with *S*≈itho suffer mild delamination, and (C) coupons with *S*>0.3 have severe delamination issue. Turquoise lines show the sub-sampling region for each coupon.

roughness indicator can be used to differentiate the delamination of sintered film effectively. For instance, for the sintered film with no obvious delamination, the surface roughness indicator normally falls below 0.1 (S<0.1) as shown in the two optical images (two different coupons) in Figure 3A. For the moderately delaminated film which has small, localized delamination, they normally fall in the range between 0.1 and 0.25. Figure 3B shows the two different coupons that contain small, localized surface anomalies with a surface roughness indicator, S close to 0.14. Finally, Figure 3C shows the coupons with severe delamination issue with a surface roughness indicator value of higher than 0.3.

2.5. Design of experiment

To investigate the effect of the photonic sintering parameters on the conductive ink printed with different thicknesses, two factors were considered in this study, namely, (1) the sintering distance, which directly influences the light intensity received by the conductive ink, and (2) the number of layers of the conductive ink, which determines the thickness of the conductive film, t (Figure 4), were varied. The correlation between the number of printed layers and the film thickness can be determined using linear regression as shown in Figure 4. In essence, the greater number of print passes will lead to more material being deposited onto the substrate, resulting in thicker films. This correlation is useful for estimating the average electrical resistivity, ρ_{ave} of the sintered films with the obtained sheet resistance, R_s using the equation, $\rho_{ave}=R_s \cdot t$.

The conditions that were taken into consideration in this study are shown in Table 1. The conductive films were printed in different number of layers (1–5). Three samples were printed for each film thickness (number of layers). For each film thickness, the sintering distance was varied from 40 to 70 with a step increment of 5 (7 levels). Hence, a total of 105 (7 × 5 × 3) samples were printed in this study.

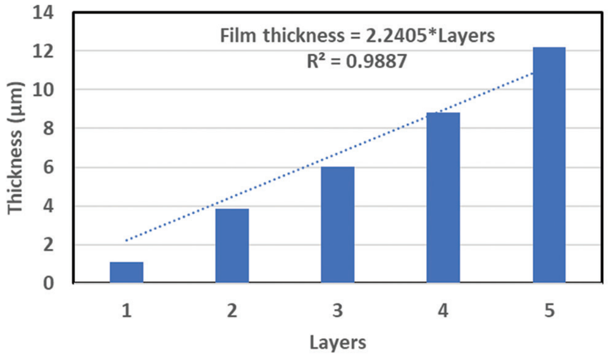

Figure 4. Relationship between film thickness and number of printed layers.

Table 1. Conditions considered in this study

Sintering distance (cm)	40, 45, 50, 55, 60, 65, 70
Number of layers	1, 2, 3, 4, 5

2.6. A desirability function approach

Here, a desirability function approach was used to transform the two response variables (number of layers and sintering distance) into a single response variable function in 2D design space. The optimal sintering process parameters could then be effectively evaluated by minimizing the single response function. To assess the desirability of the contradicting responses quantitatively, each independent response y_i is converted into an individual desirability function, d_i. The desirability function, d_i, changes within the range [0,1], where $d_i = 0$ indicates the independent response y_i is beyond the satisfactory range, and $di = 1$ implies the independent response y_i achieves its target value. Depending on whether a specified response y_i is required to be reduced or increased, different desirability function d_i is utilized accordingly.

For minimizing a particular response, the desirability function can be quantitatively calculated by a Smaller-The-Better criteria (Eq. 1):

$$d_i = \begin{cases} 0 & y_i > U \\ \left(\dfrac{y_i - U}{L - U}\right)^r & L \le y_i \le U \\ 1 & y_i < L \end{cases} \qquad \text{(Eq.1)}$$

where U and L symbolize the maximum value and minimum value of a target response, respectively. r is the user-specified parameter (r>0) to indicate the shape of desirability function d_i, discussion and descriptive figures on the different choices of r are described by Wang *et al.*[42].

Then, the transformed individual desirability functions can be merged into a single response variable function (desirability function D) as shown in Eq. 2 to calculate the overall desirability of the contradicting responses:

$$D = \left((d_1)^{u_1} (d_2)^{u_2} \cdots (d_n)^{u_n}\right)^{\frac{1}{\sum u_i}} \qquad \text{(Eq.2)}$$

where u_i are user-specified weights of the i-th response (i=1,...,n) and n is the number of individual responses. Following that, a statistical software Design-Expert® was used to ascertain the optimal process parameters by maximizing the single response of the overall desirability function.

2.7. GA-based multi-objective optimization

GA is a heuristic global optimization method inspired by the theory of biological evolution where the generated new population can effectively receive the characteristics of the best solutions of the precedent[43]. Besides that, due to capability of simultaneously evaluating a set of generations rather than individual solution, the GAs can converge fast and have been widely used in various research areas for multi-objective optimization[44,45]. A GA usually consists of three key phases: crossover, mutation and selection. Specifically, during the multi-objective optimization process, the genetic operations of crossover and mutation can be utilized to encourage the variety of the generated offspring[46]. Following that, the selection operator will be adopted to evaluate and choose best solutions from a set of generations. Although the methodologies of selection can be classified into different types, including tournament-based selection and proportional selection, a non-dominated sorting GA III (NSGA-III) was employed to optimize the conflicting responses in this research[47,48], which reduced the contradiction between the responses in an objective manner.

The relationship between varying factors (number of layers and sintering distance) and the resulting responses (sheet resistance and surface roughness indicator) was formed by fitting the data using response surface method (RSM). The reduced cubic model and the reduced sixth model were used for the sheet resistance and the surface roughness indicator, respectively. For simplicity, surface roughness was used in place of surface roughness indicator for the rest of the discussion. The ANOVA technique was used to study the significance of the main effects (A: Sintering distance and B: Number of print layers) and the interactions on the responses. The probability of *F* value greater than calculated *F* value due to noise is indicated by *P*-value. $P < 0.05$ signifies the corresponding design parameter has effect on the mechanical property. ANOVA results (Table 2) reveal that both sintering distance and number of print layers have significant impact on the sheet resistance of the sintered film, registering *P*-value smaller than 0.0001 for the main effects. It was also noted that the interactions AB and AB^2 also registered $P = 0.0045$ and 0.0108, respectively, indicating there is a combined effect of the factors on the sheet resistance, or in other words, the effect of one factor is dependent on the level of the other factor.

For the surface roughness, ANOVA results (Table 3) reveal that both sintering distance and number of print layers have significant impact on the surface roughness of the sintered film, registering *P*-values of smaller than 0.0001 and 0.0009, respectively. It was found that most of the interactions were found to be significant up to the sixth order, with a few exceptions for A^2B, A^3B, B^4, and A^4B, registering $P = 0.3618$, 0.7594, 0.061, and 0.1762, respectively. The higher order of interactions indicates that the response is highly non-linear.

Table 2. ANOVA results for sheet resistance

Source	*F*-value	*P*-value
Model	44.50	<0.0001
A-Sintering distance	50.30	<0.0001
B-Print layers	128.39	<0.0001
AB	8.45	0.0045
A^2	0.5021	0.4803
B^2	3.48	0.0650
AB^2	6.75	0.0108
A≥	4.39	0.0387
Residual		
Lack of Fit	1.07	0.3961
R^2	0.7625	
Adjusted R^2	0.7454	
Predicted R^2	0.7185	
Adeq Precision	21.7425	

To check the model accuracy, the residuals of the derived models were computed by studentized residuals in standard deviation units. The normal probability of the studentized residuals for the target responses are presented in Figure 5, as the studentized residuals scattered along a straight line with little deviation, the modeling results are statistically acceptable. Furthermore, Figure 6 shows the model residuals versus test orders. As the residuals spread randomly around the center line without noticeable trend, they are considered independent from each other, thus excluding the effect of the test orders on the derived CCD models.

Figure 7 demonstrates the predicted sheet resistance and surface roughness versus actual printed sheet resistance and surface roughness, and the diagonal line drawn in Figure 7 is x (actual value) = y (predicted value). The high R^2 and Adeq. precision values suggests that the input-output relationship between the sintering process parameters and the sheet resistance and surface roughness are successfully recorded by the derived CCD models. Based on the ANOVA results, the input-output relationship for the responses of sheet resistance, R_s, and surface roughness, R_{SR}, with coded units for sintering process can be expressed as follows:

- $ln\ (R_s \times 10^4) = -11.21 + 1.21A - 0.6126B - 0.2357AB + 0.0704A^2 + 0.1705B^2 - 0.3562AB^2 - 0.3894A^3$
- $ln\ R_{SR} = -0.9469 + 2.45A + 0.7624B - 2.42AB + 2.53A^2 - 2.03B^2 - 0.5648A^2B - 1.36AB^2 - 5.94A^3 + 0.5038B^3 + 0.9995A^2B^2 - 0.5000A^3B + 3.04AB^3 - 11.02A^4 +$

Table 3. ANOVA results for surface roughness

Source	*F*-value	*P*-value
Model	41.00	<0.0001
A-Sintering distance	57.09	<0.0001
B-Print layers	11.86	0.0009
AB	13.17	0.0005
A^2	3.48	0.0657
B^2	18.74	< 0.0001
A^2B	0.8409	0.3618
AB^2	18.14	< 0.0001
$A\geq$	30.57	< 0.0001
$B\geq$	4.53	0.0362
A^2B^2	23.99	< 0.0001
$A\geq B$	0.0944	0.7594
$AB\geq$	23.35	< 0.0001
A^4	7.85	0.0063
B^4	3.61	0.0610
$A\geq B^2$	15.63	0.0002
$A^2B\geq$	2.69	0.1049
A^4B	1.86	0.1762
A^5	12.60	0.0006
$A\geq B\geq$	17.61	< 0.0001
A^5B	5.58	0.0205
A^6	7.32	0.0083
Residual		
Lack of Fit	1.82	0.0569
R^2	0.9121	
Adjusted R^2	0.8898	
Predicted R^2	0.8600	
Adeq Precision	21.2984	

$$0.7784B^4 + 1.51A^3B^2 - 0.6597A^2B^3 + 0.6386A^4B + 2.86A^5 - 3.16A^3B^3 + 2.70A^5B + 7.24A^6$$

where the high levels of the factors are coded as +1 and the low levels are coded as −1.

It can be seen from Figure 8A that the slope of the gradient for the sheet resistance over the number of print layers increases as the sintering distance becomes larger. It is observed that at lower number of print layers, the effect of the sintering distance on the sheet resistance is extremely prominent, in which larger sintering distance gives rise to higher sheet resistance. The effect becomes less prominent as the number of print layers increases.

The surface roughness does not scale linearly with the print layers nor the sintering distance (Figure 8B). A global peak is observed at print layer equal to three and sintering distance of 60 cm. The surface roughness drops sharply as the print layer reduces to 1 or sintering distance approaches 70 cm. The decrease is less drastic at higher print layers and sintering distance lower than 60 cm.

For high quality sintered film, both the sheet resistance and the surface roughness should be low. From Figure 9A, the sheet resistance is lowest in the region of high numbers of print layers and small sintering distance. The surface roughness, on the other hand, is lower at small number of print layers or at sintering distance of 70 cm (Figure 9B). The conflicting relationship results in a need to reach a compromise between the two parameters.

To identify the optimum condition for high quality sintered film, a desirability function approach was used (Eq. 2), where the multiple response variables were merged into a single response function established on a certain metric. In the overall desirability function, the weights of sheet resistance and surface roughness were initialized with the same value.

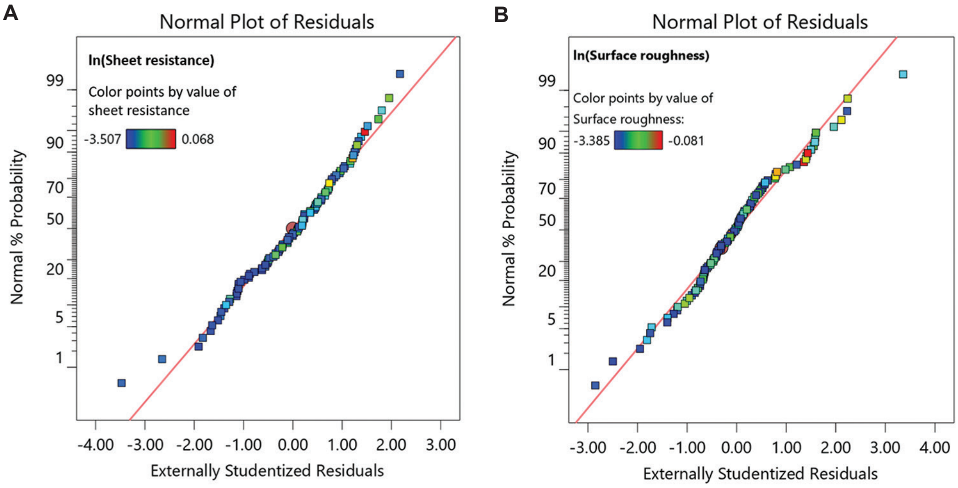

Figure 5. Normal probability plots of the residuals for (A) sheet resistance and (B) surface roughness.

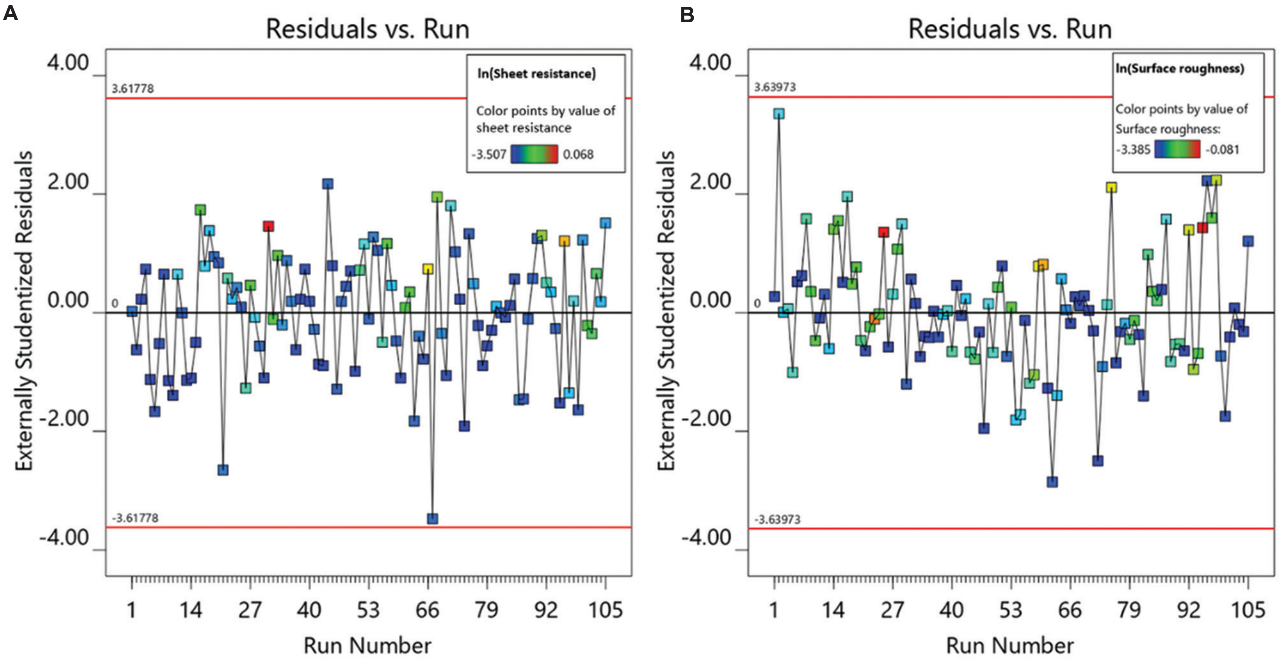

Figure 6. Model residuals versus test orders for (A) sheet resistance and (B) surface roughness.

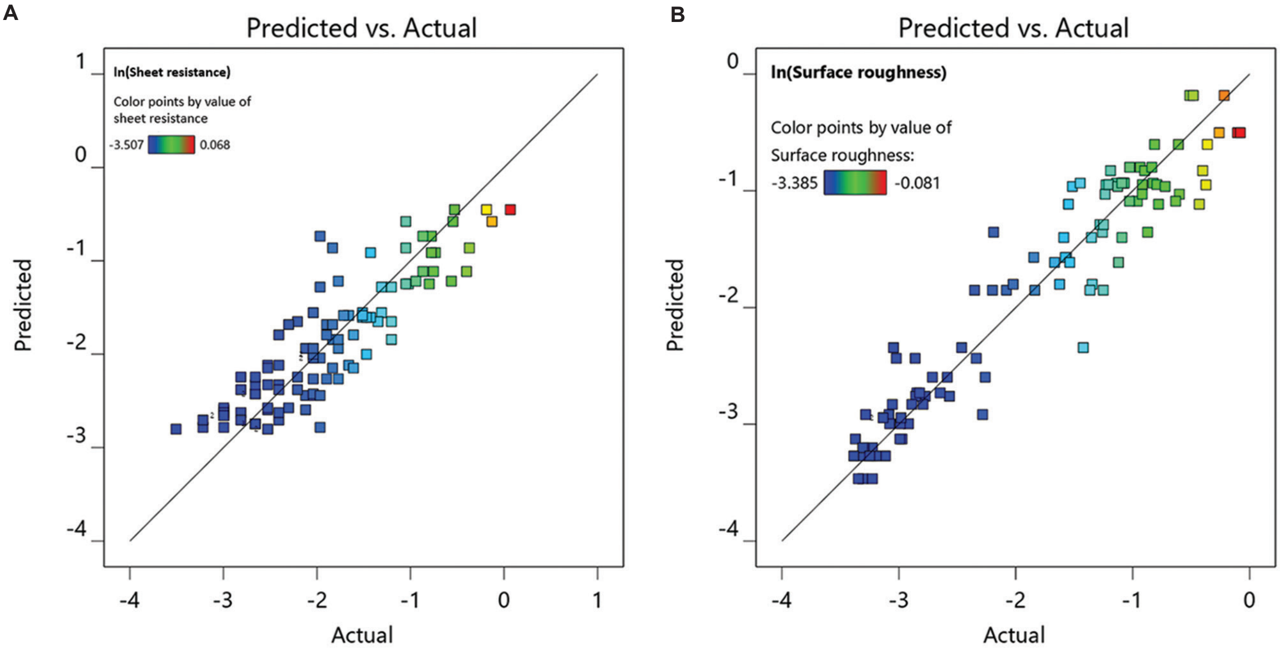

Figure 7. Predicted line values actual values for (A) sheet resistance and (B) surface roughness.

In addition, the minimum value and maximum value set for the sheet resistance and the surface roughness indicator are [3×10^{-2}, 1.07] Ω/sq and [0.034, 0.922], respectively. In this case, the optimal number of layer and sintering distance determined from the desirability function are 2 and 42.5 cm, respectively, and the overall desirability is 0.878 (Figure 10).

The desirability function approach can optimize the conflicting responses by merging the multi-objective vector into a single objective. As the attained optimal solution is very sensitive to the user specified weights used in the optimization process, there is a need to determine a set of Pareto-optimal points as alternate solutions in place of

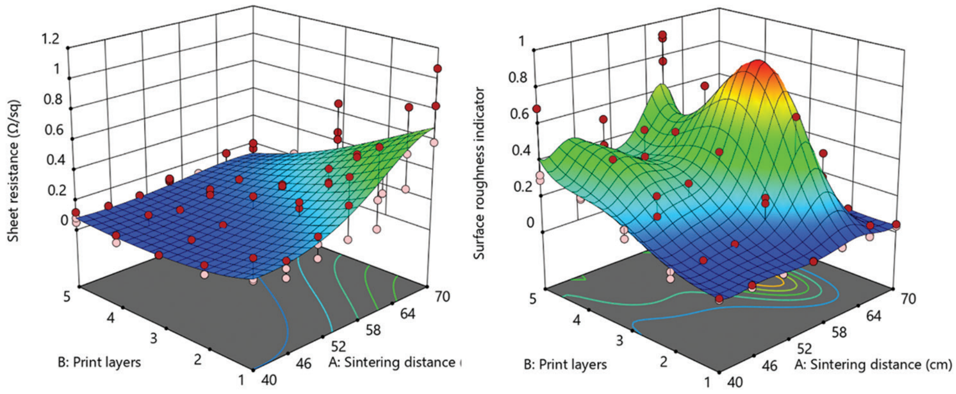

Figure 8. Response surface curves for (A) sheet resistance and (B) surface roughness with respect to the sintering distance and number of print layers.

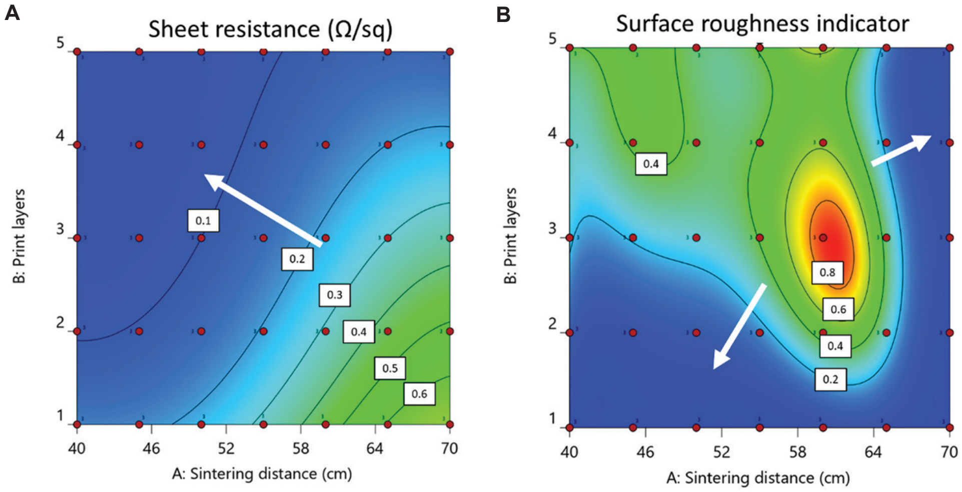

Figure 9. (A and B) Conflicting relationship between sheet resistance and surface roughness with respect to the number of print layers and the sintering distance in the sintering process. Arrow indicating the direction towards lower values.

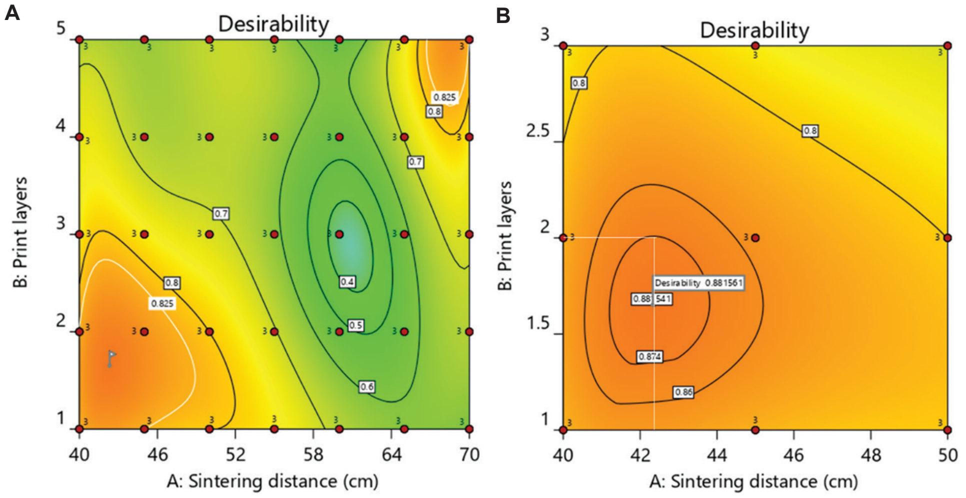

Figure 10. 2D map for the desirability function (A) over the entire studied process window and (B) zoomed in at the region with highest desirability. Red indicates high desirability and green indicates low desirability.

an individual point, particularly when prior knowledge about the underlying optimization problem is unknown. In this case, the derived statistical models were jointly driven with the NSGA-III to systematically optimize the conflicting responses in a more robust manner. Figure 11 demonstrates the flow chart of the adopted GA-based multi-objective optimization approach. During the optimization process, the input factors including sintering distance and number of print layers were characterized by the string of chromosome, and the proposed binary encoding of the chromosome pattern is shown in Figure 12, in which each process parameter looks like a gene that undergoes crossover and mutation in NSGA-III. Based on the experimental design and ANOVA results as discussed above, the attained statistical models were driven with the NSGA-III, and the two contradicting objectives (sheet resistance and surface roughness) were optimized in terms of minimization.

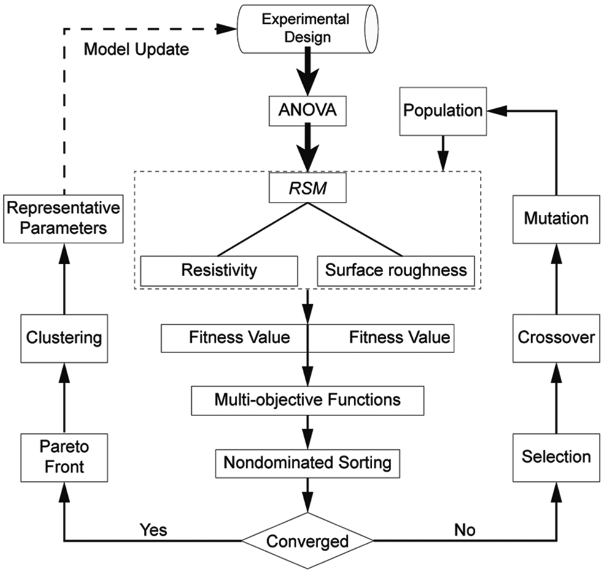

Figure 11. Flow chart of the adopted genetic algorithm-based multi-objective optimization approach.

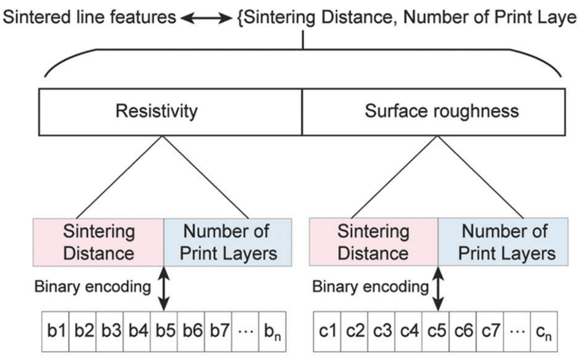

Figure 12. The chromosome encoding pattern in NSGA-III.

Table 4 summarizes the system settings of the adopted multi-objective optimization approach. Based on the proposed flow chart, the optimization process will be repeated if the employed NSGA-III does not reach its convergence. On the contrary, the convergent optimization algorithm will generate the corresponding Pareto front set as candidate solutions for the optimization process. However, as it will be inefficient to utilize the whole Pareto solution set during the evolution process, an affinity propagation approach is adopted to select the clustering centroids as representative solutions[49], which will be helpful to further enhance the efficiency of the optimization process.

Figure 13 demonstrates the optimization results with respect to the conflicting relationship between the surface roughness and sheet resistance. As shown in Figure 13A-C, to ensure the convergence of the optimization process, the generations were increased until the obtained Pareto front remains stable. Under such circumstances, the corresponding Pareto optimal set based on clustering is shown in Figure 13D. Generally, the clustering centroids of the attained Pareto optimal set as shown in Table 5 can be selected as the representative solutions of the optimization process[42], which will be helpful to extend the selection

Table 4. System settings of the adopted multi-objective optimization approach

Parameters	Settings
Number of input parameters	2
Number of statistical models	2
Objective functions	2
(1) Obj_1=sintering distance	Minimization
(2) Obj_2=number of print layers	Minimization
Constraints of adjustable parameters	2
(1) Sintering distance (cm)	[40, 70]
(2) Number of print layers	[1, 5]
Population size of NSGA-III	300
Crossover probability	0.9
Mutation probability	0.01
Maximal generations	2000

Table 5. Identified clustering centroids of the obtained Pareto optimal set

Solutions	Sintering distance (cm)	Number of print layers (→closest integer)	Sheet resistance (Ω/sq)	Surface roughness indicator
Solution 1	41.47	3.08 (→3)	6.31×10^{-2}	0.168891
Solution 2	42.27	1.91 (→2)	7.42×10^{-2}	0.09184
Solution 3	42.33	1.74 (→2)	9.30×10^{-2}	0.04964

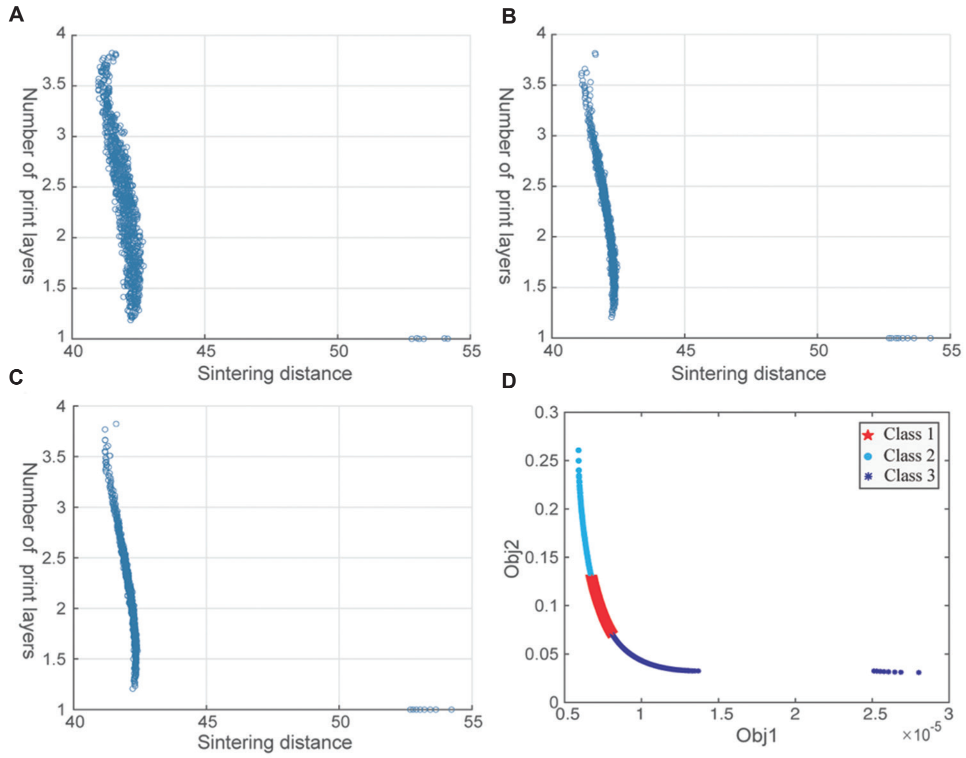

Figure 13. Optimization results with respect to sintered line features. (A-C) The variation of the obtained Pareto front under the generations of 500, 1000, and 2000, respectively. (D) The obtained Pareto optimal set corresponding to (C).

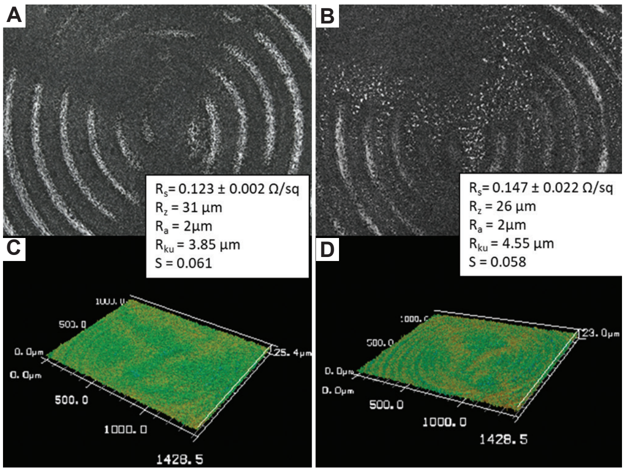

Figure 14. Optical images and confocal micrographs showing the surface morphologies of (A and C) Set 1 and (B and D) Set 2 as well as their corresponding surface roughness and sheet resistance.

for designers and optimize the printing quality in a more robust manner. However, as the number of print layers is limited to be an integer in this research, some approximate solutions such as (42.22, 2) and (41.50, 3) can be selected from the optimal Pareto front to replace the initial solutions, and more solutions from the selected cluster could be used to further extend the selection. Compared with the desirability function, the non-dominated sorting-based multi-objective optimization approach can provide different selections according to users' preference, which will be beneficial to trade-off the conflicting responses in a more objective manner.

To verify the solutions, we have identified two solution sets that are close to the obtained Pareto optimal sets, which are Set 1 (sintering distance: 41.5 cm; print layers: 3) and Set 2 (sintering distance: 42.5 cm; print layers: 2). Figure 14 shows the optical images and the sheet resistance of the sintered silver film. The results suggest that the proposed approach can effectively identify a set of Pareto-optimal points for designers. Furthermore, the circuit designer could select the preferred solution from a set of Pareto-optimal solutions rather than from a single point, and the selection could be further extended from the cluster that the chosen solution represents, the surface morphology, and electrical property of the sintered film could be optimized in more robust and systematic manners.

3. Conclusion

In this work, a conflicting relationship between the electrical property and physical property of the photonic sintered silver thin film prepared using aerosol jet printing technique is observed. As such, a hybrid multi-objective optimization approach is proposed to find the optimum solutions within the operating windows. In the proposed methodology, the response surface methodology is used to study the individual effects and their interactions of the main variables on the sheet resistance and the surface roughness of the printed silver film. The conflicting relationship between the sheet resistance and the surface roughness was ascertained by the RSMs. Then the 2D optimal operating windows were ascertained by a desirability function approach to reduce the inherent conflict of the print passes of the printed film and the sintering distance of the IPL sintering process. Thereafter, the derived RSMs and the corresponding statistical uncertainty were jointly driven with the NSGA-III to methodically optimize the overall printing quality in 2D space. The experimental results demonstrate that the suggested hybrid multi-objective optimization approach was advantageous to reduce the contradiction between the sheet resistance and the surface roughness, yielding printed films with low surface roughness and low sheet resistance.

Comparing to the conventional trial-and-error method, the suggested optimization methodology is found to be more efficient and systematic. It should be pointed out, however, that the optimal windows will vary significantly depending on the types of ink and substrate properties. Nevertheless, this work outlined a systematic approach for determining the optimal windows for the IPL sintering process of the aerosol jet printed films that can also be applied when other types of ink or substrate are used. For potential research work, the influence of the number of pulse and pulse duration can be systematically studied for aerosol jet printed silver film. Furthermore, this work outlines effective approaches for optimizing the electrical property and the surface morphology of the nanoparticle-based film which can potentially allow for the homogeneous deposition of material for the subsequent layers of multi-layered and multi-material electronics such as an electrochemical electrode with a dielectric passivation layer.

Acknowledgments

None.

Funding

This research is supported by the National Research Foundation, Prime Minister's Office, Singapore under its Medium-Sized Centre funding scheme and PUB, Singapore's National Water Agency under its Urban Solutions & Sustainability (Competitive Research Programme [Water] Scheme, PUB-1804-0075), and the Key Natural Science Project of Anhui Provincial Education Department (No. KJ2021A1111).

Conflict of interest

The authors declare no conflict of interest.

Author contributions

Conceptualization: Guo Liang Goh
Data curation: Guo Dong Goh
Funding acquisition: Wai Yee Yeong
Investigation: Guo Dong Goh
Methodology: Guo Liang Goh, Haining Zhang
Software: Haining Zhang
Supervision: Wai Yee Yeong, Tzyy Haur Chong
Writing – original draft: Guo Liang Goh, Guo Dong Goh
Writing – review & editing: Tzyy Haur Chong

References

1. Tan H, Tran T, Chua C, 2016, A review of printed passive electronic components through fully additive manufacturing methods. *Virtual Phys Prototyp*, 11: 271–288.

   https://doi.org/10.1080/17452759.2016.1217586

2. Saengchairat N, Tran T, Chua CK, 2017, A review: Additive manufacturing for active electronic components. *Virtual Phys Prototyp*, 12: 31–46.

   https://doi.org/10.1080/17452759.2016.1253181

3. Fisher G, Seacrist MR, Standley RW, 2012, Silicon crystal growth and wafer technologies. *Proc IEEE*, 100: 1454–1474.

   https://doi.org/10.1109/jproc.2012.2189786

4. Tan HW, An J, Chua CK, *et al.*, 2019, Metallic nanoparticle inks for 3D printing of electronics. *Adv Electron Mater*, 5: 1800831.

   https://doi.org/10.1002/aelm.201800831

5. Saidina D, Eawwiboonthanakit N, Mariatti M, *et al.*, 2019, Recent development of graphene-based ink and other conductive material-based inks for flexible electronics. *J Electron Mater*, 48: 3428–3450.

   https://doi.org/10.1007/s11664-019-07183-w

6. Yang W, List-Kratochvil EJ, Wang C, 2019, Metal particle-free inks for printed flexible electronics. *J Mater Chem C*, 7: 15098–15117.

   https://doi.org/10.1039/c9tc05463d

7. Bhat KS, Ahmad R, Wang Y, *et al.*, 2016, Low-temperature sintering of highly conductive silver ink for flexible electronics. *J Mater Chem C*, 4: 8522–8527.

   https://doi.org/10.1039/c6tc02751b

8. Xu Z, Dong Q, Qtieno B, *et al.*, 2016, Real-time *in situ* sensing of multiple water quality related parameters using micro-electrode array (MEA) fabricated by inkjet-printing technology (IPT). *Sens Actuators B Chem*, 237: 1108–1119.

   https://doi.org/10.1016/j.snb.2016.09.040

9. Zhang H, Moon SK, Ngo TH, 2020, 3D printed electronics of non-contact ink writing techniques: status and promise. *Int J Precis Eng Manuf Green Technol*, 7: 511–524.

   https://doi.org/10.1007/s40684-019-00139-9

10. Goh GL, Zhang H, Chong TH, *et al*., 2021, 3D printing of multilayered and multimaterial electronics: A review. *Adv Electron Mater*, 7: 2100445.

    https://doi.org/10.1002/aelm.202100445

11. Goh GL, Ma J, Chua KL, *et al*., 2016, Inkjet-printed patch antenna emitter for wireless communication application. *Virtual Phys Prototyp*, 11: 289–294.

    https://doi.org/10.1080/17452759.2016.1229802

12. Goh GL, Shweta A, Yeong WY, 2018, High resolution aerosol jet printing of conductive ink for stretchable electronics. In: Proceedings of the 3rd International Conference on Progress in Additive Manufacturing (PRO-AM). Nanyang Technological University, Singapore, p109–114.

13. Agarwala S, Goh GL, Yeong WY, 2018, Aerosol jet printed pH sensor based on carbon nanotubes for flexible electronics. In: Proceedings of the 3rd International Conference on Progress in Additive Manufacturing (Pro-AM 2018), Singapore.

14. Goh GL, Agarwala S, Yeong WY, 2018, High resolution aerosol jet printing of conductive ink for stretchable electronics. In: Proceedings of the 3rd International Conference on Progress in Additive Manufacturing (Pro-AM 2018), Singapore.

15. Goh GL, Dikshit V, Koneru R, *et al*., 2022, Fabrication of design-optimized multifunctional safety cage with conformal circuits for drone using hybrid 3D printing technology. *Int J Adv Manuf Technol*, 120: 2573–2586.

    https://doi.org/10.1007/s00170-022-08831-y

16. Jiang P, Ji Z, Zhang X, *et al*., 2018, Recent advances in direct ink writing of electronic components and functional devices. *Prog Addit Manuf*, 3: 65–86.

    https://doi.org/10.1007/s40964-017-0035-x

17. Wilkinson N, Smith M, Kay R, *et al*., 2019, A review of aerosol jet printing a non-traditional hybrid process for micro-manufacturing. *Int J Adv Manuf Technol*, 105: 4599–4619.

    https://doi.org/10.1007/s00170-019-03438-2

18. Zeng M, Kuang W, Khan I, *et al*., 2020, Colloidal nanosurfactants for 3D conformal printing of 2D van der waals materials. *Adv Mater*, 32: 2003081.

    https://doi.org/10.1002/adma.202003081

19. Aleeva Y, Pignataro B, 2014, Recent advances in upscalable wet methods and ink formulations for printed electronics. *J Mater Chem C*, 2: 6436–6453.

    https://doi.org/10.1039/c4tc00618f

20. Hoeng F, Denneulin A, Bras J, 2016, Use of nanocellulose in printed electronics: A review. *Nanoscale*, 8: 13131–13154.

    https://doi.org/10.1039/c6nr03054h

21. Goh GL, Tay MF, Lee JM, *et al*., 2021, Potential of printed electrodes for electrochemical impedance spectroscopy (EIS): Toward membrane fouling detection. *Adv Electron Mater*, 7: 2100043.

    https://doi.org/10.1002/aelm.202100043

22. Jiang J, Bao B, Li M, *et al*., 2016, Fabrication of transparent multilayer circuits by inkjet printing. *Adv Mater*, 28: 1420–1426.

    https://doi.org/10.1002/adma.201503682

23. Agarwala S, Goh GL, Le TS, *et al*., 2018, Wearable bandage-based strain sensor for home healthcare: Combining 3D aerosol jet printing and laser sintering. *ACS Sensors*, 4: 218–226.

    https://doi.org/10.1021/acssensors.8b01293

24. Pan H, Ko SH, Grigoropoulos CP, 2008, Thermal sintering of solution-deposited nanoparticle silver ink films characterized by spectroscopic ellipsometry. *Appl Phys Lett*, 93: 234104.

    https://doi.org/10.1063/1.3043583

25. Allen ML, Aronniemi M, Mattila T, *et al*., 2008, Electrical sintering of nanoparticle structures. *Nanotechnology*, 19: 175201.

    https://doi.org/10.1088/0957-4484/19/17/175201

26. Tan HW, Saengchairat N, Goh GL, *et al*., 2020, Induction sintering of silver nanoparticle inks on polyimide substrates. *Adv Mater Technol*, 5: 1900897.

    https://doi.org/10.1002/admt.201900897

27. Nam HJ, Kang SY, Park JY, *et al*., 2019, Intense pulse light sintering of an Ag microparticle-based, highly stretchable, and conductive electrode. *Microelectron Eng*, 215: 111012.

    https://doi.org/10.1016/j.mee.2019.111012

28. Jang YR, Joo SJ, Chu JH, *et al*., 2020, A review on intense pulsed light sintering technologies for conductive electrodes in printed electronics. *Int J Precis Eng Manuf Green Technol*, 8: 327–363.

    https://doi.org/10.1007/s40684-020-00193-8

29. Moores A, Goettmann F, 2006, The plasmon band in noble metal nanoparticles: an introduction to theory and applications, *New J Chem*, 30: 1121–1132.

    https://doi.org/10.1039/b604038c

30. Kelly KL, Coronado E, Zhao LL, *et al*., 2003, The optical properties of metal nanoparticles: The influence of size, shape, and dielectric environment. *J Phys Chem B*, 107: 668–677.

    https://doi.org/10.1021/jp026731y

31. Zhang JZ, Noguez C, 2008, Plasmonic optical properties and applications of metal nanostructures. *Plasmonics*, 3: 127–150.

    https://doi.org/10.1007/s11468-008-9066-y

32. Lee DJ, Park SH, Jang S, *et al*., 2011, Pulsed light sintering characteristics of inkjet-printed nanosilver films on a polymer substrate. *J Micromech Microeng*, 21: 125023.

    https://doi.org/10.1088/0960-1317/21/12/125023

33. Moon CJ, Kim I, Joo SJ, *et al*., 2017, Flash light sintering of ag mesh films for printed transparent conducting electrode. *Thin Solid Films*, 629: 60–68.

    https://doi.org/10.1016/j.tsf.2017.03.049

34. Kang J, Ryu J, Kim H, *et al*., 2011, Sintering of inkjet-printed silver nanoparticles at room temperature using intense pulsed light. *J Electron Mater*, 40: 2268–2277.

    https://doi.org/10.1007/s11664-011-1711-0

35. Niittynen J, Abbel R, Mäntysalo M, *et al*., 2014, Alternative sintering methods compared to conventional thermal sintering for inkjet printed silver nanoparticle ink. *Thin Solid Films*, 556: 452–459.

    https://doi.org/10.1016/j.tsf.2014.02.001

36. Hösel M, Krebs FC, 2012, Large-scale roll-to-roll photonic sintering of flexo printed silver nanoparticle electrodes. *J Mater Chem*, 22: 15683–15688.

    https://doi.org/10.1039/c2jm32977h

37. Chung WH, Hwang HJ, Lee SH, *et al*., 2012, *In situ* monitoring of a flash light sintering process using silver nano-ink for producing flexible electronics. *Nanotechnology*, 24: 035202.

    https://doi.org/10.1088/0957-4484/24/3/035202

38. Yung KC, Gu X, Lee C, *et al*., 2010, Ink-jet printing and camera flash sintering of silver tracks on different substrates, *J Mater Process Technol*, 210: 2268–2272.

    https://doi.org/10.1016/j.jmatprotec.2010.08.014

39. Tobjörk D, Aarnio H, Pulkkinen P, *et al*., 2012, IR-sintering of ink-jet printed metal-nanoparticles on paper. *Thin Solid Films*, 520: 2949–2955.

    https://doi.org/10.1016/j.jmatprotec.2010.08.014

40. Goh GL, Agarwala S, Yeong WY, 2019, Aerosol-jet-printed preferentially aligned carbon nanotube twin-lines for printed electronics, *ACS Appl Mater Interfaces*, 11: 43719–43730.

    https://doi.org/10.1021/acsami.9b15060

41. Keyence. Surface Roughness Parameters. Keyence. Available from: https://www.keyence.com/ss/products/microscope/roughness/line/parameters.jsp [Last accessed on 2021 Dec 20].

42. Zhang H, Choi JP, Moon SK, *et al*., 2020, A hybrid multi-objective optimization of aerosol jet printing process via response surface methodology., *Addit Manuf*, 33: 101096.

    https://doi.org/10.1016/j.addma.2020.101096

43. Srinivas M, Patnaik LM, 1994, Genetic algorithms: A survey. *Computer*, 27: 17–26.

44. Chen JH, Ho SY, 2005, A novel approach to production planning of flexible manufacturing systems using an efficient multi-objective genetic algorithm. *Int J Mach Tools Manuf*, 45: 949–957.

    https://doi.org/10.1016/j.ijmachtools.2004.10.010

45. Saravanan R, Asokan P, Sachidanandam M, 2002, A multi-objective genetic algorithm (GA) approach for optimization of surface grinding operations. *Int J Mach Tools Manuf*, 42: 1327–1334.

    https://doi.org/10.1016/s0890-6955(02)00074-3

46. Jain NK, Jain V, Deb K, 2007, Optimization of process parameters of mechanical type advanced machining processes using genetic algorithms. *Int J Mach Tools Manuf*, 47: 900–919.

    https://doi.org/10.1016/j.ijmachtools.2006.08.001

47. Deb K, Pratap A, Agarwal S, *et al*., 2002, A fast and elitist multiobjective genetic algorithm: NSGA-II. *IEEE Trans Evol Comput*, 6: 182–197.

    https://doi.org/10.1109/4235.996017

48. Srinivas N, Deb K, 1994, Muiltiobjective optimization using nondominated sorting in genetic algorithms. *Evol Comput*, 2: 221–248.

    https://doi.org/10.1162/evco.1994.2.3.221

49. Frey BJ, Dueck D, 2007, Clustering by passing messages between data points. *Science*, 315: 972–976.

    https://doi.org/10.1126/science.1136800

WHIOCE
PUBLISHING PTE. LTD.
Materials Science in Additive Manufacturing

ORIGINAL RESEARCH ARTICLE

Process study for directed energy deposition of 316L stainless steel with TiB_2 metal matrix composites

Yao Ting Ang[1], **Swee Leong Sing**[2]*, **Joel Choon Wee Lim**[1]

[1]School of Mechanical and Aerospace Engineering, Nanyang Technological University, Singapore

[2]Department of Mechanical Engineering, National University of Singapore, Singapore

Abstract

In addition to laser powder bed fusion, directed energy deposition (DED) is also gaining interest as an effective metal additive manufacturing technique. Due to its system configuration, it is more efficient and flexible for materials development. Therefore, it can be used for processing of metal matrix composites (MMCs) through the use of powder mixture as feedstock. 316L stainless steel has high corrosion resistance, biocompatibility, and ductility. Several studies have shown the feasibility of using DED to process 316L stainless steel. The material properties of 316L stainless steel can be improved using reinforcement particles such as TiB_2 to form MMCs. In this study, the effects of process parameters on microstructure and mechanical properties of 316L stainless steel reinforced with TiB_2 (316L/TiB_2) MMC were studied. The process parameters, including laser power, scanning speed, and hopper speed, were varied and analyzed using Taguchi L9 array. It was found that the process parameters have insignificant effect on the bulk density of the samples produced. Through this study, it is also found that tumble mixing was not suitable for the powder feedstock preparation for MMCs to be processed by DED. The microstructure of DED 316L/TiB_2 MMC samples consists of columnar and equiaxed grains. Columnar grains were located within the layers while equiaxed grains were located at the interlayer zones. Fine sub-grains were also observed within these grains and their boundaries were enriched with molybdenum and chromium segregations. Precipitates containing titanium were also observed to segregate at the sub-grain boundaries. Finally, the Vickers microhardness of the DED 316L/TiB_2 MMC was found to be similar to pure 316L stainless steel produced by DED.

Keywords: Additive manufacturing; 3D printing; Directed energy deposition; Metal matrix composites; Steels

***Corresponding author:**
Swee Leong Sing
(sweeleong.sing@nus.edu.sg)

Citation: Ang YT, Sing SL, Lim JCW, 2022, Process study for directed energy deposition of 316L stainless steel with TiB_2 metal matrix composites. *Mater Sci Add Manuf*. 1(2): 13. https://doi.org/10.18063/msam.v1i2.13

Received: April 29, 2022

Accepted: June 10, 2022

Published Online: June 29, 2022

1. Introduction

Additive manufacturing (AM) is a disruptive technology that has gain increasing traction in recent years. AM is a family of techniques and processes that involve the addition of material layer-by-layer with the help of computer-aided designs and computer-aided manufacturing[1]. Compared to traditional manufacturing that produces parts by removing material, AM is more flexible and efficient that can reduce manufacturing costs and environmental impacts[2]. AM is also able to create near net shape parts with complex geometries that would otherwise be difficult to manufacture[3,4].

Directed energy deposition (DED) is a popular AM technique for metals that uses a laser beam to melt metal powders onto a substrate. There are various names used for DED, including laser metal deposition, laser cladding, and laser engineered net shaping. One of the key features of DED is its relatively low energy input, resulting in lower residual stresses and smaller heat-affected zones[5]. Due to its configuration, DED is ideal for repair and reinforcement cladding applications[6-8]. Furthermore, DED is able to create metal matrix composites (MMC) and functionally graded materials that can be customized to meet specific requirements[9,10].

316L stainless steel is one of the most suitable materials for DED. It is a low carbon austenitic steel alloy that has excellent corrosion resistance, ductility, and biocompatibility[11]. It is suitable for marine, biomedical, chemical, and even nuclear industry[12,13]. However, 316L stainless steel still have relatively low strength, hardness, and wear resistance compared to other alloys such as Ti6Al4V which limits its applications. These shortcomings can be overcome by adding reinforcement particles such as SiC, TiC, and TiB_2 to form MMCs that have significantly higher strength and hardness[12,14-17]. Among the various reinforcement particles, TiB_2 is considered one of the most suitable due to its compatibility with 316L stainless steel[18]. TiB_2 has high thermal stability, chemical resistance, and wettability with molten steel[19].

One of the main challenges of the DED process is the optimization of the variables involved. The part properties from DED process is highly dependent on these variables such as scanning paths and build part geometry as well as process parameters[20]. Variation in these variables will cause a significant change in microstructure and mechanical properties of DED parts. Mukherjee *et al.* observed changes in the thermal distortion of AM parts with process parameters, build geometry, and material[21]. Saboori *et al.* also demonstrated that the microstructure and tensile strength of 316L stainless steel cuboids created by DED varied depending on the deposition strategy due to the differences in cooling rate[22].

There have been some studies on the effects of variables on MMCs using 316L stainless steel as the matrix. Ertugrul *et al.* showed that using proper powder preparation, the addition of TiC particles increased the hardness by about 100 HV as compared to pure 316L stainless steel[14]. Wu *et al.* showed that increasing the SiC content in 316L stainless steel MMCs would result in higher hardness but lower corrosion resistance[12]. Other researchers such as AlMangour *et al.* were able to find that for laser powder bed fusion (L-PBF), which is another type of metal AM technique, 316L with 10 vol.% TiB_2 was optimum to produce finer microstructure and better mechanical properties[18]. They attributed the improvement in mechanical properties to Orowan and grain boundary strengthening. However, there is currently no known research on the process parameter optimization of 316L stainless steel reinforced with TiB_2 particles for DED. Optimizations of these process parameters are crucial to produce parts with desired mechanical properties with minimal defects, thus, increasing the flexibility and usage of DED for a wider range of applications.

In this study, an optimal set of process parameters for 316L stainless steel with TiB_2 MMC (316L/TiB_2) was determined. The effects of process parameters on the mechanical properties and microstructure of 316L/TiB_2 were evaluated. The Taguchi L9 array was used to design the experiments and to optimize the process parameters for optimum mechanical properties. The three process parameters varied were laser power, scanning speed, and hopper speed at three different levels. Pre-mixed 316L stainless steel with 6 wt.% TiB_2 powder was used and other parameters such as laser spot size and scanning strategy were kept constant. Optical microscopy and scanning electron microscopy (SEM) were used to evaluate the microstructure of the samples. Finally, the density and Vickers hardness of the samples were also determined and discussed.

2. Materials and methods

2.1. Powder preparation

Gas atomized 316L stainless steel powder with particle size distribution 40–100 μm from TLS Technik (Germany) was tumble mixed with 6 wt.% TiB_2 nanoparticles. The powder mixture was mixed for 8 h at 60 rpm using the Inversina 2L Tumbler Mixer (Bioengineering AG, Switzerland). The chemical composition of the 316L stainless steel powder is listed in Table 1.

The powders before and after mixing were examined using SEM to ensure that the TiB_2 particles adhere to the 316L stainless steel particles and are homogeneously dispersed. TiB_2 particles were observed to be evenly coated and distributed on the 316L stainless steel particles. The

Table 1. Chemical composition of 316L stainless steel powder

Material	Chemical composition (wt.%)								
316L	C 0.03	Mn 2	P 0.045	S 0.03	Si 1	Cr 16-18	Ni 10-14	Mo 2-3	Fe Bal.

SEM images of the 316L stainless steel and TiB_2 powder before and after mixing are shown in Figure 1.

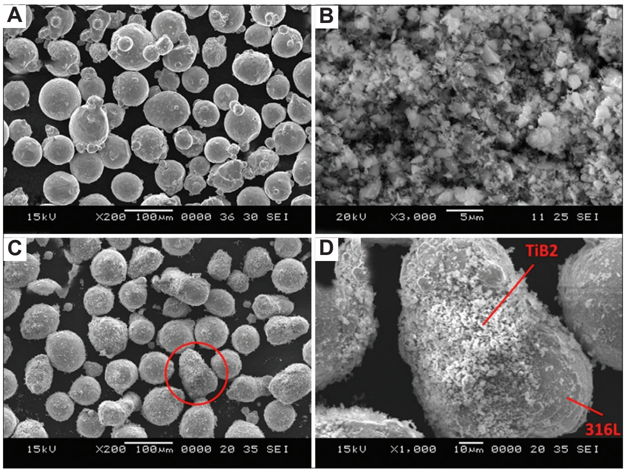

Figure 1. Scanning electron microscopy images: (A) pure 316L stainless steel powder, (B) TiB_2 nanoparticles, (C) mixed 316L/TiB_2 powder mixture, and (D) higher magnification showing TiB_2 particles adhering to surface of a 316L stainless steel particle.

2.2. DED

The fabrications were conducted using a DMG Mori LASERTEC 65 3D (Germany). The laser unit consists of a 2.5 kW diode-pumped laser that has 3 mm laser spot size and produce wavelengths ranging from 900 nm to 1080 nm. The powder focus distance used is 11 mm and the argon gas flow rate for shielding was 6 l/min. The fixed parameters used for the fabrication are shown in Table 2.

Table 2. Fixed process parameters for DED

Fixed process parameters	Values
Spot size	3 mm
Powder focus	11 mm
Shield gas	Argon
Gas flow rate	6 l/min
Overlap rate	50%
Layer step height	1 mm
Scanning pattern	Zig-zag

To optimize the process parameters, a L9 Taguchi array was used that varied laser power, scanning speed, and hopper speed at three levels. The Taguchi L9 array and the parameters used are tabulated in Table 3. The energy density, ε, is calculated using the following equation:

$$\varepsilon = \frac{P}{v \times d}$$

where P is the laser power (W), v is the scanning speed (mm/min), and d is the laser spot size (mm).

The range of each parameter was obtained by preliminary experiments that vary the parameters for single clad. For example, at 600 W laser power, very little material was deposited while at 1800 W laser power, overheating was observed. The parameter ranges were also chosen such that the energy density for all the Taguchi runs is between the known optimal DED process parameters for pure 316L stainless steel and its composites. Due to formation of powder clouds during the DED process, which is attributed to the presence of TiB2 particles, the powder flow rate could not be accurately measured; hence, hopper speed was varied instead.

For each set of Taguchi parameters, three 20 mm × 20 mm × 10 mm cuboids were fabricated on 304 stainless steel substrates. Each of the three cuboids was built concurrently, layer-by-layer, in a zig-zag path as shown in Figure 2.

The DED produced cuboids were then separated from the substrate using wire electrical discharge machining. The samples were cut 1 mm above the substrate such that the samples analyzed are not contaminated with the substrate material due to dilution effect.

The results obtained from the experiments were converted into a signal-to-noise (S/N) ratio. The S/N ratio converts the results into a logarithmic scale to account for non-linear relationships. It is also robust as it considers both the mean and variance of the results. The "larger is better" S/N ratio approach was used and the formula for S/N ratio is given by:

$$S/N = -10\,log_{10} \frac{\sum_{i=i}^{n} \frac{1}{y_i^{2}}}{n} \qquad (1)$$

Where y_i is the raw measurement value and n is the number of measurements for each Taguchi parameter.

2.3. Microstructure analysis

The DED samples were ground using 320 grit sandpaper, followed by polishing using 9 µm, 3 µm, 1 µm diamond suspension, and 0.25 µm standard fumed silica suspension (OP-S). Samples were rinsed with water after each step.

The polished samples were first observed using an Olympus SZX7 (Japan) optical microscope to check for pores and cracks. The samples were then etched by swabbing the surfaces with Marble's Reagent for 10 s. The microstructure was then observed using JEOL 5600LV (United States) SEM. Energy dispersive X-ray spectroscopy (EDS) was also used to identify the compositions of the microstructures found using the same equipment as the SEM.

Table 3. L9 Taguchi array with estimated powder flow rate and energy density

Taguchi Number	Run Order	Laser power (W)	Scanning speed (mm/min)	Hopper speed (rpm)	Estimated powder rate (g/min)	Energy density (J/mm^2)
1	1	1000	200	200	5.44	100.0
2	2	1000	400	300	7.85	50.0
3	3	1000	600	400	9.95	33.3
4	8	1200	200	300	7.85	120.0
5	9	1200	400	400	9.95	60.0
6	7	1200	600	200	5.44	40.0
7	6	1400	200	400	9.95	140.0
8	4	1400	400	200	5.44	70.0
9	5	1400	600	300	7.85	46.7

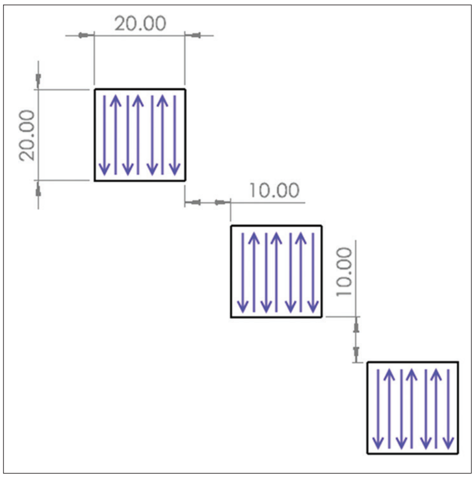

Figure 2. Scanning path used in directed energy deposition.

2.4. Density measurements

The method of hydrostatic weighing was used to measure the bulk density of the polished samples based on Archimedes' Principle. The XS204 balance machine with density kit (Mettler Toledo, Switzerland) was used to perform the density tests.

The actual TiB_2 content of the DED samples was calculated using the rule of mixture:

$$f = \frac{\frac{1}{\rho} - \frac{1}{\rho_S}}{\frac{1}{\rho_T} - \frac{1}{\rho_S}} \tag{2}$$

Where f is the weight fraction of TiB_2, P_s and P_T are the density of 316L stainless steel (8.00 g/cm^3) and TiB_2 (4.52 g/cm^3), respectively. The calculated TiB_2 weight fraction assumes that the DED samples have no porosity.

2.5. Microhardness

The Vickers hardness of the polished samples was measured using FM-300e hardness tester (Micro Measurement Pte Ltd, Singapore) at a load of 300 g for 15 s, according to ISO 6507-1:2018. Six evenly spaced indentations were made on both the top and side surfaces.

3. Results and discussion

3.1. Microstructure

The optical micrographs of the polished side and top surfaces with clear boundaries between the melt pools are shown in Figure 3.

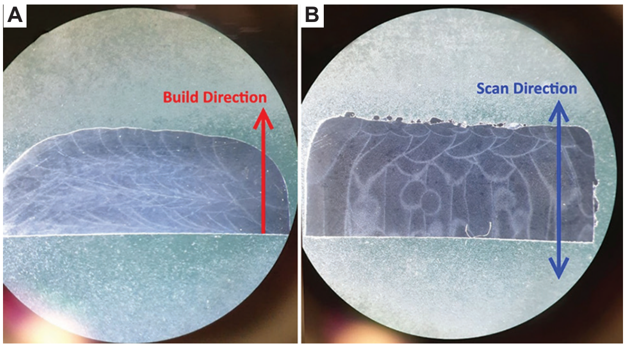

Figure 3. Optical micrographs: (A) side surface and (B) top surface with melt pool boundaries.

The melt pool boundaries were formed during the remelting of layers and adjacent scan tracks when subsequent powder is deposited following the scanning path. As seen in Figure 3B, the scan tracks formed straight lines following the scanning path but stops abruptly near the edge of the sample. This is due to the laser momentarily turning off and on as it shifts to the adjacent linear path, remelting and forming a separate melt pool during the DED process. No crack or visible pore can be observed in all the DED samples. The optical micrographs using higher magnifications are shown in Figure 4.

Precipitates between 1 µm and 2 µm were identified to be TiB_2 within the 316L stainless steel matrix, which can be a result of agglomeration of the particles. Further magnifications also revealed finer precipitates that were smaller than 1 µm. These nanoinclusions are not pores and were identified by Saeidi *et al.* to be silicate-chromium phases[23]. Due to the low wettability of silicon with steel, it tends to separate from the melt pools during the DED process. It is also circular to reduce surface tension due to the high viscosity of the silicate melt. These nanoinclusions could also be TiB_2 due to their similarity in size. The SEM images of the polished and etched top and side surfaces reveal the microstructure of DED 316L/TiB_2 MMC as shown in Figure 5.

The microstructure mainly consists of epitaxial columnar grains that grow along the build direction. This is because the previously deposited layers act as a heat sink and affect the direction of heat flow, resulting in a vertical temperature that encouraged columnar grains to grow[24]. At the interlayer zone, the microstructure morphology is made of fine equiaxed grains that were formed during remelting when a subsequent layer is deposited on top of it. The high cooling rates during the deposition of subsequent layers result in equiaxed grain growth. It is well documented that the difference solidification microstructure formed is due to the thermal gradients and cooling rate[23-25].

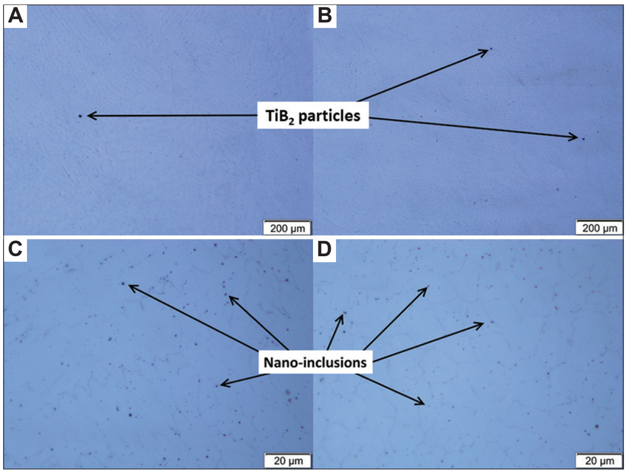

Figure 4. Optical micrographs of unetched samples at ×5 magnification for (A) side surface and (B) top surface and at ×50 magnification for (C) side surface and (D) top surface.

Within each of the columnar and equiaxed grains, there exist complex and intricate sub-grains. These sub-grains are not actual grains but were formed due to the segregation of the alloying molybdenum during the rapid solidification process[23]. There is insufficient time for the heavier molybdenum to dissolve into the matrix during solidification, leading to the enrichment of molybdenum at the sub-grain boundaries. The sub-grain boundaries are more chemically resistant than the matrix as revealed during the etching process. They also have high dislocation concentrations and help to strengthen the DED samples. Tan *et al.* were able to relate the Vickers hardness of DED 316L stainless steel to the sizes of these sub-grains using the Hall-Petch relationship[24]. The molybdenum enrichment at the sub-grain boundaries is confirmed using EDS for both equiaxed and columnar grains, as shown in Table 4. The locations for EDS are shown in Figure 6.

There is an enrichment of molybdenum and chromium with depletion of iron in the sub-grain boundaries compared to the matrix for both equiaxed and columnar grains. This agrees with the results obtained for pure 316L stainless steel[24]. EDS analysis of some of the larger precipitates showed presence of titanium, which confirmed that TiB_2 was successfully deposited during the DED process. Element mapping for titanium (Figure 7) shows high concentration of titanium that coincided with the location of precipitates. These precipitates are located the sub-grain boundaries and suggest that the actual TiB_2

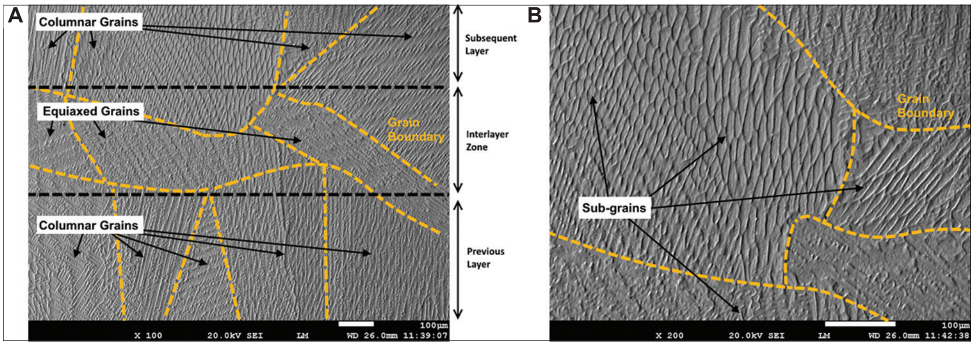

Figure 5. Scanning electron microscopy image of side surface (A) showing columnar and equiaxed grains and (B) higher magnification showing the sub-grains in the columnar and equiaxed grains.

content in the MMC samples may be significantly lower than 2 wt.%. This may account for the negligible differences in the results obtained for 316L/TiB_2 MMC as compared to pure 316L stainless steel.

3.2. Density

The mean and S/N ratio of the measured density is tabulated in Table 5, with the calculated weight fraction of TiB_2 in the DED samples. The average weight fraction of TiB_2 is 2 wt.% which is significantly lower than the added weight fraction of 6 wt.%. This indicates that the powder clouds formed during the DED process can be the TiB_2 particles that escaped during the powder deposition.

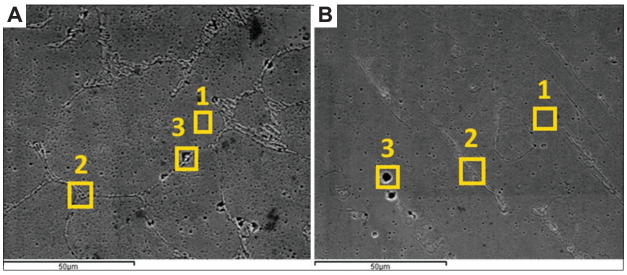

Figure 6. Energy dispersive X-ray spectroscopy locations for (A) equiaxed and (B) columnar grains. Location 1 is within the matrix, location 2 is at the sub-grain boundary, and location 3 is at the TiB_2 particle.

Table 4. Composition for equiaxed and columnar grains

Element	Equiaxed (wt.%)			Columnar (wt.%)		
	Matrix	Boundary	TiB_2	Matrix	Boundary	TiB_2
S	1.06	-	1.6	0.48	-	-
Cr	16.48	22.27	19.18	16.26	21.86	22.75
Mn	1.38	1.83	-	1.33	1.8	2.6
Fe	67.69	54.09	66.34	69.81	62.03	46.25
Ni	10.13	6.38	9.03	10.66	9.3	3.86
Ti	-	-	3.85	-	-	5.57
Mo	-	10.69	-	-	5.01	4.4
Others	3.26	4.74	-	1.46	-	14.57
Total	100	100	100	100	100	100

Even though TiB_2 particles were observed to be adhering onto the 316L stainless steel particle surfaces, the tumble mixing process did not induce sufficient adhesion which caused the TiB_2 particles to separate from the 316L stainless steel particles during powder deposition. The powder deposition step involves forces induced by the gas flow to expulse the powder from the nozzle. Tumble mixing is not suitable for mixing nanoparticle composites for DED as the process involves injecting the mixed powder into a fast-moving gas stream. Larger TiB_2 particles can also be used as they are less likely to escape due to higher gravitational force acting on them. Ball milling can be used to strengthen the adhesion during the mixing[18]. During ball milling, mechanical alloying is achieved due to the repeated deformation, fracturing, and cold welding of the powder particles[18,26]. At the start, the reinforcement particles facture due to their brittleness before sticking onto the matrix powder in which cold welding predominates due to plastic deformation. During the deformation and cold welding of the matrix powder particles, the reinforcement particles then dispersed inside the matrix. Fracture then takes over due to the matrix hardening. Finally, a dynamic balance between cold welding and fracture ensures the absence of agglomeration[27]. In addition, the collisions can cause the break-up of agglomerated particles[18]. However, it is of interest to note that using larger particles or ball milling result in a morphological change to the powder, which, in turn, may affect the powder flowability. Hence, a careful control of the powder preparation parameters is needed. With controlled parameters used during the process, the centrifugal effect of ball milling results in uniform dispersion of the reinforcement particles in the powder mixture with minimum change in powder morphology. It has been found that mechanical alloying

Table 5. Mean, S/N ratio of sample density, and calculated weight fraction of TiB_2

Taguchi number	Laser power (W)	Scanning speed (mm/min)	Hopper speed (rpm)	Mean density (g/cm³)	S/N	*f*
1	1000	200	200	7.891±0.004	17.943	1.8%
2	1000	400	300	7.879±0.011	17.929	2.0%
3	1000	600	400	7.874±0.016	17.924	2.1%
4	1200	200	300	7.887±0.002	17.938	1.9%
5	1200	400	400	7.876±0.002	17.926	2.0%
6	1200	600	200	7.855±0.012	17.903	2.4%
7	1400	200	400	7.876±0.003	17.927	2.0%
8	1400	400	200	7.883±0.006	17.934	1.9%
9	1400	600	300	7.862±0.008	17.910	2.3%

improves the distribution of Si_3N_4 and AlN in Al6061 aluminum powder. While the process also decreases the reinforcement particle size, it improved the composite characteristics by eliminating the reinforcement particle defects. Furthermore, the mechanical alloying also improved the matrix characteristics due to deformation and dislocations[28]. During mechanical alloying, it is possible for the morphology of powders to change from spherical to flattened and finally to nearly spherical again[29]. It was also observed that while the particle size of the mixed powder decreases with increase in milling time, there is a limit after which, the particle size will remain stable due to equilibrium between the cold welding and repeated fracture[30-32]. Hence, it is important to investigate and determine the optimum process conditions for powder mixing.

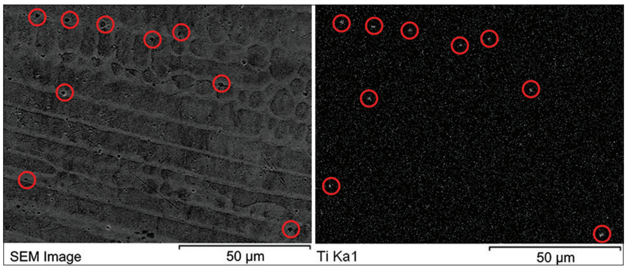

Figure 7. Energy dispersive X-ray spectroscopy element mapping for titanium. Red circles demarcate areas of high titanium concentrations, which coincide with the location of precipitates seen in the scanning electron microscopy image.

Table 6. Response for density

Level	Laser power	Scanning speed	Hopper speed
1	17.932	17.936	17.927
2	17.922	17.930	17.926
3	17.924	17.912	17.926
Delta	0.0097	0.0235	0.0009
Rank	2	1	3

The effect of each variable on the density of the DED samples is shown in Figure 8. Table 6 shows the ranks and deltas of the S/N ratios. The delta is the difference between the highest and lowest average response for each variable.

It was found that the variation of density was not significant across the various parameters and that the effect of each of the variable was negligible on the density of the DED 316/TiB_2 MMC. The spread of mean density across the DED samples was <0.5% and the delta is <0.1 for all three variables. However, the DED samples were still denser compared to same material produced using sintering and L-PBF[33]. Furthermore, no visible pore or crack was observed in the samples.

3.3. Microhardness

The mean and S/N ratio of the measured Vickers hardness of the DED samples are shown in Table 7. The mean microhardness varied between 168.5 HV and 186.4 HV, which is similar to pure 316L samples produced by DED[34].

The addition of TiB_2 did not increase the hardness as compared to DED produced 316L stainless steel. This may be due to the low actual content of TiB_2 in the obtained DED samples. AlMangour *et al.* found that there is a critical weight fraction of TiB_2 between 3 wt.% and 6 wt.% that would significantly increase the hardness values of 316L/TiB_2 MMC produced by L-PBF[33]. In addition, Du *et al.* obtained 316/TiB2 MMC with up to 900 HV using 20 wt.% TiB_2[15]. Hence, the TiB_2 content in the DED samples must be increased to achieve higher hardness.

The effect of each variable on the microhardness of DED samples is shown in Figure 9. Table 8 shows the ranks and deltas of the S/N ratio for hardness.

Table 7. Mean and S/N ratio of hardness

Taguchi Number	Laser Power	Scanning Speed	Hopper Speed	Mean Hardness	S/N
	W	mm/min	rpm	HV	
1	1000	200	200	183.5±8.5	45.244
2	1000	400	300	178.7±9.8	45.006
3	1000	600	400	186.0±8.4	45.367
4	1200	200	300	173.9±10.4	44.762
5	1200	400	400	186.4±5.1	45.399
6	1200	600	200	181.1±5.0	45.151
7	1400	200	400	181.9±9.9	45.161
8	1400	400	200	168.5±5.5	44.519
9	1400	600	300	177.6±6.1	44.977

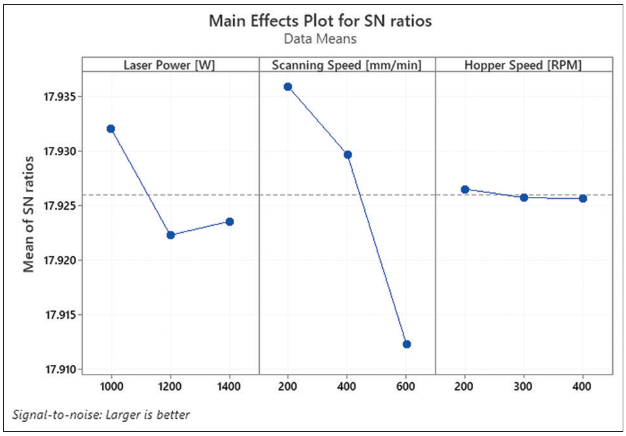

Figure 8. Main effect graph for sample density.

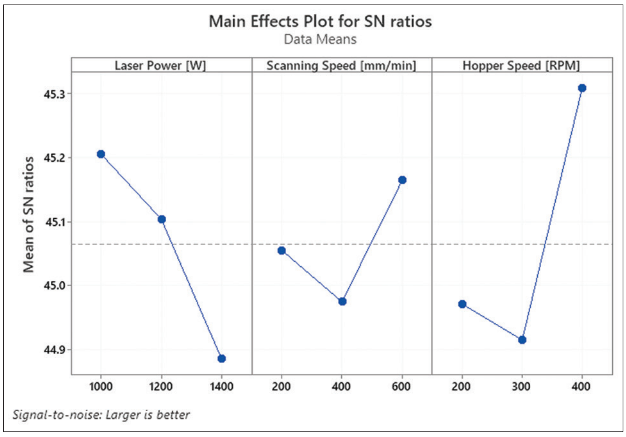

Figure 9. Main effects graph for microhardness.

Table 8. Response for microhardness

Level	Laser power	Scanning speed	Hopper speed
1	45.21	45.06	44.97
2	45.10	44.97	44.92
3	44.89	45.16	45.31
Delta	0.32	0.19	0.39
Rank	2	3	1

Hopper speed was found to be the most influential in affecting the microhardness of the DED 316L/TiB$_2$ MMC, followed by laser power and scanning speed. The optimum parameters for maximum hardness were found to be laser power of 1000 W, scanning speed of 600 mm/min, and hopper speed of 400 rpm. This gives a predicted microhardness of 182.5 HV. As these optimum parameters are identical to Taguchi No. 3, there is no confirmation run conducted. The experimental value of microhardness obtained from this run is 186.0 HV which means the predicted value has a 1.9 % error which showed the accuracy of the prediction. The Taguchi method was effective in determining the optimal set of parameters for DED 316L/TiB$_2$ MMC.

4. Conclusions

In this study, 316L/TiB$_2$ MMC was successfully fabricated using DED. The effect of DED process parameters on the microstructure and mechanical properties of 316L/TiB$_2$ MMC was studied. The L9 Taguchi array was used to vary laser power, scanning speed, and hopper speed at three levels to optimize the mechanical properties of 316L/TiB$_2$.

It was found that the laser power, scanning speed, and hopper speed had negligible effects on the density of the samples produced. Although 6 wt.% of TiB$_2$ is added, the average weight fraction of TiB$_2$ in DED 316L/TiB$_2$ was calculated to be 2 wt.%, indicating loss of TIB$_2$ during the DED process. Tumble mixing was found to be unsuitable for the preparation of powder mixture feedstock for DED as it does not result in sufficient adhesion between the TiB$_2$ and 316L stainless steel particles. No pore and crack were observed in all the DED samples. Columnar grains were found predominantly within the layers while equiaxed grains were found at the interlayer zones for the DED samples. Fine and intricate sub-grains were also observed within the grains. EDS analysis showed that the sub-grain boundaries are enriched with molybdenum and chromium. The microhardness of DED 316L/TiB$_2$ MMC ranged between 168.5 HV and 186.4 HV.

In the future, effect of different powder preparation methods for 316L/TiB$_2$ can be studied to improve the efficiency of the process. Then, the different compositions of MMC can be investigated to expand the material library available for the DED process.

Acknowledgments

The authors acknowledge the support from National Additive Manufacturing Innovation Cluster (NAMIC), Singapore, for the use of the AM facilities.

Funding

S. L. Sing would like to acknowledge the funding support from Singapore Ministry of Education Academic Research Fund Tier 1 (Award No.: 22-3721-A0001).

Conflict of interest

The authors declared no potential conflict of interest with respect to the research, authorship, and/or publication of this article.

Author contributions

Conceptualization: Swee Leong Sing
Formal analysis: Yao Ting Ang
Investigation: Joel Choon Wee Lim, Yao Ting Ang
Methodology: Swee Leong Sing, Yao Ting Ang
Project administration: Swee Leong Sing
Resources: Swee Leong Sing
Supervision: Swee Leong Sing
Validation: Joel Choon Wee Lim, Yao Ting Ang
Visualization: Swee Leong Sing, Yao Ting Ang
Writing–original draft: Swee Leong Sing, Yao Ting Ang
Writing–review and editing: Swee Leong Sing.

References

1. Herzog D, Seyda V, Wycisk E, *et al.*, 2016, Additive manufacturing of metals. *Acta Mater*, 117: 371–392.

   https://doi.org/10.1016/j.actamat.2016.07.019

2. Frazier W, 2014, Metal additive manufacturing: A review. *J Mater Eng Perform*, 23: 1917–1928.

3. Michel F, Lockett H, Ding J, *et al.*, 2018, A modular path planning solution for Wire + Arc additive manufacturing. *Robot Comput Integr Manuf*, 60: 1–11.

   https://doi.org/10.1016/j.rcim.2019.05.009

4. Ding D, Pan Z, Cuiuri D, *et al.*, 2016, Adaptive path planning for wire-feed additive manufacturing using medial axis transformation. *J Cleaner Prod*, 133: 942–952.

   https://doi.org/10.1016/j.jclepro.2016.06.036

5. Feenstra DR, Cruz V, Gao X, *et al.*, 2020, Effect of build height on the properties of large format stainless steel 316L fabricated via directed energy deposition. *Addit Manuf*, 34: 101205.

   https://doi.org/10.1016/j.addma.2020.101205

6. Saboori A, Aversa A, Marchese G, *et al.*, 2019, Application of directed energy deposition-based additive manufacturing in repair. *Appl Sci*, 9: 3316.

   https://doi.org/10.3390/app9163316

7. Dass A, Moridi A, 2019, State of the art in directed energy deposition: From additive manufacturing to materials design. *Coatings*, 9: 418.

   https://doi.org/10.3390/coatings9070418

8. Dharmawan AG, Soh GS, 2022, A cylindrical path planning approach for additive manufacturing of revolved components. *Mater Sci Addit Manuf*, 1: 3.

   https://doi.org/10.18063/msam.v1i1.3

9. Ansari M, Jabari E, Toyserkani E, 2021, Opportunities and challenges in additive manufacturing of functionally graded metallic materials via powder-fed laser directed energy deposition: A review. *J Mater Porc Technol*, 294: 117117.

   https://doi.org/10.1016/j.jmatprotec.2021.117117

10. Groden C, Traxel KD, Afrouzian A, *et al.*, 2022, Inconel 718-W7Ni3Fe bimetallic structures using directed energy deposition-based additive manufacturing. *Virtual Phys Prototyp*, 17: 170–180.

    https://doi.org/10.1080/17452759.2022.2025673

11. Sehhat MH, Sutton AT, Hung CH, *et al.*, 2022, Plasma spheroidization of gas-atomized 304L stainless steel powder for laser powder bed fusion process. *Mater Sci Addit Manuf*, 1: 11.

    https://doi.org/10.18063/msam.v1i1.1

12. Wu CL, Zhang S, Zhang CH, *et al.*, 2019, Effects of SiC content on phase evolution and corrosion behavior of SiC-reinforced 316L stainless steel matrix composites by laser melting deposition. *Optics Laser Technol*, 115: 134–139.

    https://doi.org/10.1016/j.optlastec.2019.02.029

13. Fu C, Li J, Bai J, *et al.*, 2021, Effect of helium bubbles on irradiation hardening of additive manufacturing 316L stainless steel under high temperature He ions irradiation. *J Nucl Mater*, 550: 152948.

    https://doi.org/10.1016/j.jnucmat.2021.152948

14. Ertugrul O, Enrici TM, Paydas H, *et al.*, 2020, Laser cladding of TiC reinforced 316L stainless steel composites: Feedstock powder preparation and microstructural evaluation. *Powder Technol*, 375: 384–396.

    https://doi.org/10.1016/j.powtec.2020.07.100

15. Du B, Zou Z, Wang X, *et al.*, 2008, Laser cladding of in situ TiB_2/Fe composite coating on steel. *Appl Surf Sci*, 254: 6489-6494.

    https://doi.org/10.1016/j.apsusc.2008.04.051

16. Koh HK, Moo JG, Sing SL, *et al.*, 2022, Use of fumed silica nanostructured additives in selective laser melting and fabrication of steel matrix nanocomposites. *Materials*, 15: 1869.

    https://doi.org/10.3390/ma15051869

17. Chen W, Xu L, Zhang Y, *et al.*, 2022, Additive manufacturing of high-performance 15-5PH stainless steel matrix composites. *Virtual Phys Prototyp*, 17: 366–381.

    https://doi.org/10.1080/17452759.2021.2019793

18. AlMangour B, Grzesiak D, Yang JM, 2017, Selective laser melting of TiB_2/316L stainless steel composites: The roles of powder preparation and hot isostatic pressing post-treatment. *Powder Technol*, 309: 37–48.

    https://doi.org/10.1016/j.powtec.2016.12.073

19. AlMangour B, Kim YK, Grzesiak D, *et al.*, 2019, Novel TiB_2-reinforced 316L stainless steel nanocomposites with excellent room and high-temperature yield strength developed by additive manufacturing. *Compos Part B Eng*,

156: 51–63.

https://doi.org/10.1016/j.compositesb.2018.07.050

20. Lu X, Chiumenti M, Cervera M, *et al*., 2021, Substrate design to minimize residual stresses in directed energy deposition AM processes. *Mater Des*, 202: 109525.

    https://doi.org/10.1016/j.matdes.2021.109525

21. Mukherjee T, Manvatkar V, De A, DebRoy T, 2017, Mitigation of thermal distortion during additive manufacturing. *Script Mater*, 127: 79–83.

    https://doi.org/10.1016/j.scriptamat.2016.09.001

22. Saboori A, Piscopo G, Lai M, *et al*., 2020, An investigation on the effect of deposition pattern on the microstructure, mechanical properties and residual stress of 316L produced by directed energy deposition. *Mater Sci Eng A*, 780: 139179.

    https://doi.org/10.1016/j.msea.2020.139179

23. Saeidi K, Gao X, Zhong Y, *et al*., 2015, Hardened austenite steel with columnar sub-grain structure formed by laser melting. *Mater Sci Eng A*, 625: 221–229.

    https://doi.org/10.1016/j.msea.2014.12.018

24. Tan ZE, Pang JH, Kaminski, *et al*., 2019, Characterisation of porosity, density, and microstructure of directed energy deposited stainless steel AISI 316L. *Addit Manuf*, 25: 286–296.

    https://doi.org/10.1016/j.addma.2018.11.014

25. Yadroitsev I, Krakhmalev P, Yadroitsava I, *et al*., 2013, Energy input effect on morphology and microstructure of selective laser melting single track from metallic powder. *J Mater Proc Technol*, 213: 600–613.

    https://doi.org/10.1016/j.jmatprotec.2012.11.014

26. Zhang DL, 2004, Processing of advanced materials using high-energy mechanical milling. *Prog Mater Sci*, 49: 537–560.

27. Suryanarayana C, Ivanov E, Boldyrev VV, 2002, The science and technology of mechanical alloying. *Mater Sci Eng A*, 304–306: 151–158.

    https://doi.org/10.1016/s0921-5093(00)01465-9

28. Fogagnolo JB, Velasco F, Robert MH, *et al*., 2003, Effect of mechanical alloying on the morphology, microstructure and properties of aluminium matrix composite powders. *Mater Sci Eng A*, 342: 131–143.

    https://doi.org/10.1016/s0921-5093(02)00246-0

29. Xu H, Lu Z, Jia C, *et al*., 2015, Influence of mechanical alloying time on morphology and properties of 15Cr-ODS steel powders. *High Temperature Materials and Processes*, 35: 473–477.

    https://doi.org/10.1515/htmp-2014-0229

30. Zhao Q, Yu L, Liu Y, *et al*., 2015, Morphology and structure evolution of Y_2O_3 nanoparticles in ODS steel powders during mechanical alloying and annealing. *Adv Powder Technol*, 26: 1578–1582.

    https://doi.org/10.1016/j.apt.2015.08.017

31. Rahmanifard R, Farhangi H, Novinrooz AJ, 2010, Optimization of mechanical alloying parameters in 12YWT ferritic steel nanocomposite. *Mater Sci Eng A*, 527: 6853–6857.

    https://doi.org/10.1016/j.msea.2010.07.048

32. Si C, Zhang Z, Zhang Q, *et al*., 2021, Influence of mechanical alloying on the particle size, microstructure and soft magnetic properties of coarse Fe-based amorphous powders prepared by gas atomization. *J Non Cryst Solids*, 559: 120675.

    https://doi.org/10.1016/j.jnoncrysol.2021.120675

33. AlMangour B, Grzesiak D, Yang JM, 2016, Rapid fabrication of bulk-form TiB_2/316L stainless steel nanocomposites with novel reinforcement architecture and improved performance by selective laser melting. *J Alloys Comp*, 680: 480–493.

    https://doi.org/10.1016/j.jallcom.2016.04.156

34. Sarma IK, Srinivas V, Subbu SK, 2021, Effect of process parameters on micro hardness, bulk hardness and porosity of LENS^{TM} deposited SS 316L alloy. *Mater Today Proc*, 46:2616–2624.

    https://doi.org/10.1016/j.matpr.2021.02.268

WHIOCE PUBLISHING PTE. LTD. Materials Science in Additive Manufacturing

REVIEW ARTICLE

Cold spray additive manufacturing of copper-based materials: Review and future directions

Vineeth Menon[1], **Clodualdo Aranas Jr.**[2]*, **Gobinda Saha**[1]

[1]Nanocomposites and Mechanics Laboratory, University of New Brunswick, Fredericton, Canada

[2]Alloy Design and Materials Testing Research Laboratory, University of New Brunswick, Fredericton, Canada

Abstract

The cold gas dynamic spray process is a manufacturing process strategically designed for coatings. The conditions for the deposition of materials to form coatings have evolved over several decades. Copper and copper-based cold spray coatings are an interesting field for investigation, as it has substantial commercial demand and acceptance. Several important works have already been performed in this regard that shows the immense popularity of its applications in power industries. Cold gas dynamic spray, being an economic process, can produce coatings with superior quality and low oxidation. In this paper, a particular focus has been given to copper-based cold spray coatings along with their deposition parameters. The various mechanical, electrical, corrosion, and tribological properties of these copper-based cold spray coatings are commendable and economically lucrative. A good amount of experimental data has also been included in this review article to provide comprehensive information and future scope of research about copper-based cold spray coatings.

Keywords: Cold spray; Copper-based alloys; Coatings

1. Introduction

Copper, having good ductility and exceptional thermal and electrical properties, has a great potential to be employed as coatings for different substrates according to their commercial acceptance in aerospace, automobile, power, and metallurgical industries. There are several coating processes to form copper-based coatings with various reinforcements, such as the cold gas dynamic spray process (CGDS), which is a prominent and essential additive manufacturing technique for research and industrial applications. The cold gas dynamic spray additive manufacturing technique has a wide commercial acceptance. This technique was first developed in the 1980s at the Institute of Theoretical and Applied Mechanics of the Siberian division of the Russian Academy of Science at Novosibirsk[1,2]. To date, the cold spray process technology is gaining a lot of attention from researchers for its exceptional capability of depositing powders onto the substrate without any high-temperature phase transformations or oxidation. The dense and adequately thick coatings having proper corrosion resistance and desirable mechanical properties make cold-sprayed coatings supreme. The CGDS is a low-temperature process that sprays powder particles onto a substrate; these

***Corresponding author:**
Clodualdo Aranas Jr.
(clod.aranas@unb.ca)

Citation: Menon V, Aranas Jr. C, Saha G, 2022, Cold spray additive manufacturing of copper-based materials: Review and future directions. *Mater Sci Add Manuf.* 1(2): 1-20. https://doi.org/10.18063/msam.v1i2.12

Received: April 28, 2022

Accepted: June 8, 2022

powder particles are accelerated with the help of carrier gas. Hence, the particles impact the substrate with high kinetic energy and form the coatings[3-5].

1.1. Production of metal powders

There are several methods to produce metal powders required for spraying purposes, additive manufacturing, and other fields. These methods include mechanical milling, atomization, chemical precipitation, and reduction. In the atomization process, the liquid metal alloy is continuously dispersed in the form of fine droplets due to the impact of the medium used for atomization. The different types of atomization processes are gas, water, plasma, and centrifugal atomization; plasma and gas atomization techniques are the most popularly used[6]. However, the spherical powders produced by such techniques have a low cold spray deposition efficiency compared to irregular-shaped powders. For this reason, mechanical milling remains a popular choice for creating powders for the cold spraying process[7].

1.2. Powder feedstock preparation for cold spraying

A prominent powder processing technique for processing the powder feedstock before the cold spraying is mechanical ball milling. In this process, the powder mixtures are subjected to high-energy collision by the impact of metallic balls, leading to two opposing mechanisms, and these mechanisms are cold welding and fracturing of the powder particles. A higher amount of ceramic reinforcements leads to more fracturing of powder particles; hence, smaller powder sizes can be achieved. Furthermore, these ball-milled powders are then cold sprayed with the help of a convergent-divergent nozzle and a carrier gas to increase the speed of powder particles to supersonic velocity[8]. The convergent-divergent nozzle has an inlet and outlet with a pressure difference existing between them. The gas flows in the convergent part of the nozzle at a subsonic speed and then accelerates to supersonic velocity in the divergent part of the nozzle. The parameters such as dimensions of the nozzle, type of the gas used, gas temperature, and pressure help determine the in-flight characteristics of the powder particles[7].

1.3. Role of surfactants in mechanical alloying

Mechanical treatment by ball milling is advantageous for the preparation of composite powders[9-13]. Mechanical alloying involves mixing different metals and forming an intimate powder mixture as a product. On the other hand, mechanical milling is a process of reducing the powder sizes with uniform chemical composition. These two processes take place due to the high-energy impact of the balls on the powder particles, resulting in cold welding and fracturing. As a result, the powder particles always have atomistic clean surfaces that might allow them to get combined, resulting in welding. However, with time, plastic deformation of powder particles also increases, leading to the fracture of particles. In this process, the powder particles may probably adhere to the vial and ball surfaces. Ductile particles are more prone to the cold welding process. The cold welding of ductile particles can be controlled either by altering the surface of these particles or by milling at cryogenic temperatures[14].

The altering of the surface of powder particles can be achieved using process control agent (PCA) or commonly referred to as surfactants. The surfactants get absorbed into the powder particle surfaces, as shown in Figure 1, which results in a decrease in cold welding and an increase in fracturing. This may be due to the decrease in surface energy of the newly formed surfaces of powder particles, which prevents them from cold welding. The use of surfactants in the milling of ductile powder particles increases powder yield.

The amount of surfactant used should be appropriate enough to cover the surfaces of the powder particles completely so as to serve as a deterrent to cold welding of the particles. Moreover, the quantity of surfactant required for the purpose of milling is dependent on: (i) The ductility of the powders to be milled, (ii) thermal as well as chemical cost ability of the PCA or surfactants, (iii) quantity of powder to be milled and its initial size, and (iv) duration of milling. For example, the amount of surfactant for ductile materials is higher than that of the brittle materials. Surfactants with a large molecular weight (like stearic acid) form monolayers by adsorption on powder particles. On

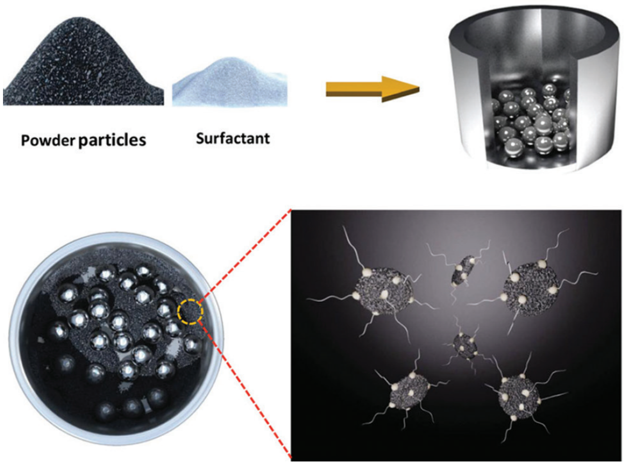

Figure 1. Surfactant added to the powders for ball milling. Surfactants get adsorbed to the surface of the powder particles preventing them from agglomeration[14]. (Reprinted from *Critical Reviews in Solid State and Materials Sciences*, 39(2), Nouri, A., and Wen, C, Surfactants in Mechanical Alloying/Milling: A Catch-22 Situation, 81 – 108, 2014, with permission from Taylor and Francis).

the other hand, methanol (with lower molecular weight) allows multilayer formations on the powder particles. The multilayer formation can reduce the cold welding of the powder particles while milling[14]. Kollo *et al.*[15] investigated that there was no sticking of aluminum silicon carbide powders on the milling tool when heptane was utilized instead of stearic acid as a surfactant. Some other factors governing the quantity of surfactant required for mechanical milling/alloying processes are speed of milling, milling temperature, and ball-to-powder ratio. These factors can greatly affect the adsorption of surfactants on the surface of the powder particles.

Lu and Zhang[16] demonstrated the effect of the amount of surfactants used during milling on the milling time. They reported that the aluminum-magnesium powder yield after milling with 4 wt.% stearic acid was much higher than the milling done with 1 wt.% stearic acid for the same milling time. Another critical observation by Shaw *et al.*[17] was the decrease in crystallite size with the increase in milling time. However, with the increase in the amount of surfactants, the actual crystallite size increases. They reported that powders milled for 4 h without any surfactant had the same crystallite size as that of powders milled for 8 h with 1 wt.% stearic acid and almost the same for powders milled for 16 h with 2 wt.% stearic acid. Furthermore, the hardness of powders is affected by the reaction of surfactants with powder particles. Kollo *et al.*[15] observed that when heptane was used as a surfactant, the hardness of powder particles was less compared to the case when stearic acid was used as a surfactant during milling. Therefore, the choice of surfactant and its amount to be used for milling have great significance in deciding the milling parameters before cold spraying the milled powders.

1.4. Cold spray process

Among additive manufacturing-based technologies, there are two distinct groups of techniques primarily divided based on their functional task, material types being handled, or the degree of complexity in their deposition process. These are powder based and non-powder based. In the non-powder feed method, such as wire arc AM or laser melt deposition wire, a wire feed is melted in a nozzle through plasma arc or laser. Whereas in the powder feed deposition method, the powder as feedstock is sprayed onto a substrate in a supersonic/transonic atmosphere to develop 3D coatings or freeform objects through self-consolidation. The technique thus works as a direct AM process in high productivity requirements.

The common denomination among the two groups is the requirement of a high thermal energy source, either in the form of laser, oxy-fuel combustion, flame spray, or detonation spray. Compared with these technologies, cold spray neither uses high temperature (e.g., selective laser melting or direct metal deposition) nor engages in complex chemical processes (e.g., electroplating). This makes cold spray the best fit for working with geometries of complex shapes and simultaneously accomplishing deposition without thickness limitation. According to ASTM F2792-12A standard, cold spray is a promising AM technology in the industry-scale manufacturing landscape. This standard is later replaced by ISO/ASTM 52900:2021.

In the cold spray process, the parameters that determine a successful deposition also include particle morphology shape, type of the material, and the standoff distance between substrate and nozzle. The gases used for cold spray are helium, nitrogen, and air[7]. Helium is costly and is helpful in cases where powder particles should reach high critical velocity required for highly dense coatings. Helium provides a good working temperature; however, nitrogen and air can cut the cost of the manufacture of coatings[18]. Nitrogen can also prevent oxidation of the coatings[7]. Furthermore, annealing treatments could be a good alternative to increase the denseness of the coatings instead of using a costly process gas[19].

The typical size range of the powder particles required for a successful cold spray should be less than 100 μm. The particles having a size larger than 100 μm may not get cold sprayed as they are difficult to get accelerated to supersonic velocity by the carrier gas. In general, for depositing composite powders, the spray conditions and parameters are typical, and they may not be the same as the parameters used for single-powder deposition. Before spraying, the different powders are mechanically milled together to make composite agglomerate. In a cermet powder feedstock, the metal powder particles act as a binder and help to ameliorate bonding. A combination of soft metal powders and hard ceramic powders can prevent damage to the hard ceramic particles and, hence, help in retaining the desired properties intended. This mechanical milling also enhances the deposition efficiency and forms thick coatings[7,20]. Figure 2 shows the parameters required to obtain a successful cold-sprayed coating.

1.5. The metal-ceramic interface bonding characteristics in the cold spray process

Combining ceramics and metals is difficult due to their different bonding characteristics. In ceramics, atoms have ionic and covalent bonds; on the other hand, metals are normally associated with metallic bonds. The flow of electrons is restricted in ceramics. Moreover, the stable ionic and covalent bonds in ceramics reduce surface interactions, reducing adherence with metal. There is also a mismatch in the thermal expansion coefficient of metal and ceramic, which makes the bonding difficult and may also result in interfacial cracks. Cold spray is an excellent technique for making an effective metal-ceramic interface because it is a low-temperature process that avoids any melting of particles or phase transformations. The effectiveness of adherence between metal-ceramic interfaces produced by the cold spray technique can have a great effect on their mechanical and tribological properties[21].

The powder particles, having a velocity greater than the critical velocity, get deposited on the substrate. These powder particles with high supersonic velocity bombard the surface of a substrate and essentially perform the desired work of removing the oxide layer on the substrate, enhancing the bonding of coatings to the substrate in the presence of ceramic particles along with the metal particles, enhancing the bonding characteristics. The ceramic particles do not deform themselves, but they distort the ductile metal matrix and enhance the bonding. These ceramic particles may also break into fragments and, hence, get embedded in the metal matrix all around, which may eventually increase the hardness of the coatings. The cermet particles serve the following functions: (i) Cleaning the nozzle, (ii) activating the sprayed surface, and (iii) densifying the structure[3,22].

2. Pure copper cold spray coatings

Copper as an element specifically known for its exceptional electrical and thermal conductivities is greatly used for thermal and electrical applications commercially in various industries. Several studies have been conducted to explore the properties of pure copper and copper-based cold spray coatings to prove its superiority in terms of quality, sustainability, and economy as compared to other available methods for producing coatings.

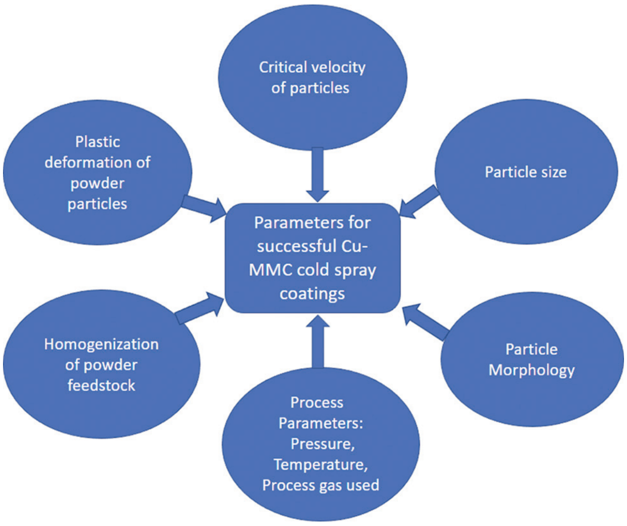

Figure 2. Parameters for successful Cu-MMC cold spray coatings.

Fukumoto *et al.*[23] reported the study of deposition behavior and efficiency of cold-sprayed copper coatings with respect to changes in substrate temperature, particle velocity, gas pressure, and gas temperature. The copper particles have mean sizes 5, 10, and 15 μm. According to their observations, the 5 μm copper particles produced an increase in particle velocity with an increase in gas pressure during the cold spraying process. However, the effect of gas temperature was not significant on particle velocity. The particle velocity was highest for 5 μm copper particles and lowest for 15 μm copper particles; this observation shows that particle velocity significantly varies with particle mean size. Moreover, higher copper particle velocity leads to better deposition efficiency.

In the same study, it was also reported that an increase in the temperature of the substrate could lead to improved deposition. This increase was even more pronounced when both pressures of the gas and substrate temperature were increased. Figure 3 shows the increase in deposition of copper particles with respect to the substrate temperature and pressure. This observation could be of good use in designing the parameters for cold spray deposition[23].

Borchers *et al.*[24] studied the deformation behavior of cold-sprayed copper coatings by focusing on various areas in the coating microstructures seen in the transmission electron microscopy micrographs (Figure 4). The regions marked as A, B, C, and D in the micrograph correspond to the copper particle-particle boundaries. Region “D” shows

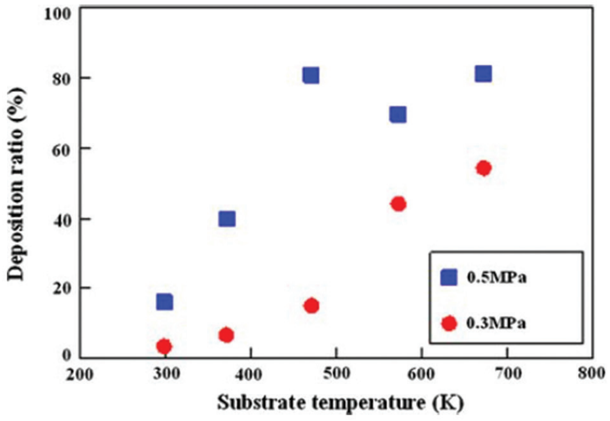

Figure 3. Deposition of copper particles with respect to substrate temperature and gas pressure[23]. (Reprinted from *Journal of Thermal Spray Technology*, 16, Fukumoto, M., Wada, H., Tanabe, K., Yamada, M., Yamaguchi, E., Niwa, A., Sugimoto, M., and Izawa, M., Effect of Substrate Temperature on Deposition Behavior of Copper Particles on Substrate Surfaces in the Cold Spray Process, 643-650-108, 2007, with permission from Springer Nature).

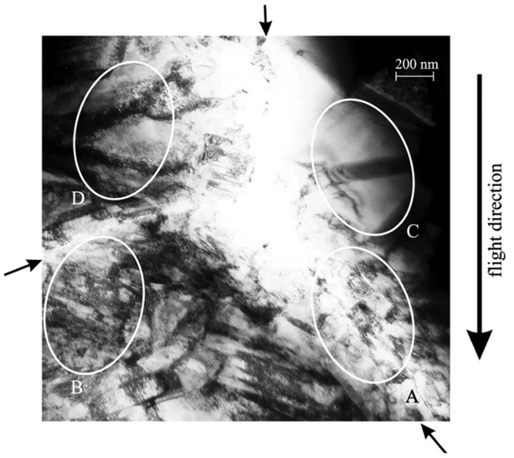

Figure 4. A particle-particle triple point of cold-sprayed copper coating is seen in this TEM micrograph[24]. (Reprinted from Materials Research Society Symposium – Proceedings, 674, Borchers, C., Stoltenhoff, T., Gärtner, F., Kreye, H. and Assadi, H., Deformation microstructure of cold gas sprayed coatings, P7.10.1-P.10.6, 2001, with permission from Springer Nature).

high dislocation density having dislocation arrangement in walls. The marked Region "B" displays aligned elongation of grains with high dislocation density. Then, Region "A" reveals the ultrafine grains with high dislocation density, specifically at the grain boundaries. Finally, Region "C" shows dislocation-free regions having deformation twins. The direction of flight of the particles has been marked on the micrograph along with three other directions showing the particle-particle interface.

Basically, particles can be seen making a triple point. Between Regions B and D, the particle-particle interface is 70°, and between Regions A and C, the particle-particle interface is 45°. As seen in the micrograph, there are particles impacting at different angles, according to which the local temperatures may also be different. This may give rise to the process of recrystallization, which can account for microstructural changes as compared to the initial powder feedstock. As discussed by Borchers *et al.*[24], Region C consisted of twins. This could be due to the high strain rate deformation and subsequent recrystallization during annealing caused by local temperature increase. Due to the extremely short cooling time of around 10^{-4} s, the fraction of coating that has recrystallized is very less. As far as the deformation in Regions A, B, and D is concerned, there could be several steps into which the whole recrystallization process can be divided; first, the formation of randomly distributed dislocations; second, the development of long dislocation cells due to dynamic recovery; and third, the elongated subgrains form, followed by the breaking up and formation of small equiaxed grains. In Region A, the rise in temperature is the highest because of the equiaxed grains visible in this region. However, in Region B, only the breaking up of elongated subgrains was visible, suggesting that the temperature increase was not too high as compared to the region A. Furthermore, in Region D, only dislocation cells were seen and not the subgrains, which shows that the temperature rise was even lesser as compared to the Region B as well as A.

Borchers *et al.*[24] also measured the resistivity of the copper coatings, which was identified to have values close to the resistivity of cold-rolled copper sheets. In their work, they suggested that the cold-sprayed coatings can acquire better electrical properties when compared to high-velocity oxygen fuel (HVOF)-fabricated copper coatings. The copper coatings produced by cold spray were very dense, consisting of good metallic bonding between the particles. Most importantly, the oxide formation was negligible in cold-sprayed copper coatings. However, the bond strength of HVOF copper coatings is higher than the bond strength of copper cold spray coatings.

3. Copper-based metal matrix composite cold spray coatings

The metal matrix composite coatings with copper as the base metal are of great commercial importance. Copper-based MMC coatings can be utilized in power industries, especially in the manufacturing of seam welding electrodes, electrical contacts, lead wires, and conductors for high-temperature electrical applications. These coatings can be produced through techniques such as HVOF and CGDS. The oxide formations and phase transformations in the HVOF coatings degrade the properties of the coatings. The CGDS process is currently being utilized in fabricating various copper-based MMC coatings. Several reinforcements such as SiC, CNT, AlN, graphene, alumina, MoS_2, WC, and TiB_2 have been employed to make successful cold spray coatings. Each reinforcement has characteristic properties; thus, they are selected accordingly to impart the same worthy properties in the copper metal matrix composite coatings. Several research projects have already been done in this area, proving the worth of such composite coatings, which are reviewed in the next section.

4. Recent investigations into copper-based MMC coatings

4.1. Copper-alumina cermet coatings

Several studies have been done on copper as a metallic matrix with ceramic reinforcement (also known as cermets). Recently, special attention has been given to ameliorating mechanical properties and wear resistance of various copper-based coatings using hard particles as additives[25-27]. For example, Koivuluoto *et al.* successfully deposited copper + alumina coatings onto a substrate via cold spray process. Dendritic and spherical copper powders were mixed with 10 vol.%, 30 vol.%, and 50 vol.% of alumina. Then, its cold spraying characteristics were compared with that of the pure copper coatings made with dendritic and spherical copper powders. The thickness of the copper-alumina coatings increased with the increasing amount of alumina ceramic particles, mainly due to the hammering effect of alumina particles on the ductile copper matrix. The shot peening effect of the ceramic particles deforms the copper powders; thus, porosity decreases, which enhances the bonding characteristics. According to Koivuluoto *et al.*, the densest coatings obtained were for dendritic copper + 50 vol.% alumina and 10 vol.% alumina + spherical copper. Figures 5-8 show the field emission scanning electron microscopy (SEM) micrographs of these coatings. The reason for this, as reported, was that the dendritic copper particles have a higher surface area and are more prone to oxidation as compared to the spherical copper powders. Eventually, these dendritic copper powders require more deformation to achieve better metal-metal bonding and an effective dense coating. However, the Vickers hardness of copper + alumina coatings showed a constant rise with the increase in alumina particles for the coatings obtained. With both dendritic and spherical copper particles, the Vickers hardness for all the coatings obtained with spherical copper powders is higher (ranging between 106 Hv and 127 Hv) when compared to the coatings obtained with dendritic copper particles (ranging 83 – 103 Hv). The corrosion resistance of these coatings made with spherical copper powders + alumina was higher than the dendritic copper powder coatings. The spherical copper + alumina powder coatings were denser, as reported in the literature[28].

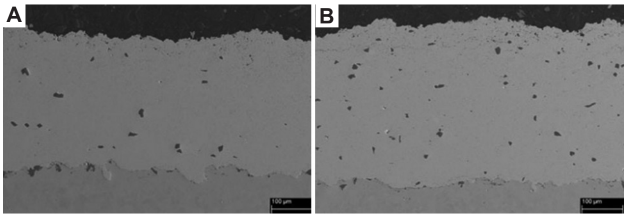

Figure 5. Field emission scanning electron microscopy micrographs of (A) dendritic copper + 10 vol.% Al_2O_3 and (B) dendritic copper + 30 vol.% coatings on steel substrate[28]. (Reprinted from *Journal of Thermal Spray Technology*, 19(5), Koivuluoto, H., and Vuoristo, P., Effect of Powder Type and Composition on Structure and Mechanical Properties of Cu + Al_2O_3 Coatings Prepared using Low-Pressure Cold Spray Process, 1081 – 1092, 2010, with permission from Springer Nature).

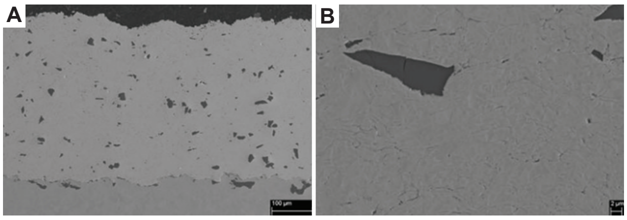

Figure 6. Field emission scanning electron microscopy micrographs of (A) dendritic copper + 50 vol.% Al_2O_3 coatings on steel substrate and its (B) detailed microstructure[28]. (Reprinted from *Journal of Thermal Spray Technology*, 19(5), Koivuluoto, H., and Vuoristo, P., Effect of Powder Type and Composition on Structure and Mechanical Properties of Cu + Al_2O_3 Coatings Prepared using Low-Pressure Cold Spray Process, 1081 – 1092, 2010, with permission from Springer Nature).

In another work, Phani *et al.*[29] successfully cold-sprayed nanocrystalline copper-alumina powders and studied the effect of heat treatments at the temperatures of 300°C, 600°C, and 950°C, and inferred that alumina particles were effective in stopping the grain growth, which is of immense value for commercial applications. Figure 9 shows the micrographs of the as-sprayed and heat-treated coatings. The variation in the grain size due to the heat treatments, as reported, was significantly less for copper-alumina coatings compared to pure copper coatings. The same trend was detected for microhardness, where nanocrystalline copper-alumina coatings had higher hardness than the pure copper coatings for all heat treatment temperatures. As reported, the copper-alumina

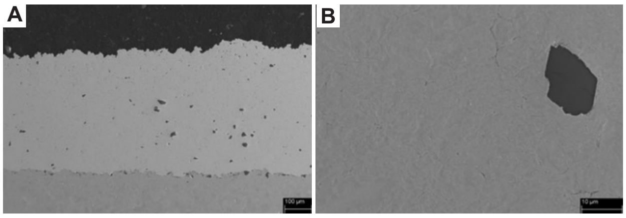

Figure 7. Field emission scanning electron microscopy micrographs of (A) spherical copper + 10 vol.% Al_2O_3 coatings on steel substrate and its (B) detailed microstructure[28]. (Reprinted from *Journal of Thermal Spray Technology*, 19(5), Koivuluoto, H., and Vuoristo, P., Effect of Powder Type and Composition on Structure and Mechanical Properties of Cu + Al_2O_3 Coatings Prepared using Low-Pressure Cold Spray Process, 1081 – 1092, 2010, with permission from Springer Nature).

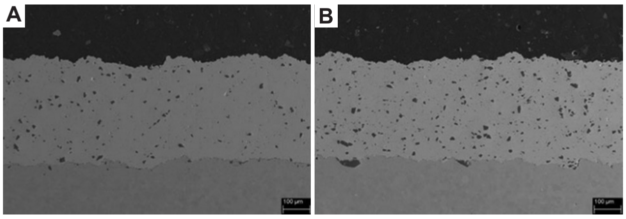

Figure 8. Field emission scanning electron microscopy micrographs of (a) spherical copper + 30 vol.% Al_2O_3 and (B) spherical copper + 50 vol.% coatings on steel substrate[28]. (Reprinted from *Journal of Thermal Spray Technology*, 19(5), Koivuluoto, H., and Vuoristo, P., Effect of Powder Type and Composition on Structure and Mechanical Properties of Cu + Al_2O_3 Coatings Prepared using Low-Pressure Cold Spray Process, 1081 – 1092, 2010, with permission from Springer Nature).

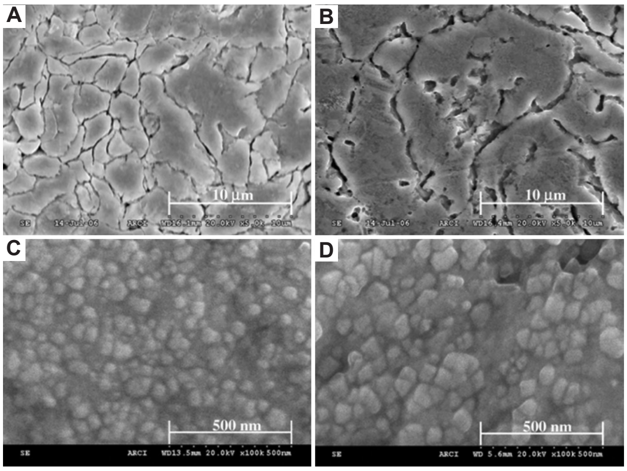

Figure 9. Microstructure of (A) copper coating (as-sprayed), (B) copper coating heat treated at 950°C, (C) copper-alumina coating (as sprayed), and (D) copper-alumina coating heat treated at 950°C[29]. (Reprinted from *Acta Materialia*, 55, Sudharshan Phani, P., Vishnukanthan, V., and Sundararajan, G., Effect of heat treatment on properties of cold-sprayed nanocrystalline copper-alumina coatings, 4741 – 4751, 2007, with permission from Elsevier).

coatings showed only a 9% reduction in hardness post-heat treatment at 950°C, whereas the pure cold-sprayed copper showed a 55% decrease in hardness, which gives nanocrystalline copper-alumina coatings an edge over coarse-grained copper coatings. The electrical conductivity of nanocrystalline copper-alumina coatings was reported to be around 20 – 25 MS/m, which is lesser than the conductivity of nanocrystalline copper coatings which had a reported value of around 50 MS/m. This electrical conductivity behavior of the coatings could be attributed to the presence of alumina ceramic particles[29].

In addition to the studies above, Winnicki *et al.*[30] studied the corrosion resistance of copper-alumina cold spray coatings with cyclic salt spray and Kesternich tests. As reported, even after 18 cycles of NaCl sprays on copper-alumina coatings, there was no significant corrosion, possibly because of the low amount of ceramic particles in the Cu + Al_2O_3 coating accounting to lesser weak metal ceramic interfaces allowing the chloride ions to penetrate in them, so there was no buckling in the coatings. However, for the Kesternich test performed in sulfur dioxide environment, there were some small cracks at the boundary between the substrate and the coatings. Furthermore, the electrical conductivity test performed on copper-alumina coatings also did not show a huge difference in electrical conductivity between as-sprayed copper-alumina coatings and the copper-alumina coatings after the two corrosion tests (salt spray and Kesternich tests). The electrical conductivity reported for as-sprayed copper-alumina coating was 62% IACS. However, interestingly, the drop in electrical conductivity of copper-alumina coatings was very less after the salt spray test and Kesternich test. Electrical conductivity values of 51% IACS and 58% IACS were measured for copper-alumina coatings after salt spray and Kesternich tests, respectively. According to the analysis, there were layers of $Cu_2Cl(OH)_3$ (paracetamite), which might also enhance corrosion resistance[30].

Chen *et al.*[31] prepared copper-alumina-graphite cold-sprayed coatings (for lubrication purposes) with 304 stainless steel plates as substrates. The feedstock powders prepared were pure copper, copper-alumina (10 wt.%), and copper-alumina (10 wt.%)-copper-coated graphite (5 wt.%, 10 wt.%, and 20 wt.%) powders. As reported, the pure copper coatings had around 365 µm thickness along with small pores. However, with the incorporation of 10 wt.% alumina, the number of pores was significantly reduced, possibly due to the hammering effect of alumina ceramic particles. The thickness of the coating also drastically improved to 859 µm. However, with the addition of copper-coated graphite, the thickness of coatings was reduced to 480, 400, and 562 µm for copper-alumina (10 wt.%)-copper-coated graphite (5 wt.%, 10 wt.%, and 20 wt.%) cold-sprayed coatings, respectively. Figure 10 shows SEM micrographs of Cu-based solid lubricating cold spray coatings.

As reported, among the hardness values of copper-based coatings, copper-alumina coatings had the highest Brinell hardness of 114.3 as compared to the pure copper coating with a Brinell hardness of 97.0 as well as with copper-alumina-copper-coated graphite coatings ranging around 107.3 – 88.2. There was a decrease in hardness with the increasing amount of copper-coated graphite in the copper-based LPCS solid lubricant coatings. The lamellas of copper in the copper-alumina-copper-coated graphite 5 wt.% are large with less plastic deformation. However, with the increase in copper-coated graphite content from 5 wt.% to 10 wt.% and further to 20 wt.%, the relative plastic deformation increased, which could be mainly due to the hammering effect and the relatively higher amount of alumina in copper-alumina (10 wt.%)-copper-coated graphite (10 wt.% and 20 wt.%)[31].

Dry sliding wear performance of copper-based solid lubrication coatings was also studied by Chen *et al.*[31]; they found that the pure copper coatings had a friction coefficient of 0.82 and the copper-alumina coatings had a friction coefficient of 0.94. With the incorporation of copper-coated graphite, the friction coefficient was reduced due to the increase in solid lubrication. The reported values of friction coefficients were 0.69, 0.29, and 0.34 for copper-alumina (10 wt.%)-copper-coated graphite (5 wt.%, 10 wt.%, and 20 wt.%) cold-

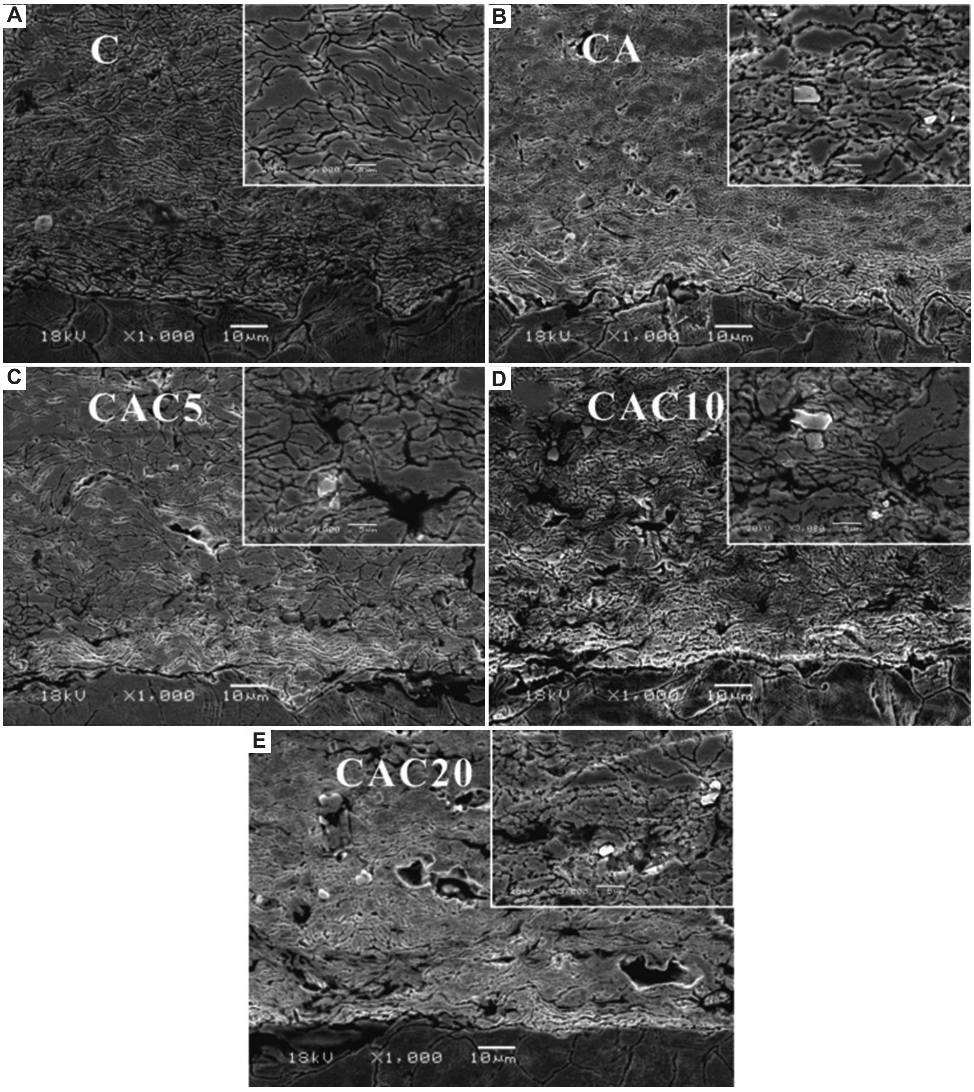

Figure 10. Scanning electron microscopy micrographs of Cu-based solid lubricating cold spray coatings: (A) Copper, (B) copper-alumina, (C) copper-alumina-copper-coated graphite 5 wt.%, (D) copper-alumina-copper-coated graphite 10 wt.%, and (E) copper-alumina-copper-coated graphite 20 wt.%[31]. (Reprinted from *Journal of Thermal Spray Technology*, 27(8), Chen, W., Yu, Y., Cheng, J., Wang, S., Zhu, S., Liu, W., and Yang, J., Microstructure, Mechanical Properties and Dry Sliding Wear Behavior of Cu-Al_2O_3-Graphite Solid-Lubricating Coatings Deposited by Low-Pressure Cold Spraying, 1652 – 1663, 2018, with permission from Springer Nature).

sprayed coatings, respectively. The wear rate of these copper-based coatings also improved with the addition of copper-coated graphite. The reported values were 2.53×10^{-4} mm^3/Nm, 2.18×10^{-4} mm^3/Nm, and 1.2×10^{-4} mm^3/Nm for copper-alumina (10 wt.%)-copper-coated graphite (5 wt.%, 10 wt.%, and 20 wt.%) cold-sprayed coatings, respectively. Graphite helps in the formation of tribolayer, and the alumina particles provide load support. The combination of both provides the lowest wear rate for the copper-alumina (10 wt.%)-copper-coated graphite (20 wt.%) cold-sprayed coating. The increase in the amount of graphite in the coatings leads to a lower wear rate of the coating.

In Figure 11, the worn-out cross-section of pure copper, copper-alumina, and copper-alumina (10 wt.%)-copper-coated graphite (10 wt.%) cold-sprayed coatings is presented. As reported and seen in the microstructure, a mixed tribolayer was formed on the pure copper coatings, with a thickness of around 5 – 10 µm with a mixture of large and ultrafine grains, possibly due to the plastic deformation of pure copper. The presence of ultrafine grains improves the plastic deformation and, thereby, the strength and wear resistance of the material. However, the addition of alumina ceramic particles may induce cracks during wear test because of the incompatibility at the ceramic metal matrix interface. However, for the case of copper-alumina (10 wt.%)-copper-

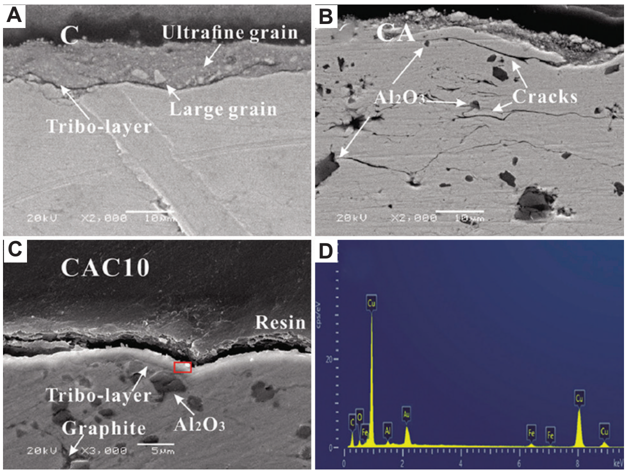

Figure 11. Scanning electron microscopy micrographs of wear cross-section regions in copper-based coatings: (A) Pure copper, (B) copper-alumina (10 wt.%), (C) copper-alumina (10 wt.%)-copper-coated graphite (10 wt.%), and (D) energy-dispersive spectrum of copper-alumina (10 wt.%)-copper-coated graphite (10 wt.%) tribolayer[31]. (Reprinted from *Journal of Thermal Spray Technology*, 27(8), Chen, W., Yu, Y., Cheng, J., Wang, S., Zhu, S., Liu, W., and Yang, J., Microstructure, Mechanical Properties and Dry Sliding Wear Behavior of Cu-Al2O3-Graphite Solid-Lubricating Coatings Deposited by Low-Pressure Cold Spraying, 1652 – 1663, 2018, with permission from Springer Nature).

coated graphite (10 wt.%) cold-sprayed coating, a tribolayer of copper, alumina, and graphite enhanced the solid lubrication, which resulted in no crack formation[31].

4.2. Copper-carbon nanotube (CNTs) coatings

The CNTs have excellent properties such as stiffness, strength, elastic modulus, electrical, and thermal conductivities. Because of the properties of CNTs, the studies on the incorporation of CNTs in composites are widely pursued[6,32-37]. CNTs can be used as reinforcements in improving strength of composites[38-40]. In 2012, Cho *et al.*[41] prepared multi-walled CNT (MWCNT) reinforced copper coatings by cold spray method. As reported, they could substantially avoid the structural damage caused to the CNTs by the low-pressure cold spray process compared to other thermal and high-pressure fabrication processes. In their work, the ball milling process employed to mix the CNTs with copper powder ensured a satisfactory level of mixing of the particles before spraying. The 3 vol.% multi-walled CNT in copper powder feedstock was successfully sprayed onto the aluminum substrate, and the coatings produced had high thermal diffusivity compared to pure copper coatings. The CNTs were homogeneously dispersed in the copper matrix, which accounted for high thermal diffusivity. In some previous reports, the presence of bundled or non-homogeneous dispersion of CNT decreases thermal diffusivity[42,43]. Therefore, Cho *et al.* employed ball milling as an effective strategy to enhance the homogeneous distribution of CNTs in the copper matrix. The MWCNT and copper had good clean and closed interfaces, contributing to low thermal resistance. Furthermore, these were moderately damaged by the ball milling process, which helped retain the desirable properties in the coatings.

In another study, Pialago and Park[44] further increased the amount of CNTs in the copper composite powder feedstock to 15 vol.%. They successfully deposited copper CNT composite powders via cold spray process after ball milling. According to the report, with the increase in the volume percent of CNT reinforcement particles in the feedstock (ranging from 5 to 15 vol.%), the deposition efficiency decreased. Furthermore, the particle size decreases with increasing ceramic content, mostly because the embedded CNTs initiated the cracks during ball milling. This process enhanced the fracturing against the cold welding process of the particles. The cold welding and fracturing of the powder particles may also vary with different milling parameters such as powder composition, size of the balls used, ball-to-powder ratio, and time of milling[44].

Furthermore, from the study by Pialago *et al.*[45], they fabricated copper-based metal matrix composites with CNT and SiC additions (Figure 12). The compositions they made were copper 5%CNT, copper 5%CNT-10%SiC, and copper 5%CNT-20%SiC along with pure copper coatings. As expected, it was reported that with the increase in ceramic content, the fracturing of powder particles (while milling) decreased compared to cold welding, possibly because the CNT and SiC served as crack initiators. Interestingly, the copper 5%CNT-20%SiC was an exception as there was an agglomeration in these powder particles because of increased surface energy due to a reduction in the size of particles. A similar trend was seen in deposition efficiency, where pure copper had the highest deposition efficiency. However, the deposition efficiency decreased with increasing ceramic content for copper 5%CNT and copper 5%CNT-10%SiC. Note that copper 5%CNT-20%SiC had deposition efficiency and coating thickness almost equivalent to pure copper coatings. The reason reported for this exception was the increased amount of ceramics that enhance metal deformation and increase deposition efficiency. Furthermore, copper 5%CNT-20%SiC coatings had the highest hardness, around 240 $Hv_{0.1}$, as compared to all other coatings[45].

The cold spray ternary coatings of copper-CNT-AlN composites were also studied in the literature[46]. These composites were produced by the ball milling mechanical alloying technique. The coating compositions made were copper-5CNT, copper-5CNT-10AlN, copper-10CNT-20AlN, and pure copper (Figure 13). The deposition efficiency reported was highest at around 0.2 for pure

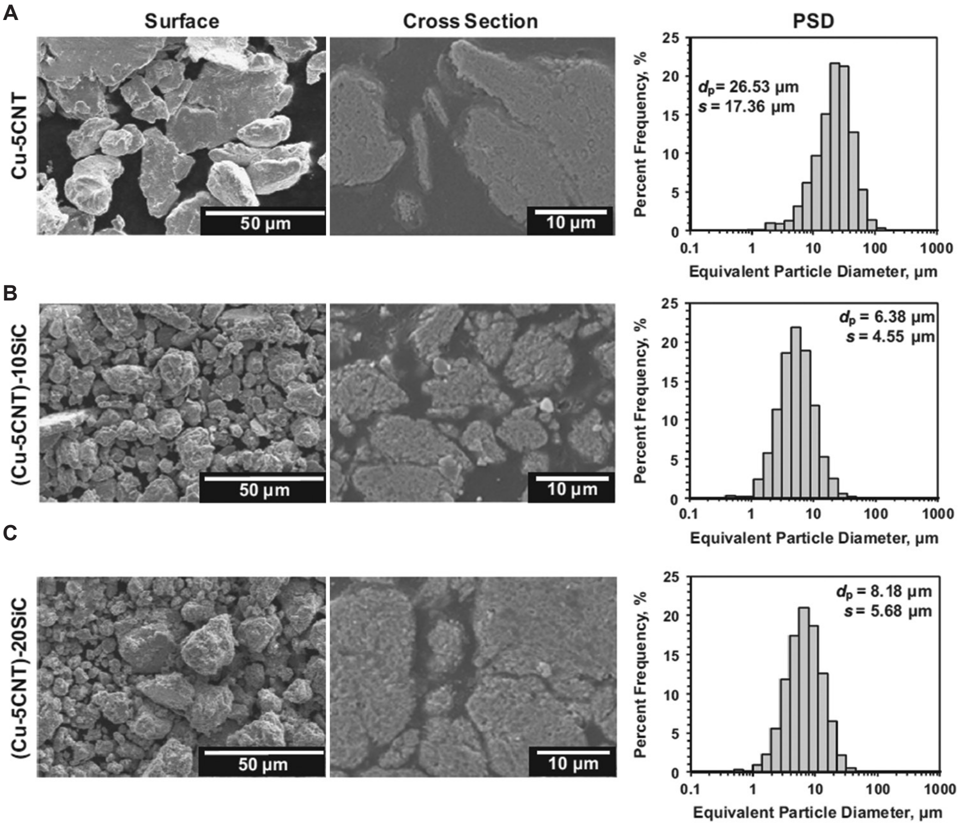

Figure 12. Scanning electron microscopy micrographs and powder size distributions of (A) Cu-5CNT, (B) Cu-5CNT-10SiC, and (C) Cu-5CNT-20SiC[45]. (Reprinted from *Ceramics International*, 41(5), Pialago, E. J. T., Kwon, O. K., and Park, C. W., Cold spray deposition of mechanically alloyed ternary Cu–CNT–SiC composite powders, 6764 – 6775, 2015, with permission from Elsevier).

copper coatings. The deposition efficiency decreased to 0.12 with the addition of CNT (copper 5CNT coatings). However, copper-5CNT-20AlN coatings had slightly better deposition efficiency than copper-5CNT-10AlN coatings. It was also reported that there were small pores in copper-5CNT-10AlN and copper-10CNT-20AlN that open toward the surface as compared to copper-5CNT coatings. Furthermore, copper-5CNT-10AlN coatings were rougher as well as porous than copper-5CNT-20AlN coatings. The pore volumes and surface roughness were the least for copper-5CNT-20AlN coatings compared to the copper-5CNT-10AlN and copper coatings.

4.3. Copper-silicon carbide cermet coatings

Winnicki *et al.*[30] manufactured and studied the corrosion resistance of copper-SiC coatings. In their work, after 18 cycles of salt spray test, the copper SiC coatings showed good corrosion resistance and the buckling of coatings was not so pronounced. As reported by the author, this could be because of the high amount of SiC particles in the coating creating a high amount of ceramic-metal interface, leading to the penetration of chloride ions in them. This effect was not so pronounced in Cu+Al_2O_3 coating work done by Winnicki *et al.* as mentioned above earlier. However, after 18 cycles of Kesternich test in a sulfur dioxide environment, the buckling of copper-SiC coatings was evident. As reported, the electrolyte having the sulfate ions was penetrating into the coating. Furthermore, it was claimed by the author that SiC might be serving as an inert electrode, facilitating the galvanic corrosion, resulting in the delamination of copper-SiC coatings, which is not the case with copper-alumina coatings. This lack of corrosion resistance also resulted in a decrease in the electrical conductivity of as-sprayed copper-SiC coatings. The reported electrical conductivity values were 49% IACS for as-sprayed copper-SiC coatings and around 20% IACS for both cases of corrosion tests (salt spray test and Kesternich test) for copper SiC coatings[30].

Recently, Chen *et al.*[47] cold-sprayed copper-SiC coatings along with pure copper, copper- Al_2O_3, and copper-WC coatings. The compositions made were pure copper, copper-alumina (15 wt.%), copper-SiC (15 wt.%), and copper-WC (15 wt.%). As reported, the density of SiC·Al_2O_3, WC were 3.2 g/cm^3, 3.5 g/cm^3, and 15.63 g/cm^3.

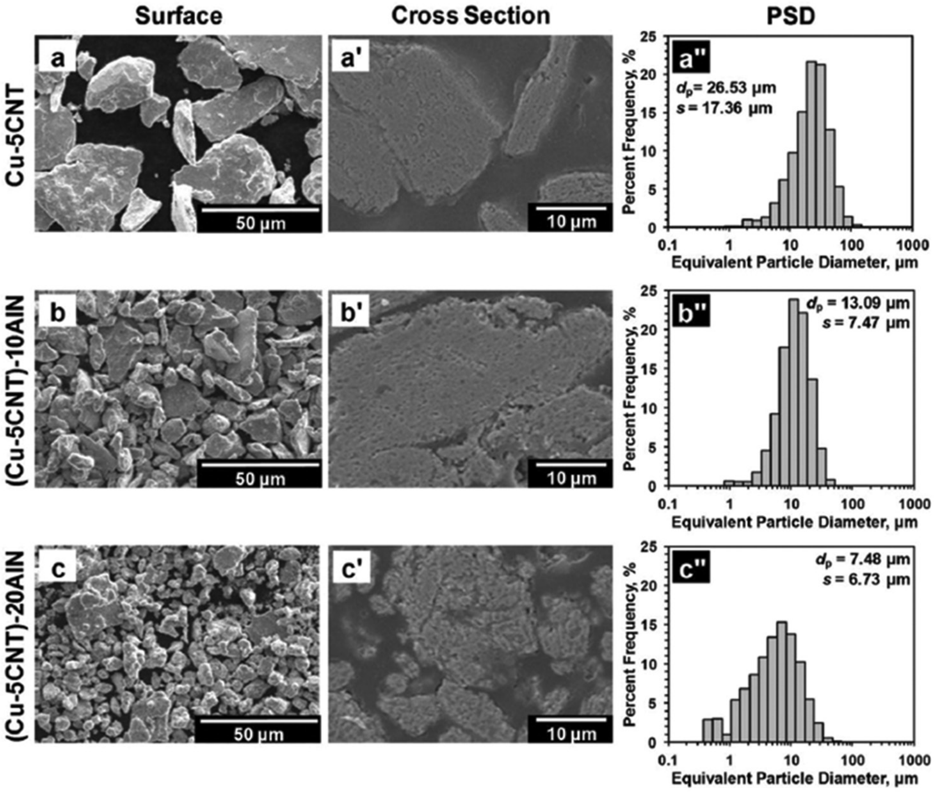

Figure 13. Scanning electron microscopy micrographs and powder size distributions of (A) Cu-5CNT, (B) Cu-5CNT-10AlN, and (C) Cu-5CNT-20AlN[46]. (Reprinted from *Journal of Alloys and Compounds*, 650, Pialago, E. J. T., Kwon, O. K., Kim, M.-S., and Park, C. W., Ternary Cu–CNT–AlN composite coatings consolidated by cold spray deposition of mechanically alloyed powders, 199 – 209, 2015, with permission from Elsevier).

Therefore, due to this density, the deposition of SiC and Al_2O_3 was good enough as compared to the tungsten carbide particles during the cold spray process. The ceramic content of copper-SiC and copper-Al_2O_3 coatings on an average reported was 7.5 + 3.2 vol.% and 10.5 + 2.7 vol.%, respectively. The wear rate of pure copper coatings was 289.57 × 10^{-6} mm^3/Nm and the reported wear rates for copper-SiC and copper-Al_2O_3 cold-sprayed coatings were 207.42 × 10^{-6} mm^3/Nm and 70.88 × 10^{-6} mm^3/Nm, respectively. The microhardness values reported for copper-SiC and copper-Al_2O_3 were 167.36 Hv and 165.01 Hv, which were higher as compared to the cold-sprayed copper coatings around 159.55 Hv. Again, the nanohardness values of copper-SiC and copper-Al_2O_3 coatings are 2.18 GPa and 2.28 GPa, respectively, which are higher than that of pure copper coatings around 2.06 GPa. Furthermore, according to Chen *et al.*, the wear mechanism of pure copper and copper-SiC coatings is adhesive in nature, whereas the copper-Al_2O_3 coatings have an abrasive wear mechanism due to the high bond strength between copper-alumina particles. Furthermore, the thermal conductivities of copper-SiC and copper-Al_2O_3 which were 164.388 W/m-K and 156.911 W/m-K, respectively, at 50°C increased to 209.407 W/m-K and 213.482 W/m-K after the heat treatment of these cold-sprayed coatings. Therefore, the merits of copper-alumina coatings seem to be better, but a thorough research on copper-SiC coatings might bring their characteristic properties into light and prove their commercial importance[47].

4.4. Copper-graphene coatings

Graphene is a wonder material, having excellent electrical conductivity, thermal conductivity, and mechanical strength[48,49]. Good quality graphene can be produced by chemical vapor deposition (CVD) method[50]. Graphene nanoplates (GNPs) are widely used in the production of metal matrix composites as they can be manufactured economically and in large quantities[51]. Yin *et al.*[52] produced GNP-reinforced copper matrix coatings intending to improve anti-friction performance. As reported, ball milling of copper and GNP powders was done; thus, copper-GNP (1 vol.%) powder feedstock was produced. The feedstock was then cold sprayed on an aluminum substrate. Then, a wear test was performed on pure copper cold spray coatings, cold-sprayed copper GNP (1 vol.%) coatings, and spark plasma sintered copper GNP coatings. Interestingly, the friction coefficient of cold-sprayed copper GNP (1 vol.%) coatings was 20% lesser than that of pure copper cold spray coatings. Furthermore, when compared to spark plasma sintered copper-based coatings, the cold-sprayed copper-GNP coatings performed better at the same volume percent of GNP in the copper matrix. The anti-friction performance was the optimum for copper-GNP cold-sprayed composite coatings. The worn surface of copper-GNP cold-sprayed coatings had very little debris and delamination. The GNPs existing at the worn surface were fractured during the wear test, which provided a graphene-rich film that lubricates the worn surface. Hence, the anti-friction performance is significantly improved[52].

In another work, Choi *et al.*[53] deposited graphene-copper cold spray coatings with copper powders and graphene grown on copper powders by CVD technique. As reported, the copper particles were coated with graphene through CVD process by introducing the powder copper particles to CH_4, H_2, and Ar gases at 100 Pa pressure for 30 min. The graphene-coated copper powder particles were then mixed with pure copper particles at a 1:3 ratio mixture, which was then cold sprayed onto an aluminum plate. The author claims to have created graphene copper composite cold spray coatings with minimal damage to graphene. The possibility of agglomeration due to high surface energy and Van der Waals forces of graphene could also be avoided by the CVD processing technique followed by cold spraying. The damage to graphene that happened during cold spray was evaluated by I_D/I_G ratio through Raman spectroscopy analysis. The I_D/I_G ratio for composite particles was 0.72, which became 0.62 after the cold spray process. This result shows that the damage to graphene was not significant. It is possible that the low temperature of carrier gas could have prevented thermal damage and oxidation of graphene. Furthermore, the band for the graphene also did not shift. It was at the same position 1588 cm^{-1} for both composite powders and coatings, indicating very low compressive residual stress induced during the cold spray process. The interatomic forces between graphene and copper particles due to the high electron density at the interface between copper and graphene prevented the pullout of graphene

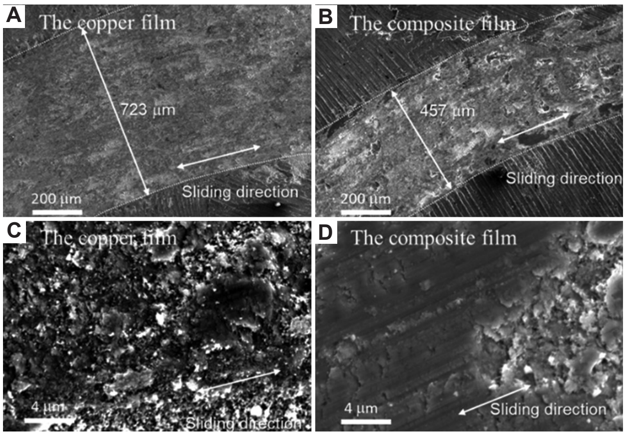

Figure 14. Scanning electron microscopy micrographs of sliding mark on the copper surface and composite film surface[53]. (Reprinted from *Diamond and Related Materials*, 116, Choi, J., Okimura, N., Yamada, T., Hirata, Y., Ohtake, N., and Akasaka, H., Deposition of graphene-copper composite film by cold spray from particles with graphene grown on copper particles, 108384, 2021, with permission from Elsevier).

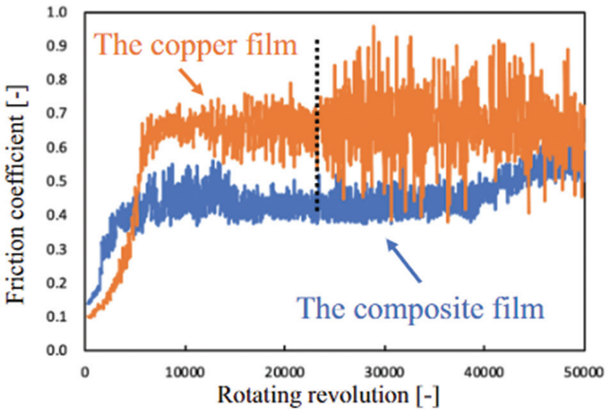

Figure 15. The measured coefficient of friction for copper and composite film[53]. (Reprinted from Diamond and Related Materials, 116, Choi, J., Okimura, N., Yamada, T., Hirata, Y., Ohtake, N., and Akasaka, H., Deposition of graphene-copper composite film by cold spray from particles with graphene grown on copper particles, 108384, 2021, with permission from Elsevier).

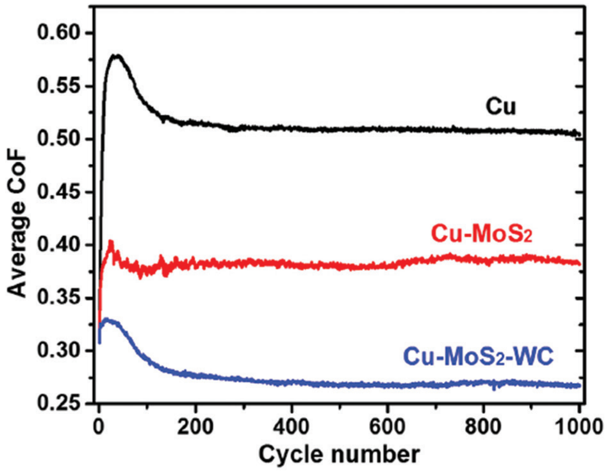

Figure 16. Coefficient of friction for copper, copper-MoS_2, and copper-MoS_2-WC[63]. (Reprinted from *Tribology International*, 123, Zhang, Y., Epshteyn, Y., and Chromik, R. R., Dry sliding wear behavior of cold-sprayed Cu-MoS2 and Cu-MoS2-WC composite coatings: The influence of WC, 296 – 306, 2018, with permission from Elsevier).

from copper particles by the Van der Waals forces, which became an advantage for cold spraying and enhanced wear resistance characteristics[53].

In Figure 14, worn areas of copper and its composite coatings are shown[53]. The graphene copper composite coatings had a better friction coefficient of 0.46, and copper coatings had a friction coefficient of 0.6, as shown in Figure 15. Furthermore, the wear rates for graphene copper composite coatings were 5.2×10^{-4} mm^3/Nm and that for pure copper coatings were 8.6×10^{-4} mm^3/Nm[53].

4.5. Copper-MoS$_2$ composite coatings

Metal matrix composites that have good wear resistance and self-lubricating properties can be used for making bearings[54]. In this material type, MoS$_2$ particles can play an effective role in reducing friction and wear rate[55]. The addition of ceramic particles into self-lubricating metal matrix composites is a good practice to ameliorate the wear resistance and strength of these composites[56-61]. Moreover, cold spray can be a beneficial method for spraying metal matrix composites powder feedstock containing MoS$_2$ because there could be no decomposition or phase transformations of solid lubricant MoS$_2$ as the cold spray process does not involve very high temperatures. Brittle compounds such as Cu$_2$S and CuMo$_2$S$_3$ may cause an increase in friction and wear, eliminating the purpose of solid lubricant when the Cu-MoS$_2$ composites are fabricated through sintering[62].

Zhang *et al.*[63] studied the sliding wear behavior of copper-MoS$_2$ and copper-MoS$_2$-WC cold spray coatings. As reported, the sliding wear experiment done showed that copper-MoS$_2$-WC coatings had low friction and wear rate compared to copper-MoS$_2$ coatings. The tungsten carbide particles helped reduce the friction; wear became uniform throughout the wear track, as shown in Figure 16. The tungsten carbide particles embedded in the coating had a thin layer of copper, which could be an advantage because the function of hard particles like tungsten carbide is not only to reduce friction but also to not serve as abrasives during wearing by having direct contact. In that work, the authors did not use a high volume percent of tungsten carbide in the coatings; probably, because tungsten carbide particles can compromise the bond strength. As far as copper-MoS$_2$ coatings were concerned, the MoS$_2$ particles smeared out during sliding and replenishing the particles continued with sliding. However, for copper-MoS$_2$-WC coatings, more wear debris accumulation due to WC particles suggests a low wear rate. There was an active transfer of material due to rapid wear debris removal in the case of copper-MoS$_2$ coatings. This led to detachments and cracks on copper-MoS$_2$ wear tracks, which was not observed in copper-MoS$_2$-WC wear track. Furthermore, the subsurface microstructures of copper-MoS$_2$-WC wear tracks suggested that the WC particles also served as load bearers and protected the rest of the surface from severe plastic deformation. The presence of the ultrafine grains only around the WC particles proved it. While for the copper-MoS$_2$ coatings, the ultrafine grains were present everywhere on the worn surface. The cracks on copper-MoS$_2$ wear tracks were again due to the already work hardened ultrafine grains present all over the surface of the wear track.

4.6. Copper-TiB$_2$ composite coatings

Copper-TiB$_2$ composite fabrication has received much attention due to its vivid applications that require properties such as electrical conductivity, thermal conductivity, wear

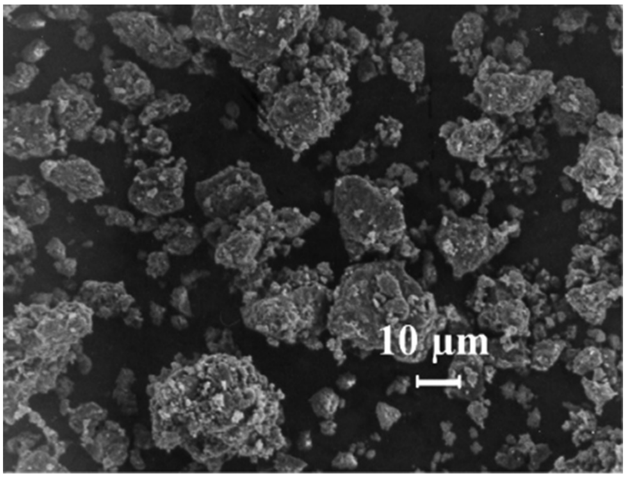

Figure 17. Copper-43 vol.% TiB$_2$ feedstock powders formed as product after the SHS reaction for cold spraying[70]. (Reprinted from *Composites Science and Technology*, 67(11), Kim, J. S., Kwon, Y. S., Lomovsky, O. I., Dudina, D. V., Kosarev, V. F., Klinkov, S. V., Kwon, D. H., and Smurov, I., Cold spraying of *in situ* produced TiB2–Cu nanocomposite powders, 2292 – 2296, 2007, with permission from Elsevier).

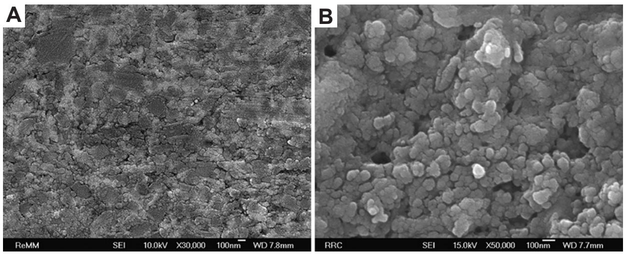

Figure 18. Microstructures of copper-43 vol.% TiB$_2$ cold spray coating: (A) Etched with $(NH_4)_2S_2O_8$ aqueous solution and (B) etched with FeCl$_3$ aqueous solution[70]. (Reprinted from *Composites Science and Technology*, 67(11), Kim, J. S., Kwon, Y. S., Lomovsky, O. I., Dudina, D. V., Kosarev, V. F., Klinkov, S. V., Kwon, D. H., and Smurov, I., Cold spraying of *in situ* produced TiB2–Cu nanocomposite powders, 2292 – 2296, 2007, with permission from Elsevier).

resistance, and strength[64-68]. Titanium diboride particles do not react with copper; it has a high melting point, high strength, resistance to wear, and hardness[69], which make them attractive for applications in the electrical industry[66,70].

In 2007, Kim *et al.*[70] were successful in spraying copper-43 vol.% TiB_2. As reported, titanium, boron, and copper nanocomposite powders were subjected to ball milling for 2 min and then subjected to self-propagating high-temperature synthesis reaction (SHS). Further, the product obtained after self-propagating high-temperature synthesis reaction was milled again to obtain optimum size TiB_2 particles, as shown in Figure 17. The heat of the SHS reaction got distributed evenly all around due to the good thermal conductivity of copper, which helped in the proper formation of TiB_2 particles. This powder feedstock was sprayed onto a copper substrate. The cold-sprayed coating was reported to be 70 µm in thickness. The coatings were very dense, possibly due to the huge plasticity difference between the copper and TiB_2 in these coatings. As reported, the coatings etched with $(NH_4)_2S_2O_8$ aqueous solution, as shown in Figure 18A, display the microstructure of the composite coating. The powder particles are closely packed in the coatings. Furthermore, in Figure 18B, the coatings etched with $FeCl_3$ solution are shown where the selective removal of copper from the surface leaves behind the network of TiB_2 phase. The Vickers hardness of copper-43 vol.% TiB_2 coating was reported to be 378 Hv which was much higher than that of the pure copper cold spray coatings, having a Vickers hardness of around 159.55 Hv as reported by Chen *et al.*[47]. The titanium diboride structure is responsible for the high hardness of copper-43 vol.% TiB_2 cold-sprayed coatings.

In another work, Calli *et al.*[71] produced cold-sprayed pure copper, copper-B_4C, copper-TiB_2, and copper-TiC coatings. As reported, the electrical conductivity of pure copper coatings was equivalent to that of the copper-TiB_2 (12.5 vol.%), around 36.0 MS/m, which is more than that of the copper-B_4C (12.5 vol.%) coatings and copper TiC (12.5 vol.%). This observation may be due to the electrical conductivity of the ceramic particles used. However, the relative wear rates (RWRs) were lowest for copper-TiB_2 coatings compared to copper-TiC and copper-B_4C coatings. This result could be due to the third

Table 1. Summary of cold spray deposition parameters for copper-based cold spray coatings

Powder	Composition	Particle diameter (µm)	Gas	Po	To	SoD (mm)	Q (g/min)	Substrate	Ref.
Copper	Pure copper	Cu (ACU 325)	N_2	2.8 MPa	500°C	35	32.1+1.14	Cu	[45]
Cu-Al_2O_3	Cu 90,70,50 Al2O3 10, 30, 50	25+5	Air	6 bar	540°C	10	-	Steel	[30]
Cu-Al_2O_3 – Cu coated graphite	Cu (90, 85, 80, and 70 wt.%), Al_2O_3 (10 wt.%), Cu coated graphite (0, 5, 10, and 20 wt.%)	Cu (20.18 µm), Al_2O_3 (4.41 µm), Cu coated graphite (47.77 µm)	Air	0.8 MPa	500°C	10	14 – 16	304SS	[31]
Cu-CNT	Cu 100, 95, 90, 85 CNT 0, 5, 10, 15	10 – 30	N_2	2.8 MPa	500°C	35	22.51 – 28.88	-	[44]
Cu-CNT-SiC	Cu (95 vol.%)-CNT (5 vol.%) SiC (10 and 20 vol.%)	Cu (ACU 325) CNT (5 – 20 nm) SiC (320 grit)	N_2	2.8 MPa	500°C	35	23.60 – 28.88	Cu	[45]
Cu-CNT-AlN	Cu (95 vol.%)-CNT (5 vol.%) AlN (10 and 20 vol.%)	Cu (ACU 325) CNT (5 – 20 nm) AlN (7 – 30 µm)	N_2	2.8 MPa	500°C	35	21.95 – 28.88	Cu	[46]
Cu- MwCNT	Cu (97 vol.%) MwCNT (3 vol.%)	0.5 – 3	Air	0.6 MPa	200°C	-	-	Al	[41]
Cu-graphene	Cu (99 vol.%) Graphene (1 vol.%)	Cu 15-38 µm Graphene 5 – 30 nm	He	2 MPa	25°C	40	-	Al	[52]
Cu-graphene	Pure copper powder coated with graphene	20	Air	0.6 MPa	720 K	12	8.21	Al	[53]
Cu-MoS_2	Cu 85 vol.%/MoS_2 (15 vol.%)	Cu (26 µm) MoS_2 (68 µm)	N_2	5 MPa	800°C	-	Cu (34.8) MoS_2 (3.6)	AA6061	[63]
Cu-MoS_2-WC	Cu 85 vol.%, MoS_2 (14 vol.%), WC (11 vol.%)	Cu (26 µm) MoS_2 (68 µm) WC (30 µm)	N_2	5 MPa	800°C	-	Cu+WC (39.4) MoS_2 (3.6)	AA6061	[63]

body abrasion mechanism, which happens due to the detachment of ceramic particles that break the oxide layer of metal during wear tests. The reported RWRs were 1.0, 2.7, 3.13, and 5.95 for pure copper, copper-TiB_2, copper B_4C, and copper TiC coatings, respectively. The coating thickness obtained for copper TiB_2 coatings was 1690 µm, which was much higher than that of pure copper (825 µm), copper B_4C (270 µm), and copper TiC (550 µm).

5. Cold spray deposition parameters and properties of copper-based cold spray coatings

Different reinforcements such as Al_2O_3, graphite, CNT, WC, MoS_2, and TiB_2 provide different properties to the copper-based cold spray coatings. These properties vary with the number of reinforcements employed, the morphology of powder particles, deposition conditions implemented, interface bonding characteristics, and characteristic properties of reinforcements. Table 1 shows the deposition parameters and compositions of the copper-based cold spray coatings and their substrates in the literature. The particle diameter generally preferred for copper-based cold spray coatings is between 10 µm and 50 µm to ensure good deposition efficiency. The low deposition temperatures also ensure that changes in the structural and mechanical properties are also minimized, and the purpose of the addition of ceramic particles is accomplished. The gases used for cold spray deposition have been helium, nitrogen, and air. Helium and nitrogen generally can help reduce oxidation. However, the authors who utilized air for cold spray deposition did not report any considerable oxidation of powder particles. The various substrates used for cold spray deposition in the references by different authors depend on various possible industrial applications of these coatings according to commercial acceptance. The applications of such copper-based cold spray coatings can be for seam and spot welding electrodes, conductors used for high-temperature applications, lead wires, electrical contacts, switches, etc.[29] Every material used as a reinforcement in the copper-based cold spray coatings serves its intended purpose.

In Table 2, a summary of the properties of various copper-based cold spray coatings with different reinforcements in the literature is presented. Numerous tests have been conducted by different authors to verify the effect of

Table 2. Comparison of various properties of copper-based cold spray coatings

Powder	Composition	Electrical conductivity	Friction coefficient	Wear rates	Microhardness	Ref.
Copper	Pure copper	36 MS/m	0.6	8.6×10^{-4}	140 – 160 Hv0.3	[23,53,71]
Cu-Al_2O_3	Cu (50 wt.%), Al_2O_3 (50 wt.%)	62% IACS	-	-	83 – 127 Hv0.3	[30]
Cu-Al_2O_3 – Cu coated graphite	Cu (90, 85, 80, and 70 wt.%), Al_2O_3 (10 wt.%) Cu-coated graphite (0, 5, 10, and 20 wt.%)	-	0.34 – 0.94	2.53×10^{-4} to 1.2×10^{-4}	114.3 – 88.2 Brinell hardness	[31]
Cu-CNT	Cu 100, 95, 90, 85 CNT 0, 5, 10, 15	-	-	-	160 – 230 Hv0.1	[45]
Cu-CNT-SiC	Cu (95 vol.%)-CNT (5 vol.%) SiC (10 and 20 vol.%)	-	-	-	190 – 260 Hv0.1	[45]
Cu- MwCNT	Cu (97 vol.%) MwCNT (3 vol.%)	-	-	-	303.64	[41]
Cu-graphene	Pure copper powder coated with graphene		0.46	5.2×10^{-4}		[53]
Cu-MoS_2	Cu 85 vol.%/MoS_2 (15 vol.%)	-	0.38 – 0.4	210×10^{-6} to 35×10^{-6}	75 – 132 Hv0.2	[63]
Cu-MoS_2-WC	Cu 85 vol.%, MoS_2 (14 vol.%), WC (11 vol.%)	-	0.27 – 0.33	123×10^{-6} to 19×10^{-6}	87 – 135 Hv0.2	[63]
Cu-TiB_2	Cu-12.5 vol% TiB_2	36 MS/m	-	Relative wear rate (with pure copper as 1) 2.7	156 Hv 0.025	[71]
Cu-B_4C	Cu-12.5 vol% TiB_2	34.3 MS/m	-	Relative wear rate (with pure copper as 1) 3.13	151 Hv 0.025	[71]
Cu-TiB_2	Cu-12.5 vol% TiB_2	35.6 MS/m	-	Relative wear rate (with pure copper as 1) 5.95	157 Hv 0.025	[71]

reinforcements in copper-based cold spray coatings. The electrical conductivity of pure copper and copper-based cold spray coatings considerably depends on the deposition parameters and porosity in the coatings. In general, higher porosity leads to lower electrical conductivity. The addition of reinforcements may or may not contribute to the increase in electrical conductivity, possibly due to the ineffectiveness of deposition, effective deformation of copper matrix, the amount of reinforcement used, and characteristic property of the reinforcements. Another property with commercial importance is the friction coefficient and wear rate. The addition of reinforcements such as graphite and MoS_2 imparts good lubrication properties, which decreases the friction coefficient and wear rates of the copper-based cold spray coatings. However, in such coatings, there could be a decrease in hardness values, possibly due to the weak interface bonding between metal matrix and reinforcement. Furthermore, this decrease in microhardness trend was not visible for reinforcements specifically used to improve the strength and hardness of copper-based cold spray coatings.

6. Conclusions and scope for future work

Pure copper and copper-based cold spray coatings are an interesting area of research in power industries. Copper-based cold spray coatings can enhance electrical and thermal conductivity, wear, and corrosion resistance, along with proper hardness and strength of components. The deposition parameters required for the cold spray of the copper-based coatings discussed in this work mainly consist of the gases used for cold spray, the pressure of the gas, standoff distance, and powder feedstock preparation for cold spraying by milling process with the incorporation of surfactants. Surfactants play a huge role in powder preparation, according to the size range required for cold spraying process. The mechanical milling process is an effective method to produce powder feedstock with homogeneity. The homogeneous distribution of reinforcement particles in the metallic copper matrix provides uniform mechanical and tribological properties.

Numerous research works focused on different types of reinforcements in copper-based cold spray coatings have been done. These different reinforcements provide unique properties to the copper-based coating according to their characteristics. The deformation and recrystallization of copper grains in pure copper coatings have been focused on in this work, along with the variation in properties with different amounts of reinforcements have also been discussed. These reinforcements have also been responsible for increasing the deposition efficiency and significant reduction in porosity. The copper-based cold spray coatings have shown superior qualities in terms of wear resistance, lesser oxidation, hardness, electrical conductivity, and so on when compared to other coating processes. The cold-sprayed copper coatings also retained the inherent characteristic properties of reinforcements without causing much damage to the reinforcements. This could be because of the low operating temperatures of the cold spray process that avoids any kind of melting or oxidation.

Copper-based cold spray coatings have immense scope for the future research works. The correct type and amount of reinforcements that can give the best desirable properties for copper-based coatings must be explored. The deposition efficiency of these copper-based coatings with the help of powder architecture and powder morphology is yet to be investigated thoroughly. The higher the deposition efficiency, the lesser wastage of powder feedstock used for the cold spraying process. Recycling of process gases and feedstock powder from economic and environmental point of view is important, and research on it is inevitable. The research works must include the incorporation of two reinforcements in the metal matrix that can provide enhanced mechanical and tribological properties. The electrical and thermal properties of copper-based cermets according to the various reinforcements used are a matter of further investigation, and this can be compared with the other coating processes such as HVOF, CVD, sintering, and so on. The comparisons can also be made among the various copper-based cold-sprayed coatings with several types of reinforcements. A thorough investigation of preserving the original grain sizes desired phases, and the chemistry of materials is desirable. The research works on bond strength and bonding characteristics, fatigue strength, thermal shock resistance, oxidation, and corrosion resistance of copper-based cold spray coatings can be beneficial in creating worthwhile coatings having great commercial importance.

Acknowledgments

The authors acknowledge with gratitude funding received from the Natural Sciences and Engineering Research Council of Canada (NSERC), the Canada Foundation for Innovation (CFI), Transport Canada, and the New Brunswick Innovation Foundation (NBIF).

Funding

This work is funded by the NSERC, the CFI, Transport Canada, and the NBIF.

Conflict of interest

The authors have no conflicts of interest to declare that are relevant to the content of this article.

Author contributions

Conceptualization: Vineeth Menon, Clodualdo Aranas Jr., and Gobinda Saha
Data curation: Vineeth Menon
Funding acquisition: Clodualdo Aranas Jr. and Gobinda Saha
Supervision: Clodualdo Aranas Jr. and Gobinda Saha
Writing – original draft: Vineeth Menon
Writing – review and editing: Clodualdo Aranas Jr. and Gobinda Saha.

References

1. Alkhimov AP, Papyrin AN, Kosarev VF, *et al.*, 1994, Gas-dynamic spraying method for applying a coating (United States Patent No. US5302414A). Available from: https://patents.google.com/patent/US5302414A/en [Last accessed on 2022 May 31].
2. Tokarev AO, 1996, Structure of aluminum powder coatings prepared by cold gasdynamic spraying. *Metal Sci Heat Treat*, 38: 136–139. https://doi.org/10.1007/BF01401446
3. Sripada J, Gallant M, Saha G, 2019, Study on the effect of milling parameters on HE-MA nanostructured Al-graphene cermet particles. *Proceedings of 1st Coatings and Interfaces Web Conference, 2019*, 6160. https://doi.org/10.3390/ciwc2019-06160
4. McCune RC, Donlon WT, Popoola OO, *et al.*, 2000, Characterization of copper layers produced by cold gas-dynamic spraying. *J Therm Spray Technol*, 9: 73–82. https://doi.org/10.1361/105996300770350087
5. Woo DJ, Heer FC, Brewer LN, *et al.*, 2015, Synthesis of nanodiamond-reinforced aluminum metal matrix composites using cold-spray deposition. *Carbon*, 86: 15–25. https://doi.org/10.1016/j.carbon.2015.01.010
6. Popovich A, Sufiiarov V, 2016. Metal powder additive manufacturing. In: Shishkovsky IV, editor. New Trends in 3D Printing. InTech, London. https://doi.org/10.5772/63337
7. Raoelison RN, Xie Y, Sapanathan T, *et al.*, 2018, Cold gas dynamic spray technology: A comprehensive review of processing conditions for various technological developments till to date. *Addit Manuf*, 19: 134–159. https://doi.org/10.1016/j.addma.2017.07.001
8. Stoltenhoff T, Kreye H, Richter HJ, 2002, An analysis of the cold spray process and its coatings. *J Therm Spray Technol*, 11: 542–550. https://doi.org/10.1361/105996302770348682
9. Suryanarayana C, 2001, Mechanical alloying and milling. *Prog Mater Sci*, 46: 1–184. https://doi.org/10.1016/S0079-6425(99)00010-9
10. Zhang DL, 2004, Processing of advanced materials using high-energy mechanical milling. *Prog Mater Sci*, 3–4: 537–560. https://doi.org/10.1016/S0079-6425(03)00034-3
11. Sripada JV, Saha DC, Saha GC, *et al.*, 2021, Study the effect of milling parameters on HE-MA nanostructured Al6061-graphene cermet feedstock particles. *J Alloys Comp*, 859: 157759. https://doi.org/10.1016/j.jallcom.2020.157759
12. Hu Z, Chen F, Xu J, *et al.*, 2018, 3D printing graphene-aluminum nanocomposites. *J Alloys Comp*, 746: 269–276. https://doi.org/10.1016/j.jallcom.2018.02.272
13. Toozandehjani M, Matori KA, Ostovan F, *et al.*, 2017, Effect of milling time on the microstructure, physical and mechanical properties of Al-Al_2O_3 nanocomposite synthesized by ball milling and powder metallurgy. *Materials*, 10: 1232. https://doi.org/10.3390/ma10111232
14. Nouri A, Wen C, 2014, Surfactants in mechanical alloying/milling: A catch-22 situation. *Crit Rev Solid State Mater Sci*, 39: 81–108. https://doi.org/10.1080/10408436.2013.808985
15. Kollo L, Leparoux M, Bradbury CR, *et al.*, 2010, Investigation of planetary milling for nano-silicon carbide reinforced aluminium metal matrix composites. *J Alloys Comp*, 489: 394–400. https://doi.org/10.1016/j.jallcom.2009.09.128
16. Lu L, Zhang YF, 1999, Influence of process control agent on interdiffusion between Al and Mg during mechanical alloying. *J Alloys Comp*, 290: 279–283. https://doi.org/10.1016/S0925-8388(99)00221-2
17. Shaw L, Villegas J, Luo H, *et al.*, 2003, Effects of process-control agents on mechanical alloying of nanostructured aluminum alloys. *Metallurgical Mater Trans A Phys Metallurgy Mater Sci*, 34: 159–170. https://doi.org/10.1007/s11661-003-0217-7
18. Legoux JG, Irissou E, Desaulniers S, *et al.*, n.d., Characterization and Performance Evaluation of a Helium Recovery System Designed for Cold Spraying. National Research Council Canada, Canada.
19. Cao K, Yu M, Liang CM, *et al.*, 2020, Study on thermal conductivity of cold sprayed Cu coating. *Surface Eng*, 36: 1058–1066. https://doi.org/10.1080/02670844.2020.1790170
20. Yin S, Xie Y, Cizek J, *et al.*, 2017, Advanced diamond-reinforced metal matrix composites via cold spray: Properties and deposition mechanism. *Compos B Eng*, 113: 44–54. https://doi.org/10.1016/j.compositesb.2017.01.009

21. Imbriglio SI, Chromik RR., 2021, Factors affecting adhesion in metal/ceramic interfaces created by cold spray. *J Therm Spray Technol*, 30: 1703–1723.

    https://doi.org/10.1007/s11666-021-01229-4

22. Pathak S, Saha GC., 2017, Development of sustainable cold spray coatings and 3D additive manufacturing components for repair/manufacturing applications: A critical review. *Coatings*, 7: 122.

    https://doi.org/10.3390/coatings7080122

23. Fukumoto M, Wada H, Tanabe K, *et al*., 2007, Effect of substrate temperature on deposition behavior of copper particles on substrate surfaces in the cold spray process. *J Therm Spray Technol*, 16: 643–650.

    https://doi.org/10.1007/s11666-007-9121-9

24. Borchers C, Stoltenhoff T, Gärtner F, *et al*., 2001, Deformation microstructure of cold gas sprayed coatings. *Mater Res Soc Symp Proc*, 674: P7.10.1–P.10.6.

    https://doi.org/10.1557/proc-673-p7.10

25. Assadi H, Kreye H, Gärtner F, *et al*., 2016, Cold spraying a materials perspective. *Acta Materi*, 116: 382–407.

    https://doi.org/10.1016/j.actamat.2016.06.034

26. Moridi A, Hassani-Gangaraj SM, Guagliano M, *et al*., 2014, Cold spray coating: Review of material systems and future perspectives. *Surface Eng*, 30: 369–395.

    https://doi.org/10.1179/1743294414Y.0000000270

27. Winnicki M, Małachowska A, Piwowarczyk T, *et al*., 2016, The bond strength of Al + Al_2O_3 cermet coatings deposited by low-pressure cold spraying. *Arch Civil Mech Eng*, 16: 743–752.

    https://doi.org/10.1016/j.acme.2016.04.014

28. Koivuluoto H, Vuoristo P, 2010, Effect of powder type and composition on structure and mechanical properties of Cu + Al_2O_3 coatings prepared by using low-pressure cold spray process. *J Therm Spray Technol*, 19: 1081–1092.

    https://doi.org/10.1007/s11666-010-9491-2

29. Phani PS, Vishnukanthan V, Sundararajan G, 2007, Effect of heat treatment on properties of cold sprayed nanocrystalline copper alumina coatings. *Acta Mater*, 55: 4741–4751.

    https://doi.org/10.1016/j.actamat.2007.04.044

30. Winnicki M, Baszczuk A, Jasiorski M, *et al*., 2017, Corrosion resistance of copper coatings deposited by cold spraying. *J Therm Spray Technol*, 26: 1935–1946.

    https://doi.org/10.1007/s11666-017-0646-2

31. Chen W, Yu Y, Cheng J, *et al*., 2018, Microstructure, mechanical properties and dry sliding wear behavior of Cu-Al_2O_3-graphite solid-lubricating coatings deposited by low-pressure cold spraying. *J Therm Spray Technol*, 27: 1652–1663.

    https://doi.org/10.1007/s11666-018-0773-4

32. Zhan GD, Kuntz JD, Wan J, *et al*., 2003, Single-wall carbon nanotubes as attractive toughening agents in alumina-based nanocomposites. *Nat Mater*, 2: 38–42.

    https://doi.org/10.1038/nmat793

33. Coleman JN, Khan U, Blau WJ, *et al*., 2006, Small but strong: A review of the mechanical properties of carbon nanotube-polymer composites. *Carbon*, 44: 1624–1652.

    https://doi.org/10.1016/j.carbon.2006.02.038

34. Ajayan PM, Tour JM, 2007, Nanotube composites. *Nature*, 447: 1066–1068.

    https://doi.org/10.1038/4471066a

35. Kwon H, Estili M, Takagi K, *et al*., 2009, Combination of hot extrusion and spark plasma sintering for producing carbon nanotube reinforced aluminum matrix composites. *Carbon*, 47: 570–577.

    https://doi.org/10.1016/j.carbon.2008.10.041

36. Cha SI, Kim KT, Arshad SN, *et al*., 2005, Extraordinary strengthening effect of carbon nanotubes in metal-matrix nanocomposites processed by molecular-level mixing. *Adv Mater*, 17: 1377–1381.

    https://doi.org/10.1002/adma.200401933

37. Bakshi SR, Lahiri D, Agarwal A, 2010, Carbon nanotube reinforced metal matrix composites a review. *Int Mater Rev*, 55: 41–64.

    https://doi.org/10.1179/095066009X12572530170543

38. Shukla AK, Nayan N, Murty SV, *et al*., 2013, Processing of copper-carbon nanotube composites by vacuum hot pressing technique. *Mater Sci Eng A*, 560: 365–371.

    https://doi.org/10.1016/j.msea.2012.09.080

39. Kang K, Bae G, Won J, *et al*., 2012, Mechanical property enhancement of kinetic sprayed Al coatings reinforced by multi-walled carbon nanotubes. *Acta Mater*, 60: 5031–5039.

    https://doi.org/10.1016/j.actamat.2012.05.034

40. Xie X, Chen C, Ji G, *et al*., 2019, A novel approach for fabricating a CNT/AlSi composite with the self-aligned nacre-like architecture by cold spraying. *Nano Mater Sci*, 1: 137–141.

    https://doi.org/10.1016/j.nanoms.2019.04.002

41. Cho S, Takagi K, Kwon H, *et al*., 2012, Multi-walled carbon nanotube-reinforced copper nanocomposite coating fabricated by low-pressure cold spray process. *Surf Coat Technol*, 206: 3488–3494.

    https://doi.org/10.1016/j.surfcoat.2012.02.021

42. Kim P, Shi L, Majumdar A, *et al*., 2001, Thermal transport measurements of individual multiwalled nanotubes. *Phys Rev Lett*, 87: 215502.

    https://doi.org/10.1103/PhysRevLett.87.215502

43. Cho S, Kikuchi K, Miyazaki T, *et al.*, 2010, Multiwalled carbon nanotubes as a contributing reinforcement phase for the improvement of thermal conductivity in copper matrix composites. *Sci Mater*, 63: 375–378.

https://doi.org/10.1016/j.scriptamat.2010.04.024

44. Pialago EJ, Park C. Cold spray deposition characteristics of mechanically alloyed Cu-CNT composite powders. *Appl Surf Sci*, 308: 63–74.

https://doi.org/10.1016/J.APSUSC.2014.04.096

45. Pialago EJ, Kwon OK, Park CW, 2015, Cold spray deposition of mechanically alloyed ternary Cu-CNT-SiC composite powders. *Ceram Int*, 41: 6764–6775.

https://doi.org/10.1016/j.ceramint.2015.01.123

46. Pialago EJ, Kwon OK, Kim MS, *et al.*, 2015, Ternary Cu-CNT-AlN composite coatings consolidated by cold spray deposition of mechanically alloyed powders. *J Alloys Comp*, 650: 199–209.

https://doi.org/10.1016/j.jallcom.2015.08.007

47. Chen Q, Yu M, Cao K, *et al.*, 2022, Thermal conductivity and wear resistance of cold sprayed Cu-ceramic phase composite coating. *Surf Coat Technol*, 434: 128135.

https://doi.org/10.1016/j.surfcoat.2022.128135

48. Novoselov KS, Geim AK, Morozov SV, *et al.*, 2004, Electric field effect in atomically thin carbon films. *Science*, 306: 666–669.

https://doi.org/10.1126/science.1102896

49. Warner JH, Schaffel F, Rummeli M, *et al.*, 2012, Graphene: Fundamentals and Emergent Applications. Elsevier, Amsterdam, Netherlands, p61-125.

50. Reina A, Jia X, Ho J, *et al.*, 2009, Large area, few-layer graphene films on arbitrary substrates by chemical vapor deposition. *Nano Lett*, 9: 30–35.

https://doi.org/10.1021/nl801827v

51. Kotov NA, 2006, Carbon sheet solutions. *Nature*, 442: 254–255.

https://doi.org/10.1038/442254a

52. Yin S, Zhang Z, Ekoi EJ, *et al.*, 2017, Novel cold spray for fabricating graphene-reinforced metal matrix composites. *Mater Lett*, 196: 172–175.

https://doi.org/10.1016/j.matlet.2017.03.018

53. Choi J, Okimura N, Yamada T, *et al.*, 2021, Deposition of graphene-copper composite film by cold spray from particles with graphene grown on copper particles. *Diam Relat Mater*, 116: 108384.

https://doi.org/10.1016/j.diamond.2021.108384

54. Chromik R, Alidokht S, Shockley JM, *et al.*, 2018, Tribological coatings prepared by cold spray. In: Cold-Spray Coatings. Springer, Berlin, p321–348.

https://doi.org/10.1007/978-3-319-67183-3_11

55. Wu Y, Wang F, Cheng Y, *et al.*, 1997, A study of the optimization mechanism of solid lubricant concentration in $NiMoS_2$ self-lubricating composite. *Wear*, 205: 64–70.

https://doi.org/10.1016/S0043-1648(96)07299-7

56. Miracle DB, 2005, Metal matrix composites from science to technological significance. *Comp Sci Technol*, 65: 2526–2540.

https://doi.org/10.1016/j.compscitech.2005.05.027

57. Suresha S, Sridhara BK, 2010b, Wear characteristics of hybrid aluminium matrix composites reinforced with graphite and silicon carbide particulates. *Comp Sci Technol*, 70: 1652–1659.

https://doi.org/10.1016/j.compscitech.2010.06.013

58. Narayanasamy P, Selvakumar N, Balasundar P, 2015, Effect of hybridizing MoS_2 on the tribological behaviour of Mg-TiC composites. *Trans Indian Inst Metals*, 68:911–925.

https://doi.org/10.1007/s12666-015-0530-z

59. Xu J, Liu W, Zhong M, 2006, Microstructure and dry sliding wear behavior of MoS_2/TiC/Ni composite coatings prepared by laser cladding. *Surf Coat Technol*, 200: 4227–4232.

https://doi.org/10.1016/j.surfcoat.2005.01.036

60. Rajkumar K, Aravindan S, 2011, Tribological performance of microwave sintered copper-TiC-graphite hybrid composites. *Tribol Int*, 44: 347–358.

https://doi.org/10.1016/j.triboint.2010.11.008

61. Suresha S, Sridhara BK, 2010a, Effect of addition of graphite particulates on the wear behaviour in aluminium-silicon carbide-graphite composites. *Mater Des*, 31: 1804–1812.

https://doi.org/10.1016/j.matdes.2009.11.015

62. Kato H, Takama M, Iwai Y, *et al.*, 2003, Wear and mechanical properties of sintered copper-tin composites containing graphite or molybdenum disulfide. *Wear*, 225: 573–578.

https://doi.org/10.1016/S0043-1648(03)00072-3

63. Zhang Y, Epshteyn Y, Chromik RR, 2018, Dry sliding wear behaviour of cold-sprayed Cu-MoS_2 and Cu-MoS_2-WC composite coatings: The influence of WC. *Tribol Int*, 123: 296–306.

https://doi.org/10.1016/j.triboint.2017.12.015

64. Tu J, Rong W, Guo S, *et al.*, 2003, Dry sliding wear behavior of *in situ* Cu-TiB_2 nanocomposites against medium carbon steel. *Wear*, 255: 832–835.

https://doi.org/10.1016/S0043-1648(03)00115-7

65. Valero ML, Corredor D, Camurri C, *et al.*, 2005, Performance and characterization of dispersion strengthened Cu-TiB_2 composite for electrical use. *Mater Characterization*, 55: 252–262.

https://doi.org/10.1016/j.matchar.2005.04.006

66. Kim JS, Kwon YS, Dudina DV, *et al.*, 2005, Nanocomposites

TiB2-Cu: Consolidation and erosion behavior. *J Mater Sci*, 40: 3491–3495.

https://doi.org/10.1007/s10853-005-2854-2

67. Agarwal A, Dahotre NB, Sudarshan TS, 1999, Evolution of interface in pulsed electrode deposited titanium diboride on copper and steel. *Surf Eng*, 15: 27–32.

    https://doi.org/10.1179/026708499322911601

68. Tu J, Wang NY, Yang YZ, *et al*., 2002, Preparation and properties of TiB_2 nanoparticle reinforced copper matrix composites by *in situ* processing. *Mater Lett*, 52: 448–452.

    https://doi.org/10.1016/S0167-577X(01)00442-6

69. Munro RG, 2000, Material properties of titanium diboride. *J Res Natl Inst Stand Technol*, 105: 709.

    https://doi.org/10.6028/jres.105.057

70. Kim JS, Kwon YS, Lomovsky OI, *et al*., 2007, Cold spraying of *in situ* produced TiB_2-Cu nanocomposite powders. *Comp Sci Technol*, 67: 2292–2296.

    https://doi.org/10.1016/j.compscitech.2007.01.019

71. Calli C, Tazegul O, Kayali ES, 2017, Wear and corrosion characteristics of copper-based composite coatings. *Ind Lubr Tribol*, 69: 300–305.

    https://doi.org/10.1108/ILT-07-2016-0146

Author Guidelines

Before submitting for publication, please ensure that your paper and other supplementary files have been prepared and formatted in accordance with the guidelines below.

Submission structure, general style and format

Materials Science in Additive Manufacturing requests that every new submission should be made and accompanied by 3 separate core files, namely manuscript, title page and back matter, and cover letter, whereas resubmission of revision file should be accompanied by 4 separate core files, namely manuscript, title page and back matter, cover letter, and response/rebuttal letter (collectively known as the revision file). Provision of supplementary files and/or confidential accessory files is optional or dependent on the nature of study and findings relevance. The table below briefly summarizes the type of files in a submission, their respective requirements and included items:

Type of file	File format	Requirements	Included items
(1) Manuscript	DOC or DOCX	- Use 1.5-spacing and format text in one column - Use page numbers and continuous line numbers - Font and size: Times New Roman, 12 - Insert tables and figures at the back of manuscript	- Manuscript title - Abstract (for original research article, review article and perspective article) - Keywords - Text - References - Tables (including caption and legend) - Figures (including caption and legend)
(2) Title page and back matter *	DOC or DOCX	- Use 1.5-spacing and format text in one column - Font and size: Times New Roman, 12	**On the first page (title page):** - Manuscript title - Authorship list (first and last names must be spelled out) - Author's affiliation, including department, institution, city, state, postal code, and country (indicated with superscript number) - Corresponding author information, including asterisk indication, mailing address and email - Indication of equally contributing authors (if any) with dagger symbol **On the second page (back matter):** - Acknowledgments - Funding - Conflict of interest (mandatory) - Author contributions (formatted as per CRediT) - Further disclosure about presentation of essential findings in conference(s) and/or upload of the paper to a preprint server
(3) Cover letter	DOC or DOCX	- Use 1.5-spacing and format text in one column - Font and size: Times New Roman, 12	- A brief explanation of what was previously known, the conceptual advancement with the findings and its significance to broad readership - A statement that "neither the manuscript nor any significant part of it is under consideration for publication elsewhere or has appeared elsewhere in a manner that could be construed as a prior or duplication of the same work" with author confirmation - If any, associated accession numbers or DOIs of the corresponding preprint version of the submission - [Optional] Name, affiliation and email address of up to 4 academically qualified (recommended) reviewers and/or name and affiliation of individuals who should be excluded from reviewing the submitted works on the grounds of conflict of interest
(4) Supplementary files		- Supplementary files should **not exceed 20 MB** in total (15MB individual file limit)	

- Supplementary tables or figures	DOC or DOCX	- Use 1.5-spacing and format text in one column - Use page numbers and continuous line numbers - Font and size: Times New Roman, 12 - Include both supplementary tables (editable) and figures (in JPEG, PNG or TIFF format) in the same file	- Supplementary tables - Supplementary figures
- Data set	XLS or XLSX	- All data should be neatly presented using consistent fonts	
- Videos	MP4	- If necessary, trim the video clip to focus only on essential parts, such as experimental procedures and findings or observation that can only be demonstrated using video(s) - Avoid unnecessary narrations that can be presented in written form	
(5) Confidential accessory files			
- Sample consent form (for human research only)	DOC, DOCX, PDF, JPEG, PNG or TIFF	- This is a sample, unsigned consent form that should bear the institution letterhead	
- Research ethics proof (for human and/or animal research only)	DOC, DOCX, PDF, JPEG, PNG or TIFF	- Ideally, this document should contain the essential research ethics information, such as ethics approval identifiers and the name of Institutional Ethics Review Board or Institutional Review Board - The research described in **original research article** should match the proposed research or significantly fit within the framework of the specification stipulated in the research ethics proof	
(6) Response/rebuttal letter (only applicable to revisions)	DOC or DOCX	- All comments/feedback and responses/rebuttals must be clearly and concisely presented	- Reviewers' comments and feedback - Authors' responses

[#] Ideally, all information given in the title page and back matter file, except for the manuscript title, should remain the same from the point of submission to paper acceptance. Thus, authors are responsible to ensure that all information therein is accurate before making submission. Refer to **Authorship and Author Information** for more information about *Materials Science in Additive Manufacturing*'s authorship policy.

Submitting authors should refer to the relevant sections in the following for more detailed information.

Author metadata during submission

During the submission process, the submitting author must ensure that all particulars of author information, including full name, affiliation, and email address, are given in the author metadata column of the submission system. These particulars must exactly reflect those on the title page of the submission; this includes the author order of the authorship list. Provide authors' ORCID ID, if available.

Article types

(1) Original research article

An original research article is based on original, basic and applied research and/or analysis. This type of article aims to describe significant and novel research. Authors of original research articles must confirm that the essential findings presented have never been published or under consideration elsewhere.

This article type typically has at least 5 tables and/or figures in total, approximately 40 references, and 7,000 words (inclusive of Abstract and References).

(2) Review article

A review article provides scholarly survey as well as balanced summarization and highlights of recent developments in a research field or emerging/future trends. Authors should ensure that all perspectives from different works are linked in balanced and cohesive manner, taking into consideration different schools of thought.

This article type typically has at least 5 tables and/or figures in total, approximately 70 references, and 7,000 words (inclusive of Abstract and References).

(3) Perspective article

A perspective article contains the author's scholarly opinions on a particular subject area or topic. Unlike a review, a perspective article covers a more specific part of the field, aiming to provide new insights into the subject matter. However, these perspectives or opinions should be objective in line with the spirit of academia. A good perspective piece should stimulate further discussions and initiate novel experiments.

This article type typically has 5 tables and/or figures in total, approximately 70 references, and 7,000 words (inclusive of Abstract and References).

(4) Letters

This article type is a collection of unsolicited letters from the readers who wish to comment on specific articles published in *Materials Science in Additive Manufacturing* or another field-related journal. Alternatively, a letter can be written on an unrelated topic of interest to the journal's readership.

Ideally, a letter should present an in-depth, scholarly re-analysis of a previously published article in *Materials Science in Additive Manufacturing* or in another field-related journal, accompanied by the reader's constructive insights and comments. Letters containing new ideas, supporting data or data criticizing the indicated article may be subjected to peer review at editors' discretion. Authors should specify the intended recipient of the letters, i.e., Editor or specific author(s).

This article type typically has no more than 3 tables and/or figures in total, no more than 20 references, and 2,000 words (inclusive of References). No Abstract is required.

(5) Editorial

An editorial piece is a solicited, concise commentary that highlights prominent topics in particular issue. Alternatively, an editorial represents the official opinions of the editors on the journal or special issue.

An editorial piece should not exceed 1,000 words (inclusive of References). Typically, an Abstract is not required and only 1 figure or table is allowed.

(6) Erratum

Authors should contact the editors of *Materials Science in Additive Manufacturing* (editor.msam@whioce.com) if certain errors made by the journal are found. The editors will evaluate the impact of the errors and decide on the appropriate course of action. Any corrections to a paper are published at the sole discretion of the editors.

(7) Corrigendum

Authors should contact the editors of *Materials Science in Additive Manufacturing* (editor.msam@whioce.com) if certain errors made by the authors are found. The editors will evaluate the impact of the errors and decide on the appropriate course of action. Any corrections to a paper are published at the sole discretion of the editors.

Language

All submissions must be written entirely in good American English. Spelling and use of punctuations should conform to conventions in American English. Clarity and conciseness are critical requirements for publications; therefore, submissions that are not clearly written will be returned to authors. Authors must ensure that their manuscripts are submit-ready or publish-ready before making submission. The articles published in *Materials Science in Additive Manufacturing* are in adherence with the publishable standards of academic and scientific writing.

Please note that utilizing a language editing service is not a guarantee of acceptance.

Letter capitalization

Use sentence case capitalization in all aspects of the submission. In sentence case, most major and minor words are lowercase (proper nouns, including name of organizations and name of guidelines, are an exception in that they are always capitalized for the first letter of each word, except for minor words, such as conjunctions and short prepositions). The first letter of the first word should always be uppercase.

Manuscript title

The title should capture the conceptual significance for a broad audience. The title should not be more than 50 words and should be able to give readers an overall view of the paper's significance. Titles should avoid using uncommon jargons, abbreviations and punctuation.

Abstract

The purpose of abstract is to provide sufficient information and capture essential findings and/or messages of the paper. The length of an abstract should be in the range of 200-400 words. The abstract should be **unstructured**. Abstract is only needed in original research article, review article, and perspective article.

Keywords

Each submission should be accompanied by 3-6 keywords. Avoid using abbreviations and acronyms in keywords, unless they are established standard keywords. Separate keywords with semi-colons (i.e, term1; term2; term3).

Abbreviations and acronyms

Define abbreviations and acronyms upon their first appearance, **separately**, in the abstract, main text, table legends, and figure captions and legends.

Sections in article

(1) Section headings

Section headings should be in boldface. Examples of section headings of different levels are shown in the following:

Primary level : **1. Heart disease**

Secondary level : **1.3. Risk factors for heart disease**

Tertiary level : **1.3.2. Hypertension**

Authors are suggested **NOT** to introduce further sub-sections after the tertiary level section (e.g., **1.3.2.1. High-salt diet**).

(2) Special sectioning requirements for an original research article

- **Introduction.** The introduction should provide a background that gives a broad readership an overall outlook of the field and the research performed. It tackles a problem and states its important regarding with the significance of the study. Introduction can conclude with a brief statement of the aim of the work and a comment about whether that aim was achieved.

- **Materials and Methods.** This section provides the general experimental design and methodologies used. The aim is to provide enough detail to for other investigators to fully replicate the results. It is also required to facilitate better understanding of the results obtained. Protocols and procedures for new methods must be included in detail for the reproducibility of the experiments. Informed consent should be obtained from patients or parents before the experiments start and should be mentioned in this section. For human and/or research, research ethics information, such as ethics approval identifiers and the name of Institutional Ethics Review Board or Institutional Review Board, should be indicated in this section.

- **Results.** This section focuses on the results and findings of the experiments performed. After (statistical) analysis, all results, including tables and figures, must be neatly presented. If necessary, this section can be sub-divided into multiple topical sub-sections.

- **Discussion.** This section should provide the significance of the results and identify the impact of the research in a broader context. It should not be redundant or similar to the content of the results section.

- **Conclusion.** Use this section for interpretation only, and not to summarize information already presented in the text or abstract.

It is acceptable to merge both Results and Discussion as a single section.

Unit of measurements

Use SI units.

Data and image processing

Post-acquisition processing of images, photos and figures should be kept minimum to ensure that the final figures accurately reflect the original data as it was captured and/or produced. Any alterations should be applied to the entire image. Any kind of alteration, including but not limited to brightness, contrast and color balance, has to be clearly stated in the figure legend and in Materials and Methods section. For simulated or model figures, the software used for production, editing, and/or processing should be mentioned. Presenting images in the same figure must be made apparent and should be explicitly indicated in the appropriate figure legends.

Data comparisons should only be made from comparative experiments (or data from the same experiment). Same piece of data or figure should not be used in multiple instances, unless the images/data describe different aspects of the same experiment (reasons must be stated, wherever appropriate, in this regard). If inappropriate image/data manipulation is identified after publication, the editors reserve the right to ask for the original data and, if that is not satisfactory, to issue a correction or retract the paper, as appropriate.

Chemical compounds

Materials Science in Additive Manufacturing requires authors to fulfill the requirements below while reporting and/or describing a chemical compound in articles:

Scenario	Requirements
Naming chemical compounds	Use either IUPAC conventions or common names such as cholesterol and cephalosporins
Reporting a new chemical compound	Provide the exact structure of the compound as well as sufficient data regarding the purity and identity of the compound
Reporting the use of a known chemical compound	Provide sufficient data regarding the source, purity and identity of the compound

Figures

Include all figures, including photographs, scanned images, graphs, charts and schematic diagrams, at the back of manuscript. Avoid unnecessary decorative effects (e.g., 3D graphs) and minimize image processing (e.g., changes in brightness and contrast applied uniformly for the entire figure should be avoided or minimized). All images should be set against white background.

All figures should be numbered (e.g., **Figure 1**, **Figure 2**) in boldface. Label all figures (e.g., axis, structures), and add caption (a brief title) and legend as a description of the illustration below each figure. Explain all symbols and abbreviations used. Each figure should have a brief title (also known as caption) that describes the entire figure without citing specific panels, followed by a legend, which is either the description of each panel or further description about the single image. Identify each panel with uppercase letters in parenthesis (e.g. (A), (B), (C), etc.) Figures must be cited in chronological manner in the text.

The preferred file formats for any separately submitted figure(s) are JPEG, PNG and TIFF. All figures should be of optimal resolution. Optimal resolutions preferred are 300 dots per inch (dpi) for RBG colored, 600 dpi for grayscale and 1,200 dpi for line art. Although there is no file-size limitation imposed, authors are highly encouraged to compress their figures to an ideal size without unduly affecting the legibility and resolution of figures.

If necessary, the editors may request author(s) to supply high-resolution and/or unprocessed images after submission or paper acceptance for pre-screening/review and production purposes, respectively.

Tables

Include all tables at the back of manuscript. Editable tables created using Microsoft Word are preferred. A table should be accompanied by a caption on top of it. Captions and legends should be concise. All tables should be numbered (e.g. **Table 1**, **Table 2**) in boldface. Explain all symbols and abbreviations used. Tables must be cited in chronological manner in the text.

Lists and math formulae

Lists and math formulae should be properly aligned and included within the main body of the manuscript. List them using Roman numerals in parenthesis (e.g. (I), (II), (III), (IV), etc.) Lists and math formulae must be cited in chronological manner in the text.

Lists and math formulae should be given in editable text and not as images. Use the solidus (/) for small fractional terms, e.g., X/Y. In principle, variables should be italicized. Powers of e are often more conveniently denoted by exp.

Footnotes

Do not use footnotes.

In-text citations

Reference citations in the text should be numbered consecutively in superscript square brackets. Some examples:

- Negotiation research spans many disciplines[3,4].
- This result was later contradicted by Becker and Seligman[5].
- This effect has been widely studied[1–3,7].

Do not include citations in the Abstract.

Personal communications and unpublished works can only be used in the manuscript and are not to be placed in the References section. Authors are advised to limit such usage to the minimum. These should be made identifiable by stating the authors, year of personal communications or unpublished works, and the words “personal communication” or “unpublished” in parenthesis, e.g., (Smith J, 2000, unpublished).

References

This section is compulsory and should be placed at the end of all manuscripts. Do not use footnotes or endnotes as a substitute for a reference list. The list of references should only include works that are cited in the text and that have been published or accepted for publication. Personal communications and unpublished works should be excluded from this section.

Authors being referenced are listed with their surname or last name followed by their initials. All references should be numbered (e.g. 1, 2, 3, and so on) and sequenced according to the order they appear as the in-text citations. References (especially journal article’s) should follow the general pattern: author(s), followed by year of publication, title of publication, abbreviated journal name in italics, volume number, issue number in parenthesis and lastly, page range or article ID. If the referred article has more than 3 authors, list only the first 3 authors and abbreviate the remaining authors as italicized “*et al*.” (meaning "and others"). Use of DOI is highly encouraged; include DOI, if available, after the page range or article ID. Examples of references for different types of publications are as follows:

(1) Journals

<u>Journal article (print) with 1-3 authors:</u>

Younger P, 2004, Using the internet to conduct a literature search. *Nurs Stand*, 19(6): 45–51.

<u>Journal article (print) with more than 3 authors:</u>

Gamelin FX, Baquet G, Berthoin S, *et al*., 2009, Effect of high intensity intermittent training on heart rate variability in prepubescent children. *Eur J Appl Physiol,* 105(1): 731–738.

<u>Journal article (online) with 1-3 authors:</u>

Jackson D, Firtko A, Edenborough M, 2007, Personal resilience as a strategy for surviving and thriving in the face of workplace adversity: A literature review. *J Adv Nurs*, 60(1): 1–9. http://doi.org/10.1111/j.1365-2648.2007.04412.x

<u>Journal article (online) with more than 3 authors:</u>

Hargreave M, Jensen A, Nielsen TSS, *et al*., 2015, Maternal use of fertility drugs and risk of cancer in children — A nationwide population-based cohort study in Denmark. *Int J Cancer*, 136(8): 1931–1939. http://doi.org/10.1002/ijc.29235

(2) Books

<u>Book with 1-3 authors:</u>

Schneider Z, Whitehead D, Elliott D, 2007, *Nursing and Midwifery Research: Methods and Appraisal for Evidence-based Practice*, 3rd edn, Elsevier Australia, Marrickville, NSW, 112–130.

<u>Book with more than 3 authors</u>

Davis M, Charles L, Curry MJ, *et al*., 2003, *Challenging Spatial Norms*, Routledge, London, 12–30.

<u>Chapter or article in book</u>

Knowles MS, (eds) 1986, Independent study, in *Using Learning Contracts*, Jossey-Bass, San Francisco, 89–96.

(3) Preprints

Preprint article with 1-3 authors:

Ulgen A, Gurkut O, Li W, 2019, Potential Predictive Factors for Breast Cancer Subtypes from a North Cyprus Cohort Analysis. *medRxiv*. https://doi.org/10.1101/19010181

Preprint article with more than 3 authors:

Wu S, Sun P, Li R, *et al*., 2020, Epidemiological Development of Novel Coronavirus Pneumonia in China and Its Forecast. *medRxiv*. https://doi.org/10.1101/2020.02.21.20026229

(4) Others

Proceedings of meetings and symposiums, conference papers:

Chang SS, Liaw L, Ruppenhofer J, (eds) 2000, *Proceedings of the twenty-fifth annual meeting of the Berkeley Linguistics Society, February 12–15, 1999: General session and parasession on loan word phenomena*. Berkeley Linguistics Society, Berkeley, 12–13.

Conference proceedings (from electronic database):

Wang T, Cook C, Derby B, 2009, Fabrication of a glucose biosensor by piezoelectric inkjet printing. *Proceedings of the Third International Conference on Sensor Technologies and Applications, 2009 (SENSORCOM-M'09)*, 82–85.

Online document with author names:

Este J, Warren C, Connor L, *et al*., 2008, Life in the clickstream: The future of journalism, Media Entertainment and Arts Alliance, viewed May 27, 2009, http://www.alliance.org.au/documents/ foj_report_final.pdf

Online document without author name:

Developing an argument, n.d., viewed March 30, 2009, http://web.princeton.edu/sites/writing/Writing_Center/WCWritingResources.htm

Thesis/Dissertation:

Gale L, 2000, The relationship between leadership and employee empowerment for successful total quality management, thesis, *Australasian Digital Thesis database*, University of Western Sydney, 110–130.

Standards:

Standards Australia Online, 2006, Glass in buildings: selection and installation, AS 1288-2006, amended January 31, 2008, *SAI Global database*, viewed May 19, 2009.

Government report:

National Commission of Audit, 1996, *Report to the Commonwealth Government*, Australian Government Publishing Service, Canberra.

Government report (online):

Department of Health and Ageing, 2008, Ageing and aged care in Australia, viewed November 10, 2008, http://www.health.gov.au/internet/main/publishing.nsf/Content/ageing

No author:

Guide to agricultural meteorological practices, 1981, 2nd ed, Secretariat of the World Meteorological Organization, Geneva, 10–20.

Note: When referencing an entry from a dictionary or an encyclopedia with no author there is no requirement to include the source in the reference list. In these cases, only cite the title and year of the source in-text. For an authored dictionary/encyclopedia, treat the source as an authored book.

Acknowledgments*

*This should be included in the title page and back matter file

This is an optional section where authors can acknowledge people and/or institutions that provided non-financial support and/or helped with the research and/or preparation of the manuscript. Examples of non-financial support include externally-supplied equipment/biological sources, writing assistance, administrative support, and contributions from non-authors.

Funding*

*This should be included in the title page and back matter file

Authors should declare all financial support and sources that were used to perform the research, analysis, and/or article publication. Financial supports are generally in the form of grants, royalties, consulting fees and others.

Conflict of interest*

*This should be included in the title page and back matter file

At the time of submission, authors must declare any (potential) conflicts or competing interests with any institutes, organizations or agencies that might influence the integrity of results or objective interpretation of their submitted works. For more information, see our **Conflict of Interest** policy.

Author contributions*

*This should be included in the title page and back matter file

This section should be included in original research articles and review articles. In *Materials Science in Additive Manufacturing*, we encourage authors to use **Contributor Roles Taxonomy (CRediT)** in describing each contributor's specific contribution to the scholarly output in the Author Contributions section.

Definitions of each contributor role as per CRediT are as follows:

Contributor role	Definition
Conceptualization	Ideas; formulation or evolution of overarching research goals and aims.
Data curation	Management activities to annotate (produce metadata), scrub data and maintain research data (including software code, where it is necessary for interpreting the data itself) for initial use and later re-use.
Formal analysis	Application of statistical, mathematical, computational, or other formal techniques to analyze or synthesize study data.
Funding acquisition	Acquisition of the financial support for the project leading to this publication.
Investigation	Conducting a research and investigation process, specifically performing the experiments, or data/evidence collection.
Methodology	Development or design of methodology; creation of models.
Project administration	Management and coordination responsibility for the research activity planning and execution.
Resources	Provision of study materials, reagents, materials, patients, laboratory samples, animals, instrumentation, computing resources, or other analysis tools.
Software	Programming, software development; designing computer programs; implementation of the computer code and supporting algorithms; testing of existing code components.
Supervision	Oversight and leadership responsibility for the research activity planning and execution, including mentorship external to the core team.
Validation	Verification, whether as a part of the activity or separate, of the overall replication/reproducibility of results/experiments and other research outputs.
Visualization	Preparation, creation and/or presentation of the published work, specifically visualization/data presentation.
Writing – original draft	Preparation, creation and/or presentation of the published work, specifically writing the initial draft (including substantive translation).
Writing – review & editing	Preparation, creation and/or presentation of the published work by those from the original research group, specifically critical review, commentary or revision – including pre- or post-publication stages.

Below shows a sample Author Contributions section written based on the CRediT:

Conceptualization: Ali Jackson, Helen Meyer
Investigation: Ali Jackson, Tom Lewis-Hans, Han Xiang
Formal analysis: Han Xiang
Writing – original draft: Ali Jackson
Writing – review & editing: Helen Meyer, Joshua O'Brien

Supplementary files

This section is optional and contains all materials and figures that are excluded from the manuscript. These materials, figures or additional information are relevant to the manuscript but remain non-essential to readers' understanding of the manuscript's main content. All supplementary information should be submitted as a separate file during submission.

Supplementary figures and tables should be submitted in a single, separate supplementary file, and must be numbered, for example, **Figure S1** and **Table S1**. All tables must be editable (preferably created from Microsoft Word). The acceptable formats of images and illustrations used in figures are JPEG, PNG and TIFF. Citations of these items must be appropriately referenced in the manuscript in chronological manner, for instance, “Additional information can be found in **Table S1**.” Note the additional letter **S** helps distinguish the normal from supplementary items.

Data set file are usually prepared using Microsoft Excel (in XLS or XLSX format).

Videos (MP4 format), with a constituent maximum size of 15 MB, can be uploaded as part of the supplementary file.

Revision and response/rebuttal letter

If the editorial decision for a submission is major revision or minor revision, authors are advised to revise the manuscript (and possibly, the supplementary files) as per the review reports and resubmit the revision file, including the manuscript, title page and back matter, cover letter, and response/rebuttal letter, before the due date.

Revisions should be done on the latest version of the manuscript (or in some rare cases, edited manuscript provided by the editor) with the track change on. The revisions made should be described and/or clarified in the response/rebuttal letter; ideally, explanation about the revisions should be made clear with the help of page number and line number. If authors do not agree with reviewers’ comments and suggestions, rebut their points with strong evidence and reasonable arguments.

Materials Science in Additive Manufacturing

Special Issue Alerts

Invitation for Special Issue Proposals

Organizing and editing for a Special Issue helps Guest Editors gain editorial experience and improve academic profile, in addition to being a part of organizing scientific communication of contemporary topics.

If you are published researcher and have an idea for a Special Issue, please write in via email to our Special Issue Commissioning Editor (felicia_wang@whioce.com). Please provide your CV, professional profile page and a topic of interest in your email. Our colleague will guide you in the process of writing a Special Issue proposal.

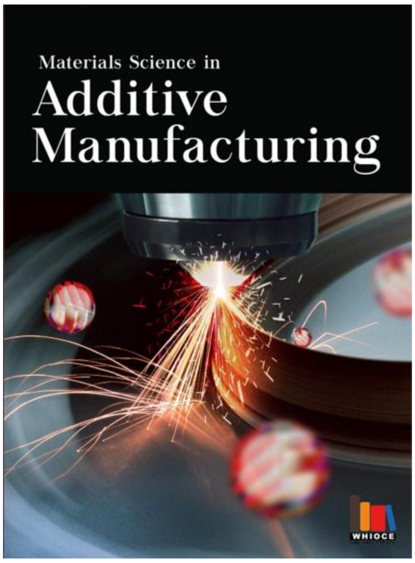

Frequently Asked Questions

1. **Are Special Issue submissions processed in the same way how Regular Issue papers are being pre-screened and reviewed?**
   Yes, all full-length article submissions to a Special Issue will go through the same editorial and peer-review process. The distinct difference here is that the Guest Editors will replace the usual editors and get involved in the making professional decisions on papers after peer review. Note that the specific roles of a Guest Editor could vary across Special Issues.

2. **How many Guest Editors are required to organize a Special Issue?**
   There is no fixed number; however, we suggest no more than 4 Guest Editors per Special Issue. More importantly, all Guest Editors should have excellent publication track records and demonstrated expertise in the topic(s) being proposed.

3. **Is the Special Issue governed by important deadlines?**
   Yes.

Benefits of Being A Guest Editor

- A chance to get involved in the conception and development of a specialty, contemporary topic that is of interest to the readers
- A chance to expand your professional network to the scholars and researchers who are similarly involved in the research of specialty topic
- A chance to hone your editorial skills
- A chance to gain first-hand experience of editing a thematic issue publication, which is a very valuable experience for those who aspire to edit their own journal in future
- A chance to improve your academic profile and help establish your academic influence within your discipline

OUR JOURNALS

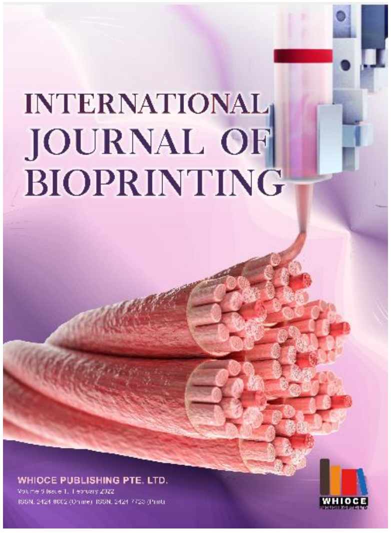

International Journal of Bioprinting is an international journal covering the technology, science and clinical application of the broadly defined field of bioprinting. Bioprinting is defined as the use of 3D printing technology with materials that incorporate viable living cells or biological elements to produce tissue or biotechnological products.

We are interested in the scientific topics spanning all stages of bioprinting process from concept creation to fabrication and beyond. Knowledge generated in these researches must be related to bioprinting.

The journal publishes original research articles on basic and applied research as well as associated social implications of this research. The journal also publishes brief commentaries and reviews. Articles focusing on the practical applications of 3D-printed products are similarly welcome.

The *Journal of Clinical and Translational Research* is an open access, peer-reviewed, multidisciplinary scientific journal that publishes studies with at least an ex vivo, in vivo, or clinical component. The published research is centered on any clearly defined clinical problem, which may comprise a disease or the basis of disease, a form of therapy or intervention, and clinical diagnostics or prognostics. Articles (original research, reviews, technical reports, medical hypotheses, commissioned articles, special issue articles, and editorials) are published continuously online. The key features of this journal are:

- Open access
- No submission or publication fees
- Reputable international editorial board
- Easy and fast submissions - no formatting rules ("your paper, your way")
- No word count or reference restrictions
- Double blind review process to minimize bias
- Rapid online publication of articles upon acceptance
- Outlet for academic institutions and industry

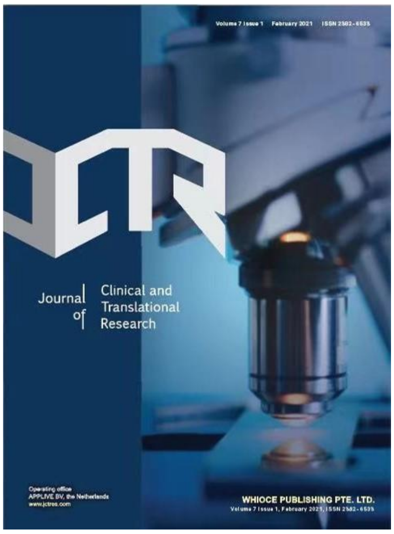

Start a new journal

Write to us via email if you are interested to start a new journal with Whioce Publishing. Please attach your CV, professional profile page and a brief pitch proposal in your email. We shall inform you of our decision whether we are interested to collaborate in starting a new journal.

Contact: info@whioce.com

WHIOCE
PUBLISHING PTE. LTD.

Whioce Publishing Pte. Ltd.
Publishing Office:
73 Upper Paya Lebar Road, #07-02B-06 Centro Bianco, Singapore 534818

Editorial Office:
34-2B, Jalan Puteri 1/2, Bandar Puteri, 47100 Puchong, Selangor, Malaysia.

msam.editor@whioce.com

https://msam.whioce.com/index.php/MSAM/index